

---

# Diffusion MRI for Characterising Childhood Brain Tumours

---

Matthew Grech-Solars BEng (Hons) MSc

A thesis submitted to University College London  
in fulfilment of the requirements for the degree of

Doctor of Philosophy in Medical Physics

Imaging and Biophysics Unit  
UCL Institute of Child Health

~ 2014 ~

## DECLARATION

I, Matthew Grech-Sollars, confirm that the work presented in this thesis is my own. Where information has been derived from other sources, I confirm that this has been indicated in the thesis.

.....

.....

## ABSTRACT

Magnetic resonance imaging (MRI) is widely used both in the clinic and as a research tool in the management of brain tumours. While most studies focus on adult tumours, which have a higher incidence than those in children, paediatric brain tumours differ widely in terms of biology and treatment management. Furthermore, as a non-invasive and non-ionising imaging tool, MRI is used in the diagnosis, prognosis and assessment of treatment response of such tumours. This work focuses on diffusion MRI to study childhood brain tumours.

The thesis is divided into three main parts: a reproducibility study of diffusion MRI parameters in order to answer the question of whether clinical imaging may be used interchangeably across multiple-centres to combine data from different institutions; a study on a tumour border diffusion measure as a prognostic biomarker in children with embryonal brain tumours – the apparent transient coefficient in tumour (ATCT); and a study analysing the functional diffusion map (fDM) as a tool for assessing treatment response in paediatric brain tumours.

Diffusion MRI has been shown to have a good reproducibility and thus data from multiple centres and scanners can be combined in order to analyse clinical data for patients treated at different institutions; particularly where data for specific tumour types would otherwise be limited. In addition, ATCT has been shown to be a useful prognostic biomarker in children with embryonal brain tumours. Finally, while the fDM may be beneficial in assessing treatment response, the underlying biology of both tumour and healthy tissue needs to be carefully considered, and in particular, areas of necrosis, tumour grade and change in tumour size need to be taken into account.

In conclusion, diffusion MRI is a valuable tool in the management of childhood brain tumours, with multi-centre studies paving the way for further research and validation of biomarkers.

Dedicated to Nanna Rita, my Godmother, whose struggle with cancer led me towards wanting to contribute to research in the field; and to all my family and friends who have accompanied their loved ones on a tough journey, and bravely fought on.

“Ask, and you will receive;  
Seek, and you will find;  
Knock, and the door will be opened to you.”

Mt 7:7

## ACKNOWLEDGEMENTS

First, I would like to thank my supervisors Chris Clark, Jonathan Clayden and Dawn Saunders for their continual support and guidance throughout the project. I would also like to thank my colleagues at the Imaging and Biophysics unit, the many lunches, coffees and pub outings we've shared have been an important element, contributing to my PhD perseverance. In addition I would like to thank my colleagues on the multi-centre study, which my PhD formed part of. Work carried out as part of this thesis could not have been done without their help. I would also like to thank Cancer Research UK, who provided the funding for my PhD and thus allowed me to contribute to the field.

I am deeply grateful for the friends I've made during the course of my PhD, and who are now living all around the globe. They accompanied me on an exciting journey in these last years; being present in times of need, helping me grow emotionally and spiritually, while of course having fun and making beautiful memories together. They have been family to me. I am particularly thankful to my friends who have been there for me while I was writing this thesis, who have encouraged me to keep going and offered me a space to de-stress and enjoy life. I am also thankful to those who have read through this thesis and lent a hand in its making.

Heartfelt thanks go to Mum & Dad, Bernard & Tara and all my family. They have been the strongest pillar of support and a constant throughout my life. Their encouraging presence and love has always provided to be a safe haven.

Finally, I would like to remember all the children who were enrolled in this study, and those who have fought, or are still fighting, a tough battle with cancer. May God watch over them and may this work bear his fruit.

## TABLE OF CONTENTS

Declaration .....	2
Abstract .....	3
Dedication .....	4
Acknowledgements.....	6
Table of Contents .....	7
List of Figures .....	12
List of Tables .....	15
Abbreviations .....	16
Glossary .....	18
Chapter 1    Introduction .....	26
1.1    Background.....	26
1.2    Objectives.....	26
1.3    Thesis overview .....	27
Chapter 2    MRI and Diffusion Imaging.....	28
2.1    Physics of MRI.....	28
2.1.1    Background .....	28
2.1.2    A brief history.....	29
2.1.3    Some characteristics of protons .....	29
2.1.4    Behaviour of a group of nuclei.....	31
2.1.5    Forming the signal.....	34
2.1.6    Locating the signal.....	36
2.1.7    Obtaining the image.....	38
2.1.8    Different sequences highlight different things .....	40
2.1.9    Diffusion weighted imaging .....	41
2.1.10    Intra-voxel incoherent motion.....	45

2.1.11	Diffusion tensor imaging .....	46
2.1.12	Image artefacts .....	49
2.2	Data processing .....	50
2.2.1	Data types and data conversion .....	51
2.2.2	Parameter estimation .....	51
2.2.3	Image Processing.....	52
2.2.4	Statistical analysis .....	53
2.3	MRI in the Clinic.....	53
2.3.1	MRI safety .....	53
2.3.2	Limitations of MRI .....	54
2.3.3	Basic clinical brain images.....	55
2.3.4	Diffusion imaging .....	55
Chapter 3	Cancer and Paediatric Brain Tumours.....	56
3.1	Cancer.....	56
3.1.1	Background .....	56
3.1.2	A brief history.....	56
3.1.3	Some characteristics of cells .....	56
3.1.4	Forming a cancer cell .....	59
3.1.5	Hallmarks of cancer.....	60
3.1.6	Histopathology and grading .....	65
3.2	The Brain.....	66
3.2.1	Background .....	66
3.2.2	Cell types .....	67
3.2.3	Anatomy .....	67
3.3	Paediatric Brain Tumours .....	70
3.3.1	Background .....	70
3.3.2	Comparison to adult brain tumours.....	70
3.3.3	Clinical presentation .....	71
3.3.4	Tumour classification .....	71
3.3.5	A note about oedema and necrosis .....	84
3.3.6	Treatment.....	85

---

3.3.7	Late effects.....	88
3.3.8	Imaging.....	89
Chapter 4	Diffusion imaging of brain tumours .....	91
4.1	Reproducibility Studies.....	91
4.1.1	Background .....	91
4.1.2	Phantom studies .....	92
4.1.3	Single-scanner studies.....	94
4.1.4	Multi-centre DWI studies.....	95
4.1.5	Multi-centre DTI studies .....	95
4.1.6	Current needs.....	96
4.2	Diffusion imaging as a diagnostic and prognostic tool.....	96
4.2.1	Background .....	96
4.2.2	Cell density .....	96
4.2.3	Tumour classification and grading .....	98
4.2.4	Prognostic biomarkers .....	101
4.3	Diffusion imaging in treatment management.....	102
4.3.1	Background .....	102
4.3.2	Treatment planning.....	102
4.3.3	Differentiating imaging confounds .....	103
4.3.4	Treatment response.....	104
Chapter 5	Reproducibility of Diffusion Imaging Parameters .....	107
5.1	Background.....	107
5.2	Materials and Methods .....	108
5.2.1	Volunteers.....	108
5.2.2	Scanners .....	108
5.2.3	Phantom.....	108
5.2.4	Imaging Protocol .....	109
5.2.5	Data Analysis .....	112
5.2.6	Statistical Analysis .....	116
5.3	Results .....	116

---

5.3.1	Phantom.....	116
5.3.2	Volunteers.....	118
5.3.3	Field strength comparison .....	128
5.4	Discussion .....	128
5.4.1	Phantom.....	129
5.4.2	Volunteers .....	129
5.4.3	Advantages.....	132
5.4.4	Study limitations .....	133
5.4.5	Conclusion .....	133
Chapter 6	Diffusion Imaging as a Prognostic Biomarker .....	134
6.1	Background.....	134
6.2	Method .....	136
6.2.1	Patients .....	136
6.2.2	Imaging.....	136
6.2.3	Measurements .....	137
6.2.4	Survival analysis .....	138
6.2.5	Reproducibility study .....	140
6.3	Results .....	141
6.3.1	Correlating ADC measures with survival.....	141
6.3.2	Kaplan-Meier curves .....	142
6.3.3	Multivariate survival analysis.....	143
6.3.4	ATCT Kaplan-Meier curves .....	144
6.3.5	Reproducibility study .....	145
6.4	Discussion .....	146
6.4.1	ATCT .....	146
6.4.2	ATCO, mean and minimum ADC .....	147
6.4.3	Tumour type.....	147
6.4.4	Metastasis at presentation .....	148
6.4.5	ATCT across embryonal brain tumours.....	148
6.4.6	Statistical analysis .....	149
6.4.7	Study limitations .....	149

---

6.5 Conclusion .....	151
Chapter 7 Diffusion Imaging for Treatment Response .....	152
7.1 Background.....	152
7.2 Method .....	154
7.2.1 Image acquisition .....	154
7.2.2 fDM analysis .....	155
7.2.3 Areas of necrosis .....	156
7.2.4 Tumour grade.....	158
7.2.5 Change in tumour size.....	159
7.2.6 Statistical analysis .....	159
7.3 Results .....	159
7.3.1 Areas of necrosis .....	160
7.3.2 Tumour Grade.....	162
7.3.3 Change in Tumour Size.....	164
7.3.4 Histology.....	165
7.4 Discussion .....	165
7.4.1 Areas of necrosis .....	166
7.4.2 Tumour grade.....	166
7.4.3 Change in tumour size.....	167
7.4.4 Study limitations .....	167
7.5 Conclusion .....	168
Chapter 8 Discussion.....	169
8.1 Advances made .....	169
8.2 Future studies.....	170
8.3 Conclusion .....	171
Appendix A: List of publications and conference presentations .....	172
References .....	176

## LIST OF FIGURES

Figure 2.1: The electromagnetic spectrum.....	28
Figure 2.2: Spin alignment in a magnetic field.....	29
Figure 2.3: Precession .....	30
Figure 2.4: Net magnetisation.....	31
Figure 2.5: Net magnetisation recovery .....	33
Figure 2.6: Spin echo phase diagram .....	34
Figure 2.7: Spin echo signal acquisition .....	35
Figure 2.8 Applying a gradient .....	36
Figure 2.9: Slice selection.....	37
Figure 2.10: Phase encoding .....	38
Figure 2.11: Obtaining the image.....	39
Figure 2.12: T1- and T2-weighted images.....	40
Figure 2.13: Diffusion-weighted imaging .....	42
Figure 2.14: Diffusion-weighted images .....	44
Figure 2.15: IVIM graph.....	45
Figure 2.16: Defining an ellipsoid.....	47
Figure 2.17: DTI parameters .....	49
Figure 2.18: Data processing.....	50
Figure 3.1: Structure of a cell .....	57
Figure 3.2: The cell cycle .....	58
Figure 3.3: Hallmarks of cancer.....	60
Figure 3.4: Anatomy of the brain .....	67
Figure 3.5: The ventricular system.....	69
Figure 3.6: Juvenile pilocytic astrocytoma in a 9 year old female patient .....	73
Figure 3.7: Optic pathway glioma in a 1 year old female patient.....	74
Figure 3.8: Subependymal giant cell astrocytoma in an 11 year old male patient .....	75
Figure 3.9: Glioblastoma multiforme in a 7 year old male patient.....	76
Figure 3.10: Gliomatosis cerebri in a 17 year old male patient.....	77

---

Figure 3.11: Diffuse intrinsic pontine glioma in a 9 year old male patient.....	78
Figure 3.12: Ependymoma in a 2 year old female patient.....	79
Figure 3.13: Choroid plexus papilloma (grade 1) in a one month old male patient.....	80
Figure 3.14: Medulloblastoma in a 7 year old female patient.....	81
Figure 3.15: Atypical teratoid/rhabdoid tumour in a 2 year old male patient .....	82
Figure 3.16: Supratentorial primitive neuroectodermal tumour in a 9 year old male patient.....	83
Figure 3.17: Pineoblastoma in a 10 year old male patient .....	84
Figure 4.1: Ice-water phantom .....	92
Figure 4.2: ADC and tumour cellularity.....	97
Figure 4.3: Comparison between ADC and histology .....	97
Figure 4.4: Mean ADC by tumour type in a paediatric cohort.....	99
Figure 4.5: Tumour border biomarkers.....	101
Figure 4.6: The functional diffusion map .....	105
Figure 4.7: Biology of the fDM .....	106
Figure 5.1: Segmentation of T1-weighted images .....	113
Figure 5.2: Measuring FA in white matter areas.....	115
Figure 5.3: Comparison of the ice-water phantom ADC images across scanners .....	118
Figure 5.4: Box plots for DWI and DTI parameters across all scanners in grey matter .....	120
Figure 5.5: Box plots for DWI and DTI parameters across all scanners in white matter .....	121
Figure 6.1: Measuring the ATCT .....	137
Figure 6.2: Plot of survival against ATCT, ATCO, mean ADC and minimum ADC in 58 patients .....	142
Figure 6.3: Kaplan-Meier survival curves for age at diagnosis, extent of surgery, tumour type, and metastasis at presentation .....	143
Figure 6.4: Kaplan-Meier survival curves for increasingly negative values of ATCT.....	144
Figure 6.5: Visualising the ATCT .....	147
Figure 7.1: Construction of the fDM .....	155
Figure 7.2: Theoretical change in areas of necrosis by treatment .....	157

---

Figure 7.3: Theoretical changes in the fDM in tumours of varying grade .....	158
Figure 7.4: The fDM in areas of necrosis.....	160
Figure 7.5: The fDM in tumours of varying grade.....	162
Figure 7.6: Change in tumour size .....	164
Figure 7.7: Histological comparison of low and high-grade tumours.....	165

## LIST OF TABLES

Table 3.1: Central nervous system tumour classification (ICD-O 9380–9539) .....	72
Table 5.1: DWI protocol. ....	110
Table 5.2: DTI protocol.....	111
Table 5.3: Reproducibility of the ice-water phantom.....	117
Table 5.4: Reproducibility in volunteers for ADC.....	122
Table 5.5: Reproducibility in volunteers for D .....	123
Table 5.6: Reproducibility in volunteers for f .....	124
Table 5.7: Reproducibility in volunteers for MD.....	125
Table 5.8: Reproducibility in volunteers for FA .....	126
Table 5.9: Reproducibility of FA .....	127
Table 5.10: Comparison of CV in 1.5, 3T and all scanners .....	128
Table 6.1: Survival details for increasingly negative values of ATCT .....	145
Table 7.1: The fDM in necrotic areas compared to clinical response and change in size in necrotic areas.....	161
Table 7.2: fDM changes by tumour grade and clinical response .....	163

## ABBREVIATIONS

Abbreviation	Definition
<b>ADC</b>	Apparent Diffusion Coefficient (parameter in DWI)
<b>ATC</b>	Apparent Transient Coefficient
<b>ATCO</b>	Apparent Transient Coefficient from white matter to Oedema
<b>ATCT</b>	Apparent Transient Coefficient from oedema to the Tumour core
<b>ATRT</b>	Atypical Teratoid/Rhabdoid Tumour
<b>CNS</b>	Central Nervous System
<b>COV</b>	Coefficient Of Variance
<b>CR</b>	Coefficient of Repeatability
<b>CSF</b>	Cerebro-Spinal Fluid
<b>CT</b>	Computed Tomography
<b>CV</b>	Coefficient of Variation
<b>D</b>	slow Diffusion coefficient (parameter in IVIM)
<b>DICOM</b>	Digital Imaging and COmmunications in Medicine
<b>DIPG</b>	Diffuse Intrinsic Pontine Glioma
<b>DNA</b>	DeoxyriboNucleic Acid
<b>DTI</b>	Diffusion Tensor Imaging
<b>DWI</b>	Diffusion-Weighted Imaging
<b>EPI</b>	Echo Planar Imaging
<b>f</b>	perfusion fraction (parameter in IVIM)
<b>FA</b>	Fractional Anisotropy (parameter in DTI)
<b>fDM</b>	functional Diffusion Map
<b>FID</b>	Free Induction Decay
<b>FLAIR</b>	FLuid Attenuated Inversion Recovery
<b>FOV</b>	Field Of View
<b>GBM</b>	Glioblastoma Multiforme
<b>GC</b>	Gliomatosis Cerebri

Abbreviation	Definition
<b>GM</b>	Grey Matter
<b>IVIM</b>	Intra-Voxel Incoherent Motion
<b>JPA</b>	Juvenile Pilocytic Astrocytoma
<b>MD</b>	Mean Diffusivity (parameter in DTI)
<b>MR</b>	Magnetic Resonance
<b>MRI</b>	Magnetic Resonance Imaging
<b>NF1</b>	Neurofibromatosis Type 1
<b>OPG</b>	Optic Pathway Glioma
<b>PACS</b>	Picture Archiving and Communication System
<b>PET</b>	Positron Emission Tomography
<b>PGSE</b>	Pulsed Gradient Spin-Echo
<b>PNET</b>	Primitive NeuroEctodermal Tumour
<b>RF</b>	Radio Frequency
<b>ROC</b>	Receiver Operating Characteristic
<b>ROI</b>	Region Of Interest
<b>ROIs</b>	Regions Of Interest
<b>SEGA</b>	SubEpendymal Giant cell Astrocytoma
<b>SNR</b>	Signal-to-Noise Ratio
<b>sPNET</b>	supratentorial Primitive NeuroEctodermal Tumour
<b>TE</b>	Time to Echo
<b>TR</b>	Time to Repeat
<b>VEGF</b>	Vascular Endothelial Growth Factor
<b>WHO</b>	World Health Organisation
<b>WM</b>	White Matter

## GLOSSARY

Term	Definition
<b>MRI Section</b>	
<b>acquisition matrix</b>	The number of independent data samples taken in the phase-encode and frequency-encode directions, determining the resolution of the image.
<b>anisotropy</b>	A physical property of having different values for measurements in different directions; high diffusion anisotropy implies diffusion occurs more in one of the directions.
<b>artefacts</b>	False features in an image, produced during image acquisition.
<b>bandwidth</b>	A range of frequencies.
<b>contrast-agent</b>	A substance administered to the patient in order to enhance the image intensity of a particular region, generally by altering relaxation times.
<b>coronal plane</b>	The plane which divides the body into a dorsal and ventral part.
<b>dephasing</b>	The loss of phase coherence between signals in the transverse plane.
<b>echo time (TE)</b>	The time (in ms) between applying the 90° RF pulse and the peak of the echo signal produced using a spin echo sequence.
<b>eddy current</b>	An electric current induced in a conductor by a time-varying magnetic field, which may cause artefacts in images.
<b>energy state</b>	One of a number of distinct energy levels for each spin in a magnetic field, determined by the spin quantum number.
<b>field of view (FOV)</b>	A rectangular region over which MRI data is acquired.

Term	Definition
<b>Fourier transform</b>	A mathematical transform which converts a time signal into the frequency domain and vice versa. It is used in MRI to reconstruct spatial information from the raw data acquired.
<b>free induction decay</b>	The decay of the transverse magnetisation MR signal towards zero with a time constant $T_2^*$ .
<b>frequency encoding</b>	The encoding of MR signals along a direction by applying a magnetic field gradient along that direction during data acquisition, such that spatial information is encoded in a frequency gradient.
<b>ghosting artefact</b>	An image artefact associated with motion resulting in phase errors.
<b>gradient echo</b>	A signal echo produced by reversing the magnetic field gradient's direction.
<b>gyromagnetic ratio</b>	A constant for a given nucleus which represents the ratio of magnetic moment to angular momentum.
<b>ionising radiation</b>	Radiation which has enough energy to interact with an atom and remove one of its bound electrons, thus ionising the atom.
<b>k-space</b>	The space in which the Fourier transform of the image is represented, and in which MR data is acquired.
<b>Larmor frequency</b>	The frequency at which magnetic resonance in a nucleus can be excited.
<b>lattice</b>	The magnetic and thermal environment with which nuclei exchange energy in longitudinal ( $T_1$ ) relaxation.
<b>longitudinal magnetisation (<math>M_z</math>)</b>	The component of magnetisation which is along the static magnetic field.
<b>magnetic field gradient</b>	A magnetic field gradient which changes in strength along a given direction.
<b>magnetic field inhomogeneity</b>	Deviation of the local magnetic field from the average value.

Term	Definition
<b>magnetic resonance</b>	The absorption and/or emission of electromagnetic energy by a nucleus in a static magnetic field after an RF pulse is applied.
<b>matrix size</b>	The number of data points in each of the directions, which may be different from the acquisition matrix.
<b>noise</b>	The component of a reconstructed image relating to unwanted interference in the image.
<b>non-invasive</b>	A procedure that allows for the diagnosis or treatment of a disease without the need to enter into the body.
<b>NSA</b>	The number of signals averaged together to construct the image.
<b>nuclear spin</b>	An intrinsic property of a nucleus which gives an associated magnetic moment and angular momentum.
<b>parallel imaging</b>	A means of increasing acquisition speed by using multiple receiver coils to collect data from different areas simultaneously.
<b>partial volume effect</b>	The loss in contrast when one voxel covers more than one tissue type.
<b>phantom</b>	An object with known properties used for testing MRI systems.
<b>phase encoding</b>	The encoding of MR signals along a direction by applying a magnetic field gradient along that direction prior to data acquisition, such that spatial information is encoded in a phase difference.
<b>precession</b>	The motion of the axis of a spinning body such that the axis of rotation traces out the shape of a cone.
<b>radiofrequency</b>	An electromagnetic wave at a frequency in the same range as that used for radio transmission, in the MHz range.
<b>repetition time (TR)</b>	The time between the beginning of a pulse sequence and the subsequent pulse sequence.

Term	Definition
<b>sagittal plane</b>	The plane which divides the body into left and right parts.
<b>slice selection</b>	A method for exciting a specific slice of tissue by applying a gradient magnetic field and a narrow-band RF pulse concurrently.
<b>SNR</b>	The signal-to-noise ratio describing the proportion of signal to random noise present in the image.
<b>spin echo</b>	A signal echo produced by first applying a 90° excitation RF pulse, followed by a 180° refocusing RF pulse.
<b>spin-lattice (longitudinal) relaxation time (<math>T_1</math>)</b>	The time it takes spins to align themselves with the external magnetic field from a magnetisation in the z-direction of 0 to 63% of its maximum value.
<b>spin-spin (transverse) relaxation time (<math>T_2</math>)</b>	The time it takes for spins to lose phase coherence, and thus for the MR signal to lose 63% of its initial value.
<b><math>T_1</math>-weighted</b>	An image where the majority of contrast stems from tissue differences in $T_1$ values (fluid is dark, white matter is bright).
<b><math>T_2</math>-weighted</b>	An image where the majority of contrast stems from tissue differences in $T_2$ values (fluid is bright, white matter is dark).
<b>transverse magnetisation (<math>M_{xy}</math>)</b>	The component of magnetisation which is at right angles to the static magnetic field, and is responsible for the signal detected by MR.
<b>transverse plane</b>	The plane which divides the body into the superior and inferior parts.

### Cancer Section

<b>adjuvant</b>	In addition to the main treatment.
<b>anaplastic</b>	Lacking differentiation characteristics of the tissue of origin.
<b>angiogenesis</b>	The formation of new blood vessels.

Term	Definition
<b>apoptosis</b>	Programmed cell-death.
<b>ataxia</b>	Loss of coordination of muscle movement.
<b>autophagy</b>	A cellular response to a lack of nutrients, causing the breakdown of organelles within the cell to provide energy.
<b>benign</b>	A growth which is confined to a specific area within a tissue with no evidence of invasion.
<b>calcification</b>	The deposit of calcium in a location.
<b>cancer</b>	A malignant condition in which abnormal cells grow and spread within the body.
<b>carcinogenic</b>	Able to contribute to or cause the formation of cancer.
<b>cell cycle</b>	The sequence of events a cell goes through from when it is created to when its DNA is doubled and the cell divides.
<b>centromere</b>	The region of the chromosome than holds the two chromatids together.
<b>chromosome</b>	A thread like structure found in nuclei and holding the genetic information in DNA.
<b>contralateral</b>	The opposite side.
<b>cystic</b>	Characterised by cysts, an abnormal sac containing liquid.
<b>cytosol</b>	The liquid component of the cytoplasm which contains all organelles.
<b>embolization</b>	The process of forming an embolus, a blood clot that can travel through the circulatory system and lodge somewhere in the body.
<b>eukaryotic</b>	Cells having a membrane-bound nucleus.
<b>extravasation</b>	The process of forcing (an embolus) out of the vascular system and into the surrounding tissue.

Term	Definition
<b>gene</b>	The basic unit of heredity.
<b>genomic stability gene</b>	Genes which keep mutations to a minimum.
<b>genotype</b>	The genetic constitution of a person.
<b>growth factor</b>	A protein that is able to stimulate growth or cell proliferation.
<b>high-grade</b>	A tumour which has progressed and become malignant.
<b>histopathology</b>	The study of changes in tissue caused by disease.
<b>hypoxia</b>	The state of low oxygen levels reaching the tissue.
<b>immortality</b>	A trait of a cell to proliferate indefinitely.
<b>incidence</b>	The frequency of occurrence of a given disease.
<b>intravasation</b>	The process of forcing (a cancer cell) into the vascular system.
<b>invasion</b>	The process by which cancer cells move from a primary area to invade a secondary region.
<b>ipsilateral</b>	The same side.
<b>low-grade</b>	A tumour which has not progressed extensively and is relatively benign.
<b>lymphatic vessel</b>	A vessel which carries lymph, which is formed from the interstitial fluid between cells.
<b>malignant</b>	A growth which spreads into surrounding tissue or other parts of the body.
<b>metastasis</b>	A malignant growth which has spread to another region of the body.
<b>mitosis</b>	The process by which a single cell separates the chromosomes into two equal sets in preparation for cell division.

Term	Definition
<b>morphology</b>	The shape and form of a cell.
<b>mortality</b>	The rate of cell death due to a specific disease or condition.
<b>motility</b>	The ability of individual cells to move from one location to another.
<b>mutation</b>	A change in the genotype, resulting in the creation of a new trait.
<b>necrosis</b>	The process of cell death which is not programmed.
<b>neoadjuvant</b>	Applied prior to the main treatment.
<b>oedema</b>	An abnormal retention of fluid.
<b>oncogene</b>	A cancer inducing cell.
<b>primary tumour</b>	The first mass of cancer cells at the place of origin, where the cancer began.
<b>prognosis</b>	A forecast of the likely course of a disease.
<b>progression</b>	The phase in tumour growth characterised by the ability of tumour cells to grow rapidly and invade other areas.
<b>resection</b>	Removal by surgery.
<b>secondary tumour</b>	Also metastases, a tumour which has spread to secondary regions different from the origin.
<b>stroma</b>	The space within a cell or tissue which supports the cell or tissue.
<b>telomere</b>	The structure at the end of the chromosomes, which protects the ends from degradation and from fusion with other chromosomes.
<b>transcription factor</b>	A protein involved in the transcription (copying of DNA sequences) of a gene.
<b>tumour</b>	A growth in one specific area.

Term	Definition
<b>tumour suppressor gene</b>	A gene, which if inactivated leads to an increased chance of developing cancer.

# Chapter 1 INTRODUCTION

## 1.1 Background

Cancer makes frequent appearance in the news. Its high prevalence means that it is a disease which touches the lives of a large proportion of the population, affecting not only patients, but also their families and friends. It is, however, rare in children and as a result fewer research studies have been carried out in this patient group. Brain tumours are the second most common tumour in children, after leukaemia, and are generally diagnosed using magnetic resonance imaging (MRI). This standard clinical imaging normally includes diffusion-weighted imaging, a technique which uses the diffusion of water molecules to determine the nature of the underlying microstructure. The main focus of this PhD thesis is to investigate the use of diffusion MRI in childhood brain tumours and to present work carried out in order to advance knowledge in the field. This was done with the view of improving patient treatment management through identifying prognostic imaging biomarkers, studying imaging tools used in treatment response and exploring the image variation expected in multi-centre studies.

## 1.2 Objectives

Research carried out in imaging of paediatric brain tumours is limited and sparse, which may be a reflection of the rarity of these tumours. As part of a multi-centre study, the objectives of this thesis include an analysis to determine whether data from multiple centres can be combined so as to conduct studies on a larger cohort of similar tumours, which would allow for more meaningful analyses of individual tumour types. Second, the thesis aims to study diffusion imaging as a prognostic tool in order to determine whether it can be used as a biomarker of survival so as to aid in the treatment planning and management of brain tumours. The third objective is to analyse diffusion imaging as a tool for identifying early treatment response by applying tools currently used in brain tumours in adults to those in children.

### 1.3 Thesis overview

In Chapter 2 the basics of MRI and diffusion imaging are presented by describing the physics behind MRI and diffusion imaging. The chapter then describes the necessary data processing steps, from acquiring data on the scanner to performing the required statistical analyses, and concludes with the current uses of MRI in the clinic.

Chapter 3 starts with a description of the basics of cancer by presenting cell biology and how a cancer cell may form, together with the hallmarks of cancer. It is followed by a description of brain anatomy, prior to presenting paediatric brain tumours in more detail.

Chapter 4 presents the importance of reproducibility studies and current research carried out. It then focuses on the use of diffusion MRI in childhood cancer, particularly as a tool for diagnosis, prognosis and treatment response.

The subsequent three chapters present the research component of this thesis. Chapter 5 describes results for the reproducibility of diffusion MRI parameters from a multi-centre study. Chapter 6 focuses on a prognostic imaging biomarker analysed in a specific paediatric brain tumour type. Chapter 7 then moves on to explore a diffusion MRI tool suggested for determining treatment response.

Finally, a discussion is held on the advances provided by this work and in the field, and how this may be taken forward.

## Chapter 2 MRI AND DIFFUSION IMAGING

The main aim of this chapter is to provide a background of MRI physics, and in particular diffusion imaging. This is followed by an outline of how data is processed after images are acquired from the scanner and an overview of MRI safety, limitations and its uses in the clinic.

### 2.1 Physics of MRI

#### 2.1.1 BACKGROUND

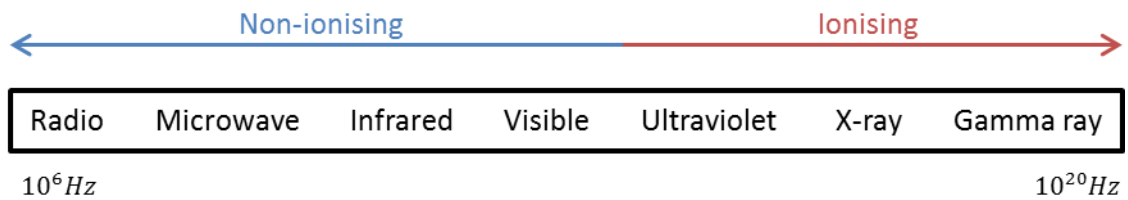


**Figure 2.1: The electromagnetic spectrum.** Higher frequencies cause ionisation which raises safety issues. From the non-ionising set, visible light does not penetrate the skin, infrared is only able to enter the body superficially and microwaves cause heating and are thus not safe. MRI, which lies in the radio frequency range, is able to penetrate the body without causing harm.

MRI is considered a safe and non-invasive imaging technique. The reason behind this can be explained in terms of the electromagnetic spectrum shown in Figure 2.1. To identify a suitable imaging technique, two elements need to be taken into consideration – transparency and safety. Visible light is not useful for body and brain imaging as it does not penetrate the skin. The higher frequencies on the electromagnetic spectrum tend to pose a safety issue: while X-ray, computed tomography (CT) and positron emission tomography (PET) are used in diagnostic medical imaging, they carry an element of risk in terms of radiation dose. The ionising radiation associated with these techniques may lead to DNA damage, caused by the free radicals formed as electrons are ejected from their molecules. In the lower wavelengths, infrared can be used, but it is only able to penetrate the skin superficially

and hence its applications are limited. That said, near infrared can be beneficial in the clinic, particularly in a neonatal setting to monitor tissue oxygenation<sup>1</sup>. Microwaves pose a safety issue due to thermal heating and hence the best frequency range for a safe and non-invasive imaging modality is that of radio waves, in which MRI frequencies lie. MRI therefore has the benefit of an imaging modality that is able to probe the whole body without causing harm. This section gives an account of the physics behind MRI and in particular diffusion imaging.

### 2.1.2 A BRIEF HISTORY

Magnetic resonance (MR) was first described by Rabi et al in 1938<sup>2</sup> as a method for determining nuclear magnetic moments. It was further explored following the Second World War by Purcell et al in 1945<sup>3</sup> and by Bloch in 1946<sup>4</sup>. It can be explained by taking a quantum mechanics approach or a classical physics approach and a combination of both is taken in this chapter. In order to understand the basis for today's MRI, we need to start with the behaviour of the most abundant chemical substance, hydrogen, the nucleus of which contains just one proton.

### 2.1.3 SOME CHARACTERISTICS OF PROTONS

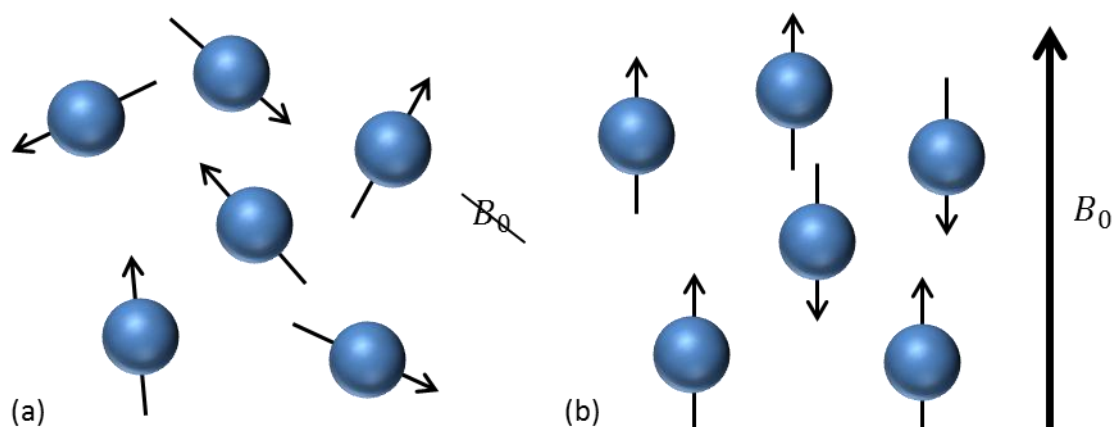


**Figure 2.2: Spin alignment in a magnetic field.** Hydrogen nuclei, consisting of one proton, will possess a spin and in the absence of an external magnetic field (a) will orient themselves in a random direction. In the presence of a strong magnetic field (b), a very small majority of nuclei will orient themselves in the direction of the external magnetic field, while the other nuclei will orient themselves in the higher energy state which is against the external magnetic field,  $B_0$ .

Every nucleus with an odd atomic and/or mass number has what is known as spin and the associated property of angular momentum. Hydrogen, with an atomic number of 1 consists of one proton and has a spin of  $\frac{1}{2}$ . Due to the positive charge and this spin, each nucleus will also possess magnetic properties. In the absence of a strong external magnetic field, at thermal equilibrium, the spin of each hydrogen nucleus will have no preferred direction, and the overall magnetism of all the hydrogen atoms will be zero (Figure 2.2a). In the presence of a strong external magnetic field, a small majority of protons will orient themselves parallel to the direction of the magnetic field, and the remainder will take an anti-parallel direction (Figure 2.2b). The number of atoms which align with or against the direction of the magnetic field is given by Boltzmann's equation in (2.1).

$$\frac{N_\uparrow}{N_\downarrow} = 1 + \frac{\gamma\hbar B_0}{k_B T} \quad (2.1)$$

where  $N_\uparrow$  and  $N_\downarrow$  are the number of nuclei having a spin along and against the direction of the magnetic field  $B_0$  respectively,  $\gamma$  is the gyromagnetic ratio of protons,  $\hbar$  is the rationalised Planck's constant,  $k_B$  is Boltzmann's constant and  $T$  is the temperature of the material in Kelvin.

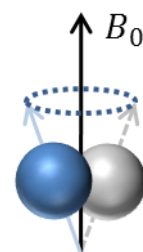


**Figure 2.3: Precession.** A nucleus aligned with, or against, the external magnetic field will precess around the direction of the magnetic field at what is known as the Larmor frequency.

The energy state of the nucleus depends on whether a nucleus will align parallel or against the direction of the magnetic field. A parallel direction requires less energy and at room temperature, there will be more nuclei aligned in this direction. Furthermore, the interaction of the nuclei with the magnetic field causes the nuclear magnets to

precess around the external magnetic field as shown in Figure 2.3. The precession frequency is given by the Larmor equation in (2.2).

$$\omega_0 = \gamma B_0 \quad (2.2)$$

where  $\omega_0$  is the angular frequency of protons,  $\gamma$  is the gyromagnetic ratio of protons and  $B_0$  is the magnetic field.

In order for a nucleus to move from the lower parallel energy state to the higher anti-parallel energy state, it must acquire energy through a radio-frequency (RF) pulse. The frequency at which this can happen is the Larmor frequency. When an RF pulse, at the Larmor frequency is applied, some of the nuclei will gain energy to move from the parallel direction to the anti-parallel direction. The nuclei can subsequently lose this energy by re-orienting in the parallel direction, a process known as relaxation.

#### 2.1.4 BEHAVIOUR OF A GROUP OF NUCLEI

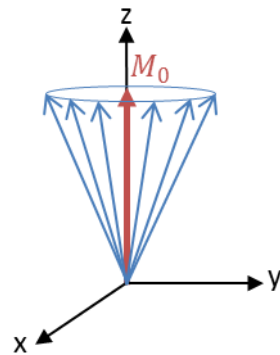


**Figure 2.4: Net magnetisation.** As there is a slight majority of nuclei aligned with the external magnetic field, there will be a small net magnetisation  $M_0$  in the same direction as the external magnetic field.

In MRI, we generally image a volume of tissue, or a voxel, and in each voxel a large number of hydrogen nuclei are present. By analysing voxels, we study the combined effect of the hydrogen nuclei in a specific area of tissue. Given there are more nuclei aligned parallel with the magnetic field, and the direction of precession is random at any given time point, the sum of all the spins will result in a net magnetisation,  $M_0$ , in the direction of the magnetic field as shown in Figure 2.4. As the number of spins aligning parallel to  $B_0$  is only marginally more than those aligning in the anti-parallel

direction,  $M_0$  is very small and in the order of microtesla<sup>5</sup>. Hence, it is difficult to measure at equilibrium while aligned with the main field  $B_0$ .

When an RF pulse at the Larmor frequency is applied, some of the nuclei in the parallel direction will absorb the energy necessary to re-orient themselves into the higher energy state. It transpires that the net magnetisation will be flipped at an angle which is dependent on the strength and duration of the RF pulse as given by equation (2.3).

$$\alpha = \gamma B_1 t_p \quad (2.3)$$

where  $\alpha$  is the flip angle,  $\gamma$  is the gyromagnetic ratio,  $B_1$  is the magnetic field of the RF pulse and  $t_p$  is the duration of the RF pulse.

Applying a 90° RF pulse, with  $B_1$  in the x-direction, forces the net magnetisation to flip into the transverse plane such that the longitudinal magnetisation ( $M_z$ ) is zero and the net magnetisation is equal to the transverse magnetisation ( $M_{xy}$ ). This transverse magnetisation rotates at the Larmor frequency and can be measured through the voltage that it induces in a receiver coil. By Faraday's law, the voltage generated is proportional to the transverse magnetisation, which can thus be measured.

After flipping the net magnetisation into the transverse plane, the nuclear spins will fan out and become out of phase with each other. As the protons quickly dephase, the transverse magnetisation rapidly decreases towards zero. The resulting rapidly decreasing signal is known as free induction decay (FID). This dephasing of spins is an effect of both field inhomogeneity, inherent in every scanner, and interaction with the magnetism of neighbouring nuclei. Field inhomogeneity is a fixed effect, while the interactions with the neighbouring nuclei are a random effect. Overall, the rate at which the dephasing occurs, and hence at which the transverse magnetisation decays to its original value of zero, is given by Bloch equation (2.4) and is shown in Figure 2.5a.

$$M_{xy} = M_{0xy} e^{-\frac{t}{T_2^*}} \quad (2.4)$$

where  $M_{xy}$  is the transverse magnetisation,  $M_{0xy}$  is the net magnetisation in the transverse plane and is equivalent to the longitudinal magnetisation  $M_z$  before the

application of the RF pulse,  $t$  is the time allowed for recovery, and  $T_2^*$  is the  $T_2^*$  relaxation time.

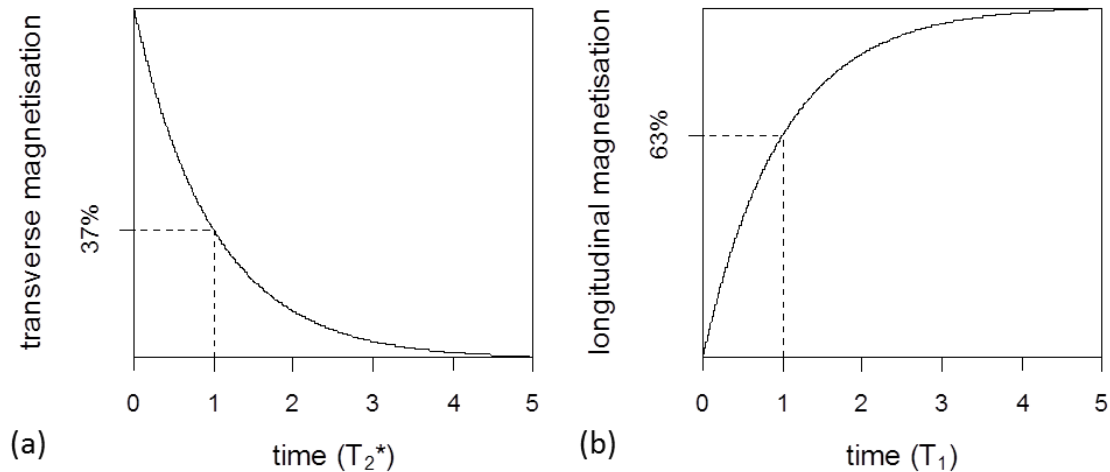


**Figure 2.5: Net magnetisation recovery.** After the magnetisation is tipped into the transverse plane by application of the RF pulse, (a) the transverse magnetisation will decrease at a rate defined by  $T_2^*$  and (b) the longitudinal magnetisation will recover at a rate defined by  $T_1$ .

While the decrease in  $M_{xy}$  is rapid, the recovery of the longitudinal magnetisation is slower. When the RF pulse is switched off, the spins will start reverting back to the original direction, and as a result the longitudinal magnetisation will recover as given by Bloch equation (2.5) and shown in Figure 2.5b.

$$M_z = M_0(1 - e^{-\frac{t}{T_1}}) \quad (2.5)$$

where  $M_z$  is the longitudinal magnetisation,  $M_0$  is the net magnetisation in the longitudinal plane,  $t$  is the time allowed for recovery, and  $T_1$  is the longitudinal relaxation time or spin-lattice relaxation time.

After  $1T_1$  the signal recovers to 63% of the original value, and after  $5T_1$  the signal is in practice almost fully recovered. A longer value of  $T_1$  therefore implies a longer longitudinal recovery time. The longitudinal relaxation time is material-dependent. This is because longitudinal relaxation depends on local fluctuating magnetic fields, and in particular on fluctuations close to the Larmor frequency. Such fluctuations arise as a result of molecular motion, and so the degree of molecular mobility is an

important factor in determining  $T_1$  values. Hence, more liquid-like materials tend to have long  $T_1$  values – for example, cerebro-spinal fluid (CSF) has longer  $T_1$  values than grey and white matter. Additionally, the Larmor frequency is dependent on the value of  $B_0$ . Hence,  $T_1$  will also be affected by a change in  $B_0$ .

### 2.1.5 FORMING THE SIGNAL

As described, the signal we measure in MR, is the transverse magnetisation, and thus is dependent on the transverse magnetisation recovery time. The rapid decrease in magnetisation makes it difficult to acquire the MR signal, and the FID cannot be used. In practice, echoes – the gradient echo and the spin echo – are created, and the spin echo is here described.

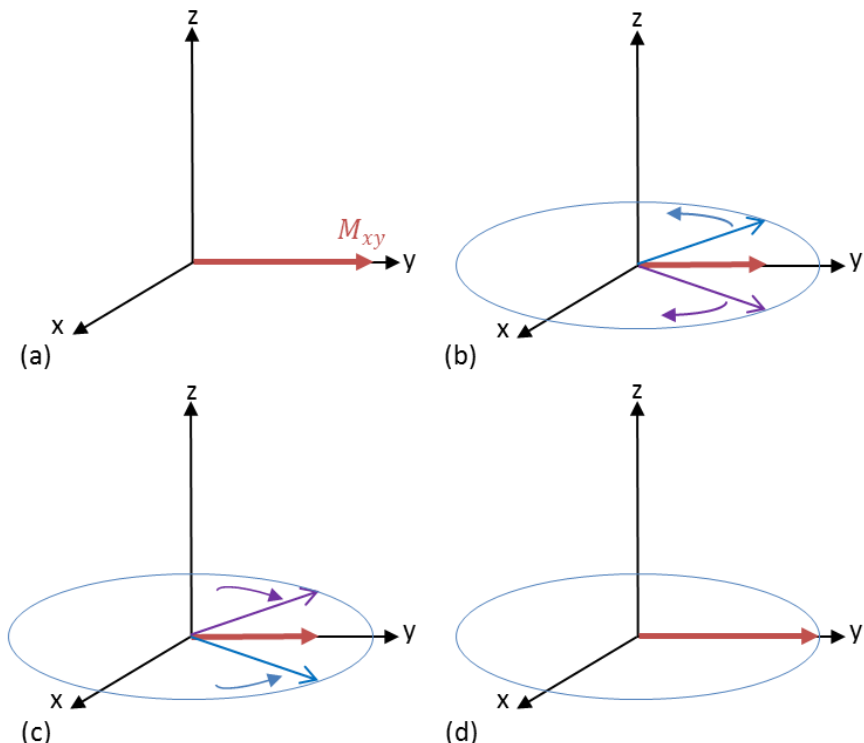


**Figure 2.6: Spin echo phase diagram.** (a) Spins are tipped into the transverse plane after application of a 90° RF pulse. (b) Due to field inhomogeneity, spins will dephase at a different rate and the net magnetisation in the transverse plane will reduce rapidly at a rate defined by  $T_2^*$ . (c) After a 180° RF pulse is applied in the y-direction, the spins will flip along the axis and continue dephasing in the same direction and at the same rate as they previously were. (d) After a time  $TE$ , the spins will realign and the signal in the transverse plane reappears.

The main cause for the rapid dephasing in the transverse plane is the different magnetic fields each nucleus experiences. As this field inhomogeneity is a fixed effect, when we apply a  $180^\circ$  RF pulse on the  $y$ -axis, the spins will flip along the axis and continue dephasing at the same rate and in the same direction as shown in Figure 2.6. This implies that after a time  $TE$ , equal to twice the time from when the  $90^\circ$  pulse was switched off to the time the  $180^\circ$  pulse is applied, all spins will realign and the signal will reappear. However, it will do so at a lower strength than the original, and this is due to the energy loss from spin-spin interactions. The signal loss is described by Bloch equation (2.4), using a time constant  $T_2$ , described as the transverse relaxation time, or spin-spin relaxation time. While  $T_2$  describes the signal loss from spin-spin interactions, i.e. from the interactions with neighbouring molecules,  $T_2^*$  describes the faster signal loss from both spin-spin interactions and field inhomogeneity. The signal acquisition for a spin echo sequence, which reverses the losses associated with  $T_2^*$ , is shown in Figure 2.7.

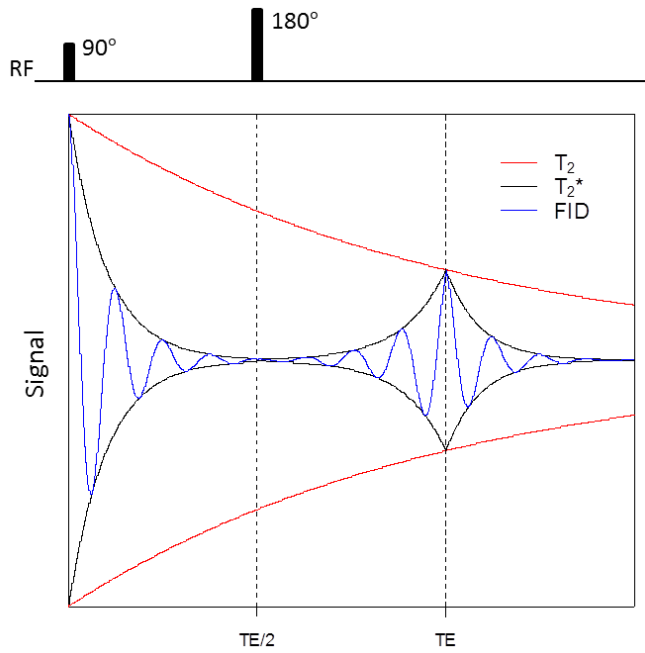


**Figure 2.7: Spin echo signal acquisition.** The signal acquired, the FID, is at a maximum after application of the  $90^\circ$  RF pulse and quickly decays at a rate defined by  $T_2^*$ . After applying the  $180^\circ$  RF pulse, the spins start to realign and the signal reappears at a time equal to twice the time between the two RF pulses, or  $TE$ . The signal reappears with a loss defined by the spin-spin relaxation time,  $T_2$ .

### 2.1.6 LOCATING THE SIGNAL

The signal acquired, the FID, is an electromotive force induced by the rotating magnetic field in a coil. It is thus not dependent on a specific location but is obtained from the entire object. In order to localise the signal, the specific area being imaged needs to be excited separately. This is done by applying gradients.

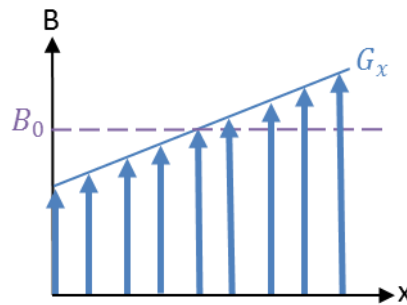


**Figure 2.8 Applying a gradient.** When a magnetic field gradient is applied in the  $x$ -direction, the magnetic field along the said direction will vary depending on position. As the Larmor frequency is dependent on magnetic field, only a specific area will be excited when applying a specific frequency.

A gradient is a spatially linear variation applied onto the static magnetic field,  $B_0$ , in either of the  $x$ ,  $y$  and  $z$  directions; as shown in Figure 2.8 for the gradient applied in the  $x$  direction,  $G_x$ . Following on from the Larmor equation (2.2), the precession frequency is dependent upon the magnetic field, and hence after applying the gradient, the precession frequency is dependent upon position. Applied gradients can be either positive, as in the case of Figure 2.8, or negative. A faster precession is experienced towards the end having a higher magnetic field, while a slower precession is experienced towards the end having a lower magnetic field.

In order to image a 3D volume, gradients in the three orthogonal directions are used. First, the slice being imaged is selected. This is done by applying a gradient  $G_z$ , also known as the slice select gradient  $G_{ss}$ , at the same time as applying an RF pulse tuned to the precession frequency of the specific slice being imaged,  $f_1$ . This RF pulse will include a narrow range of frequencies,  $\Delta f$ , which will only excite those nuclei precessing at that same frequency  $f_1 \pm \Delta f$ . As shown in Figure 2.9, the location being imaged can be chosen by altering the frequency around which the RF pulse is centred,

while the slice thickness required is dependent on both the bandwidth of the RF pulse and the applied gradient.

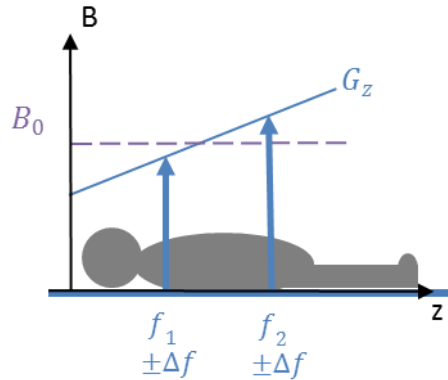


**Figure 2.9: Slice selection.** By applying a gradient in the  $z$  direction, a specific slice to image is selected by applying an RF pulse at the frequency corresponding to the slice of interest. The slice thickness is determined by the bandwidth  $\Delta f$ .

After the slice is selected, the  $x$ - and  $y$ - directions need to be encoded. When applying a gradient in the  $y$ -direction, a process of phase encoding is used, hence  $G_y$  is also known as the phase-encode gradient,  $G_{PE}$ . In phase encoding, when a gradient is applied along the  $y$ -direction, the nuclei will start precessing slower or faster, depending on the location along the gradient. This implies that the spins will start getting out of phase and this phase difference increases with time. After  $G_{PE}$  is turned off, the spins will return to precessing at the original frequency, but at the different phase angles acquired prior to the gradient being turned off as shown in Figure 2.10. This phase difference will last until either another gradient,  $G_{PE}$ , is applied, or until the MR signal in the transverse plane decays due to  $T_2$ . The location in the  $y$ -direction is thus encoded in the signal phase.

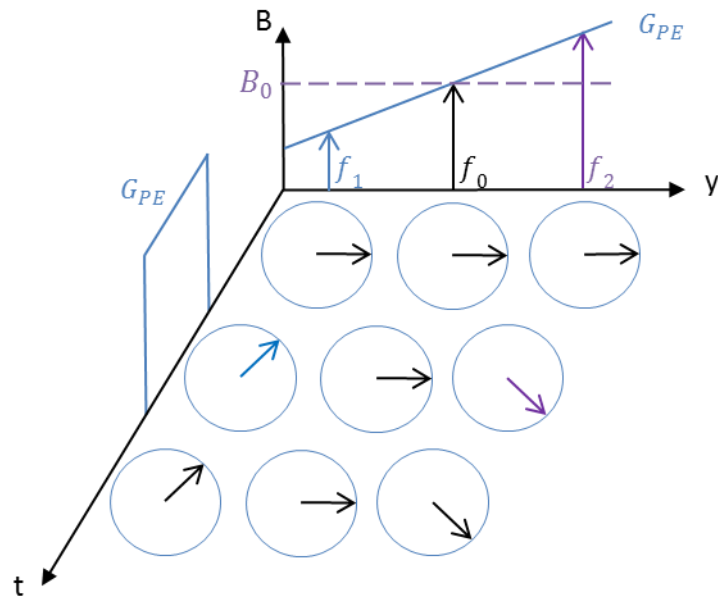


**Figure 2.10: Phase encoding.** In phase encoding, prior to applying a gradient, the spins along the y-axis (the phase encode direction) precess in the same direction. When a gradient is applied, the spins will have different energy and get out of phase from each other. Removing the gradient, brings the frequency of the spins back to the original value, however the phase difference is preserved. Location information is thus encoded in the phase of the spins.

The gradient in the x-direction,  $G_x$ , is encoded in terms of frequency and hence is known as the frequency encode gradient,  $G_{FE}$ . Frequency encoding works using the same principle shown in Figure 2.8. In this case, the gradient is kept on during signal collection. As long as the gradient is on, the nuclei experiencing different gradients will precess at different frequencies. Hence, location in the x-direction is encoded in terms of the frequency of the signal acquired.

Hence, following slice selection using  $G_{SS}$ , by combining the two gradients,  $G_{PE}$  and  $G_{FE}$ , we are able to acquire the signal for all voxels in the selected slice.

### 2.1.7 OBTAINING THE IMAGE

The signal obtained, the FID, consists of a number of sinusoids at different frequencies and phases, each representing a specific location. The location can thus be determined by using the Fourier transform to convert the signal. The Fourier transform is able to

transform any signal in terms of a sum of sinusoids with a specific frequency and phase for each.

A one-dimensional signal in time can be represented in terms of a sum of sinusoids, which can be transformed from the time- to the frequency-domain using the Fourier transform. Similarly, a two-dimensional image in space can be represented in terms of a sum of sinusoidal basis images. The two-dimensional Fourier transform in this case can be used to move from the space domain to what is known as k-space. In a similar way to how the units of frequency are defined ( $s^{-1}$ ), the units of k-space are given by  $m^{-1}$ . Each point in k-space determines an individual sinusoidal basis image, the sum of which makes up the original image.

Going back to the MR signal we obtain, the signal acquired is in k-space; with the signal in the phase encode (y) and frequency encode (x) directions being represented by  $k_{PE}$  and  $k_{FE}$  respectively. The signal acquired has both a real and imaginary component, the magnitude of which is shown together with the Fourier transformation into the acquired image in Figure 2.11.

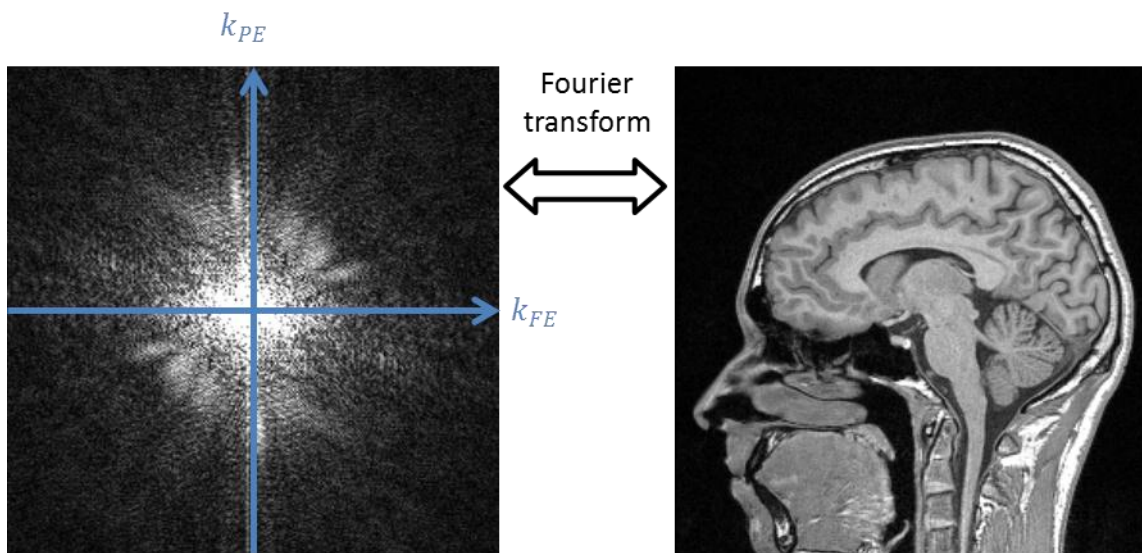


**Figure 2.11: Obtaining the image.** The acquired signal is in k-space (left). Applying the Fourier transform to k-space will give the image (right).

### 2.1.8 DIFFERENT SEQUENCES HIGHLIGHT DIFFERENT THINGS

Having explained how images are obtained, it is important to note that different sequences can be used to show different things. Thus, to obtain a specific type of image, a specific sequence is designed; consisting of RF pulses and the gradients in the x, y and z directions. Pulse sequence diagrams are drawn, defining the timing and the type of RF pulses applied and the gradients; also showing the repetition time (TR) and the echo time (TE).

The signal we acquire is dependent on the values of  $T_1$ ,  $T_2$ ,  $T_2^*$  and the proton density, with each of these values being dependent on the material being imaged. For example, materials with a higher proton density will have a greater signal and thus appear brighter. Hence a difference in signal can be observed for different materials imaged depending on how the images are weighted.

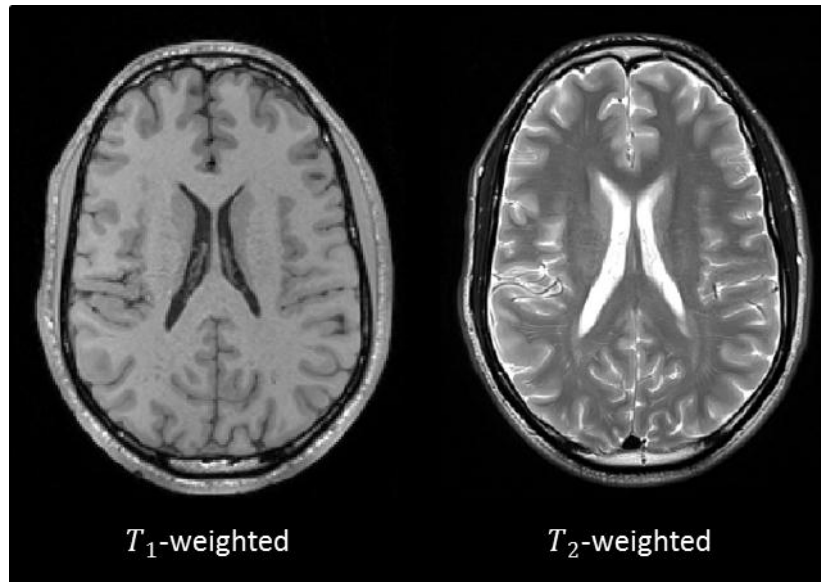


**Figure 2.12:  $T_1$ - and  $T_2$ -weighted images.**  $T_1$  and  $T_2$  weighted images vary in that areas of fluid appear dark in  $T_1$ -weighted images and bright in  $T_2$ -weighted images. White matter also appears brighter than grey matter in  $T_1$ -weighted images.

$T_1$ -weighted images have a contrast that is dependent on the recovery in longitudinal magnetisation,  $M_z$ . This can be measured in the transverse plane as  $M_z$  is related to  $M_0$  and  $T_1$  by equation (2.5); and if the RF pulse is applied before  $M_z$  has recovered, the amount of magnetisation available in the transverse plane,  $M_{xy0}$  is equal to  $M_z$ .

Hence,  $M_{xy}$  is influenced by the  $T_1$  values of the tissue being imaged. In order to ensure  $M_z$  has not recovered, a short TR is required. As mentioned,  $T_1$  is also known as the spin-lattice relaxation, which describes the energy loss to the surrounding lattice. As neighbouring molecules in fluids (the lattice) vibrate faster than the Larmor frequency, energy cannot be easily lost from spin-lattice interactions and thus fluids have a longer  $T_1$ . This implies that when the signal is tipped to the transverse plane there will be less signal available, as less of  $M_z$  would have recovered, and hence fluids appear dark in  $T_1$ -weighted images, as shown in areas of CSF in Figure 2.12.

On the other hand,  $T_2$ -weighted images are related to the spin-spin interactions and the energy loss between the surrounding spins. To ascertain that these images are not affected by values of  $T_1$ , a long TR is used such that  $M_z$  would have completely recovered to  $M_0$ , and a long TE is used such that the signal's influence by  $T_2$  would be increased. In fluids, hydrogen nuclei are free to move around and thus spin-spin interactions are very limited, implying a longer time is taken to lose energy and thus fluids have a longer  $T_2$ . This implies that the signal in fluids is stronger and fluids appear bright in  $T_2$ -weighted images, as shown in areas of CSF in Figure 2.12.

### 2.1.9 DIFFUSION WEIGHTED IMAGING

In order to understand diffusion-weighted imaging (DWI), the concept of diffusion needs to be first explained. Diffusion of water molecules, also referred to as Brownian motion, describes how all water molecules move around in a random fashion, resulting from collision with other molecules. This in turn implies that, provided there is no barrier, water molecules will diffuse outwards according to a Gaussian distribution described by Einstein in equation (2.6).

$$\langle r^2 \rangle = 6D\tau \quad (2.6)$$

where  $\langle r^2 \rangle$  is the mean-squared displacement, D is the diffusion coefficient of the substance and  $\tau$  is the diffusion time.

As the MR signal results from the hydrogen present in water molecules, diffusion can be imaged by using a specific sequence. A method for measuring the effect of diffusion was first proposed by Carr and Purcell in 1954<sup>6</sup>, while Stejskal and Tanner introduced

the basic pulsed gradient spin-echo (PGSE) sequence, forming the basis for diffusion sequences today, in 1965<sup>7</sup>.

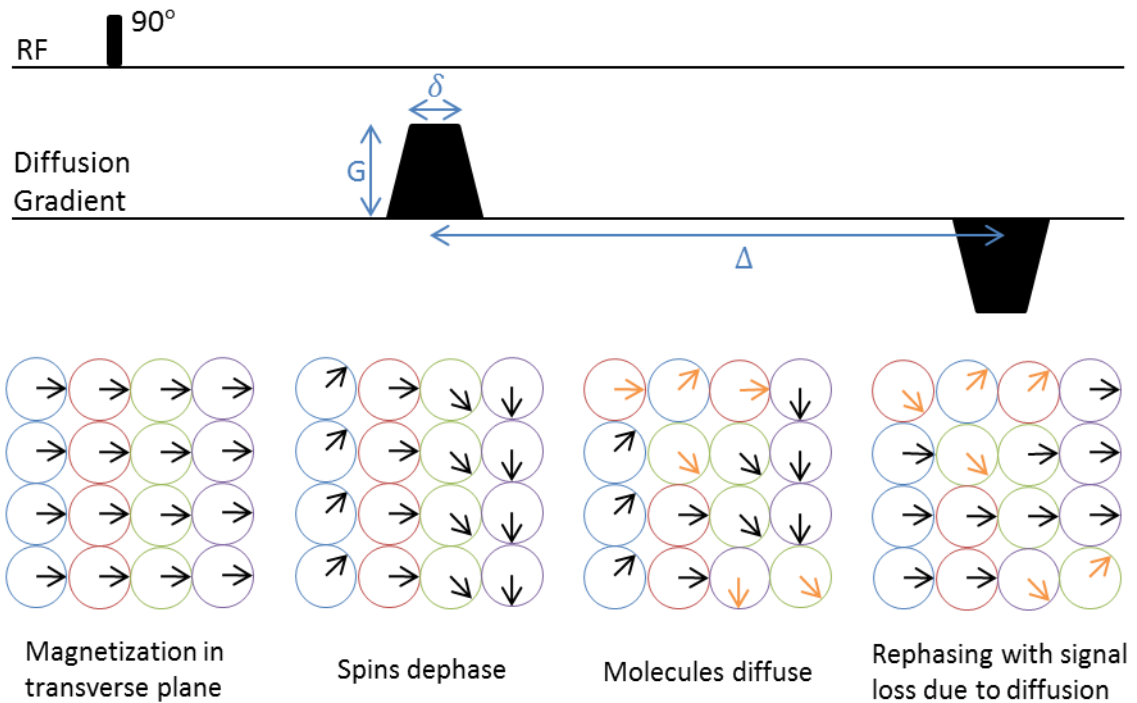


**Figure 2.13: Diffusion-weighted imaging.** After the RF pulse is applied the spins are tipped into the transverse plane. When a gradient is applied, the spins dephase with each area of tissue experiencing a different field getting out of phase from each other. During the time  $\Delta$ , molecules will diffuse such that the spins move from one area to another. An equal and negative gradient is then applied such that the spins would realign. However, due to the diffusion which would have occurred, some spins will experience a different gradient to the original and will thus not rephase completely. This results in a signal loss.

In order to apply diffusion-sensitization, a bipolar gradient is introduced after RF excitation and before signal acquisition. This can be done by either applying a positive gradient followed by an equal but negative gradient as shown in Figure 2.13, or by applying two equal positive gradients with a  $180^\circ$  RF pulse in between. When the first gradient is applied, spins will dephase according to the gradient applied. Following a time  $\Delta$ , the molecules would have diffused such that some of the spins would have moved with respect to the gradient. When the negative gradient is then applied, rephasing will occur, however the diffused molecules will experience a different

gradient to the original and will thus not realign and the phase difference results in a signal loss. Diffusion is thus measured in terms of signal loss.

The diffusion effect and thus the signal loss is dependent on four parameters: the time between the gradient pulses  $\Delta$  – a longer time will imply more diffusion as given by equation (2.6) and hence less signal; the strength and duration of the gradient pulse  $G$  and  $\delta$  – a larger gradient or longer gradient length will imply increased spin dephasing and hence a larger signal loss when rephasing; and a diffusion constant  $D$  which is material dependent – a larger  $D$  implies water molecules can diffuse a larger distance per unit time as given by equation (2.6) and hence a larger signal loss. The relationship between these four parameters and the signal is shown in equations (2.7) and (2.8).

$$\ln \frac{S}{S_0} = -bD \quad (2.7)$$

where  $S$  is the signal with diffusion weighting,  $S_0$  is the signal without diffusion weighting,  $D$  is the diffusion coefficient of the material and  $b$  is the diffusion weighting defined in equation (2.8).

$$b = \gamma^2 G^2 \delta^2 \left( \Delta - \frac{\delta}{3} \right) \quad (2.8)$$

where  $b$  is the diffusion weighting,  $\gamma$  is the gyromagnetic ratio of protons,  $G$  is the gradient amplitude, and  $\left( \Delta - \frac{\delta}{3} \right)$  is the diffusion time – with  $\delta$  being the gradient duration and  $\Delta$  the gradient separation, as shown in Figure 2.13.

Following from equation (2.7), the diffusion constant,  $D$ , can be measured by measuring the signal with no diffusion weighting ( $b = 0$ ) and with diffusion weighting. The diffusion weighting,  $b$ , needs to thus be changed, in principle by altering  $G$ ,  $\delta$  or  $\Delta$ . In practice changing  $\Delta$  alters the echo time, resulting in a signal which is both diffusion- and  $T_2$ - weighted; and increasing  $\delta$  is limited by the pulse sequence timing setup. Hence, when measuring the signal with multiple  $b$ -values, a change in the gradient strength is normally applied such that the variation in signal loss is only due to the diffusion effect. While using two points is enough to measure the diffusion coefficient, more  $b$ -values can be acquired and a least square fit applied so as to increase the

signal-to-noise ratio (SNR). That said, a more efficient way of improving SNR is to take multiple acquisitions at the optimal b-value, rather than using multiple b-values. SNR is also maximised by making  $G$  as large as possible and making  $\Delta$  as small as possible to minimise the echo time.

As such, the diffusion coefficient measured is influenced by a number of factors, and hence the measured diffusion coefficient is called the apparent diffusion coefficient (ADC). The diffusion of water in tissue is more restricted than that in fluid areas and thus a smaller signal loss occurs at higher b-values in tissue as compared to fluid areas, where diffusion is high. As shown in Figure 2.14, the resultant ADC image shows areas of fluid, such as areas of CSF, as bright; while other more compact tissues appear dark. ADC is measured in  $mm^2s^{-1}$ .

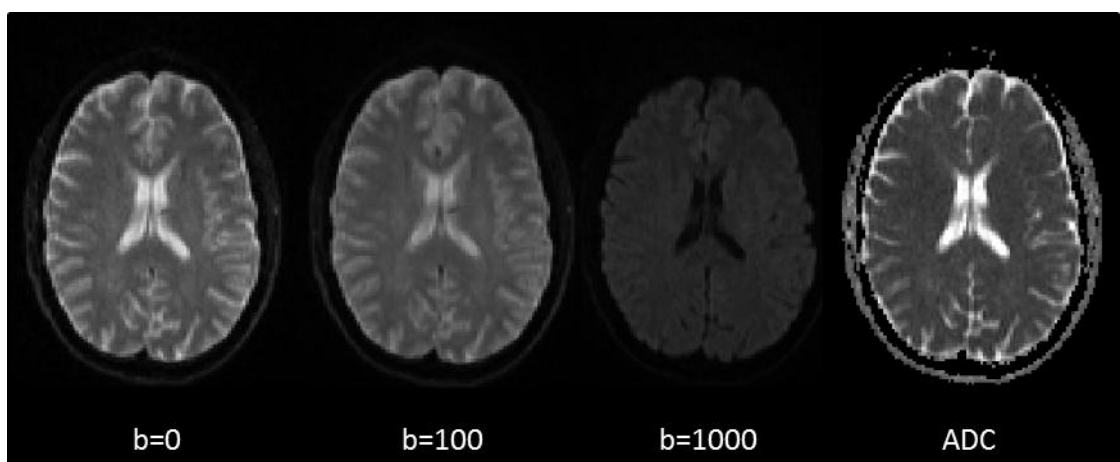


**Figure 2.14: Diffusion-weighted images.** At  $b=0$  there is no diffusion weighting, and the image is essentially a  $T_2$  weighted image. Diffusion weighting can be applied, with an increased diffusion weighting ( $b=1000$ ) implying more signal loss and hence appearing darker, particularly in areas where diffusion is higher such as in areas of CSF. An ADC image is calculated from a  $b=0$  image and at least one diffusion weighted image, commonly  $b=1000$ .

When measuring ADC as described above, the diffusion gradient is applied along one direction. Thus ADC is only able to measure diffusion along one direction – which is not an issue if it is assumed that diffusion in any given direction is random. While ADC is a good measure for isotropic diffusion, it is unable to define anisotropic diffusion. An issue thus arises in imaging tissue which is anisotropic; and hence the concept of an

average ADC over three orthogonal directions was introduced, as shown in equation (2.9). For the purpose of this thesis, from here on ADC refers to the averaged measure of diffusion along three orthogonal directions.

$$ADC_{av} = \frac{ADC_x + ADC_y + ADC_z}{3} \quad (2.9)$$

where  $ADC_{av}$  is the averaged ADC over three orthogonal directions:  $ADC_x$  – the ADC measured in the x-direction,  $ADC_y$  – the ADC measured in the y-direction, and  $ADC_z$  – the ADC measured in the z-direction.

### 2.1.10 INTRA-VOXEL INCOHERENT MOTION

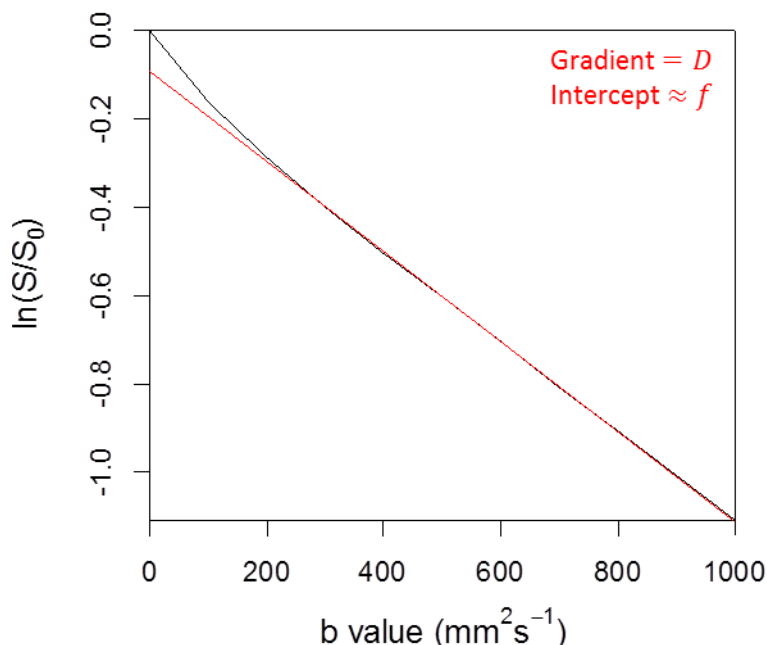


**Figure 2.15: IVIM graph.** While ADC images assume a linear fit for all points, it can be observed that at lower b-values a different fit exists. IVIM applies a biexponential to the data such that the gradient to the fit at higher b-values (shown in red) gives the slow diffusion coefficient,  $D$ ; the intercept of the same fit is an approximation for the value of the perfusion fraction,  $f$ ; and the fit at the lower b-values gives the fast-diffusion coefficient,  $D^*$ .

While in measuring the ADC, it is assumed that the diffusion coefficient is linear across all b-values and is thus modelled as a single exponential, in practice the signal has a non-linear behaviour, both at low b-values ( $< 200\text{mm}^2\text{s}^{-1}$ ) as shown in Figure 2.15 as well as at high b-values ( $> 2000\text{mm}^2\text{s}^{-1}$ )<sup>8</sup>. Focusing on the signal at low b-values,

intra-voxel incoherent motion (IVIM) suggests applying a bi-exponential fit to data<sup>9</sup>. The model suggests that two components give rise to the diffusion effect; random Brownian motion of molecules in tissue (referred to as the slow diffusion component) and the flow of water in the randomly oriented micro-vascular network (referred to as the fast diffusion component). The IVIM model is given by equation (2.10).

$$\frac{S}{S_0} = (1 - f)e^{-bD} + fe^{-b(D+D^*)} \quad (2.10)$$

where  $S$  is the signal intensity at a given b-value,  $S_0$  is the signal intensity without diffusion-weighting,  $D$  is the slow diffusion coefficient of water molecules in tissue,  $D^*$  is the fast pseudo-diffusion coefficient of water in blood capillaries, and  $f$  is the fraction of the total DWI signal which arises from the latter compartment.

In the brain the fast diffusion coefficient,  $D^*$  is one order of magnitude higher than the slow diffusion coefficient  $D$ <sup>10</sup>. As shown in the model in Figure 2.15, the presence of the perfusion component at low b-values ( $< 200\text{mm}^2\text{s}^{-1}$ ) has an effect on the measured diffusion coefficient. In practice, the perfusion fraction,  $f$ , in the brain is small, and the value of  $D$  is lower than that of ADC – which measures the gradient as a linear fit to all b-values acquired.

### 2.1.11 DIFFUSION TENSOR IMAGING

While the averaged ADC deals with the issue of measuring diffusion in an anisotropic medium, it does not measure the anisotropy itself. The importance of measuring anisotropic diffusion lies in the fact that anisotropy is present in biological tissue, where water diffusion may have a preferred direction – such as along fibre tracts. Imaging the directionality of this diffusion may give an indication of the biological architecture and organisation of the tissue. Diffusion tensor imaging (DTI)<sup>11</sup> aims to determine such directionality in order to attempt to build an image of the underlying structure.

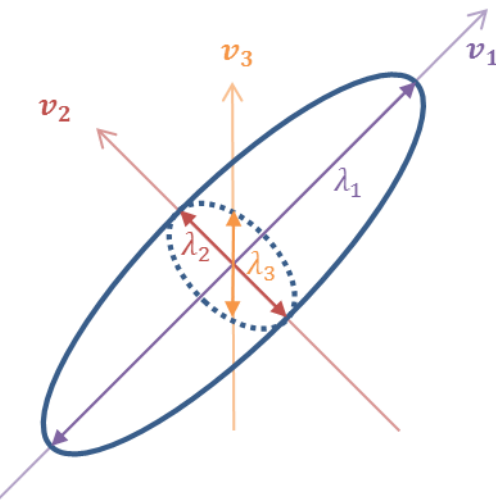


**Figure 2.16: Defining an ellipsoid.** In order to define an ellipsoid six parameters are required. Three describe the lengths of the three axes and are known as the eigenvalues  $\lambda_1$ ,  $\lambda_2$  and  $\lambda_3$ ; and three describe the orientation of the ellipsoid in space and are known as the eigenvectors  $v_1$ ,  $v_2$  and  $v_3$ .

Isotropic diffusion in the shape of a sphere can be defined using one parameter – the radius. On the other hand, anisotropic diffusion in the shape of an ellipsoid requires six parameters – three determine the shape of the ellipsoid (the shortest, the longest and the middle axes) and three define the orientation in 3D space, as shown in Figure 2.16. The three parameters determining the shape of the ellipsoid are the eigenvalues  $\lambda_1$ ,  $\lambda_2$  and  $\lambda_3$ . The three parameters defining the orientation of the ellipsoid are the eigenvectors  $v_1$ ,  $v_2$  and  $v_3$ . In order to measure these six parameters, a minimum of six measurements along arbitrary axes are required. Using DTI, a minimum of six measurements are therefore required in addition to the b-zero signal and are defined in equation (2.11).

$$\bar{D} = \begin{bmatrix} D_{xx} & D_{xy} & D_{xz} \\ D_{yx} & D_{yy} & D_{yz} \\ D_{zx} & D_{zy} & D_{zz} \end{bmatrix} \quad (2.11)$$

where  $\bar{D}$  is the diffusion tensor, with  $D_{xy} = D_{yx}$ ,  $D_{zx} = D_{xz}$  and  $D_{zy} = D_{yz}$ ;  $D_{xx}$ ,  $D_{yy}$  and  $D_{zz}$  are the diffusion measures along the three orthogonal axes; and the other diffusivities being described along correlations of two of the orthogonal axes.

As the diffusion tensor matrix is a symmetric matrix, the eigenvalues correspond to the diagonal of matrix  $\bar{\bar{D}}$ . In order to evaluate  $\bar{\bar{D}}$ , equation (2.7) cannot be used as it is only valid for isotropic diffusion. A different equation needs to be employed in anisotropic diffusion as shown in equation (2.12).

$$\frac{S}{S_0} = e^{-b\bar{g}^T \bar{\bar{D}} \bar{g}} \quad (2.12)$$

where  $S$  is the signal with diffusion weighting,  $S_0$  is the signal without diffusion weighting,  $b$  is the diffusion weighting defined in equation (2.8),  $\bar{g}$  is a unit vector pointing in the direction of the diffusion gradient pulses, and  $\bar{\bar{D}}$  is the diffusion tensor.

Once the diffusion tensor is constructed, the mean diffusivity (MD) is measured as the average of the sum of eigenvalues, which is also the mean of the trace of  $\bar{\bar{D}}$  and is shown in equation (2.13). MD is in practice very similar to ADC in value, and has the same units. The basic difference is that while ADC is measured using DWI as an average of three directions, MD represents a diffusion measurement using DTI and thus a minimum of six directions would have been used to construct the diffusion tensor from which MD is extracted.

$$MD = \frac{\lambda_1 + \lambda_2 + \lambda_3}{3} = \frac{D_{xx} + D_{yy} + D_{zz}}{3} \quad (2.13)$$

where MD is the mean diffusivity,  $\lambda_1$ ,  $\lambda_2$  and  $\lambda_3$  are the eigenvalues with  $\lambda_1 > \lambda_2 > \lambda_3$ , and  $D_{xx}$ ,  $D_{yy}$  and  $D_{zz}$  are the diffusion coefficients in the x, y and z directions.

The second important measurement in DTI is anisotropy, and the most commonly calculated parameter to represent anisotropy is the fractional anisotropy (FA), defined in equation (2.14). FA is defined such as to have values between 0 and 1, a value of 0 representing isotropy and a value of 1 representing maximum anisotropy, where the ellipsoid is actually a line and hence has only one non-zero eigenvalue.

$$FA = \sqrt{\frac{3}{2} \left( \frac{(\lambda_1 - MD)^2 + (\lambda_2 - MD)^2 + (\lambda_3 - MD)^2}{\lambda_1^2 + \lambda_2^2 + \lambda_3^2} \right)} \quad (2.14)$$

where FA is the fractional anisotropy,  $\lambda_1$ ,  $\lambda_2$  and  $\lambda_3$  are the eigenvalues, and MD is the mean diffusivity as defined in equation (2.13).

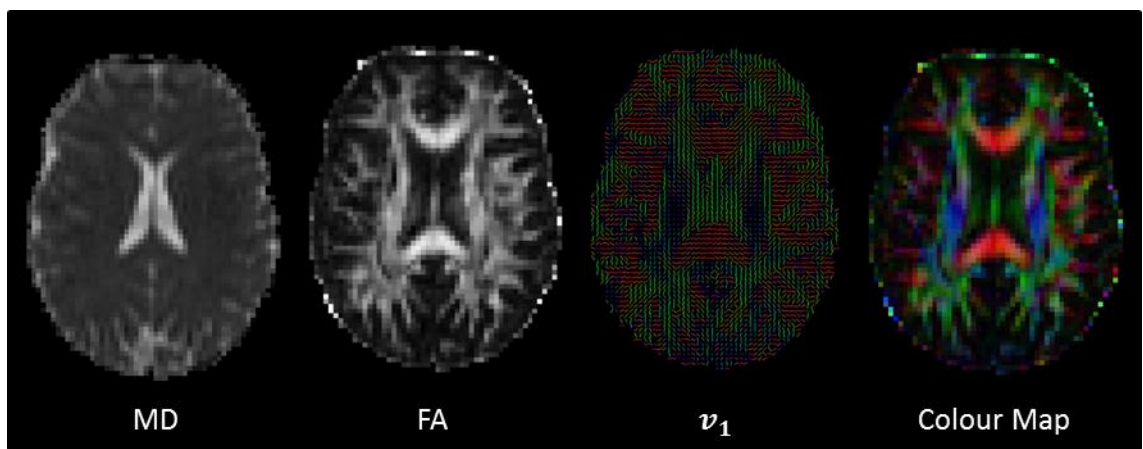


**Figure 2.17: DTI parameters.** The main DTI parameters calculated are the mean diffusivity (MD) and fractional anisotropy (FA). MD and ADC are similar and only differ in terms of the number of directions in which they are calculated. FA gives an indication of the anisotropy present in a given voxel. Using  $v_1$ , which shows the orientation for the principal eigenvalue, a colour map of the FA values can be built such that the orientation can be visualised. Red represents left to right, green represents anterior to posterior, and blue represents superior to inferior orientations.

FA characterises the anisotropy for the diffusion in the voxel but does not give an indication of the direction of diffusion. This is provided by the eigenvector,  $v_1$ , which is related to the principal eigenvalue,  $\lambda_1$ , such that a colour-coded map may be built on top of the FA showing the direction of diffusion. Conventionally, red represents diffusion between left and right, green represents diffusion anterior-posterior, and blue represents diffusion superior-inferior. By observing the direction of diffusion and the FA, DTI is able to reconstruct an image of the white matter fibres. Reconstruction of white matter pathways is done through tractography, a method which was first described in 1999<sup>12–15</sup> and is discussed in more detail in <sup>16,17</sup>. Example DTI images are shown in Figure 2.17.

### 2.1.12 IMAGE ARTEFACTS

While all MR images may suffer from artefacts, diffusion imaging is particularly sensitive to motion due to the strong diffusion gradients. Motion can result in phase errors, which introduce ghosting artefacts. In order to mitigate this, the echo planar imaging (EPI) acquisition method is used. In this way, all of k-space is acquired in one scan such that a phase shift would affect the whole of k-space and should not have an

effect on the magnitude obtained after the Fourier transform is applied. This method, however, limits the image resolution and also introduces susceptibility errors. Susceptibility artefacts result from magnetic field inhomogeneity, particularly at tissue-air interfaces, and become worse with increased field strength.

Another artefact which is an issue in diffusion imaging involves the rapid switching of large magnetic field gradients, which induce eddy currents in the conductive parts of the scanner. The eddy currents produce additional unwanted magnetic fields, which alter the magnetic field at the sample from the value applied for a specific b-matrix. The eddy currents' magnetic field also decays slowly during readout, causing geometrical distortions of diffusion images.

Image artefacts, such as those caused by eddy currents, may be taken into account during data processing so as to minimise their effect. While the next section does not go into the detail of the data processing methods which can be employed to reduce such artefacts, it describes the process through which data obtained from the scanner is analysed in order to study the research question and draw meaningful conclusions.

## 2.2 Data processing

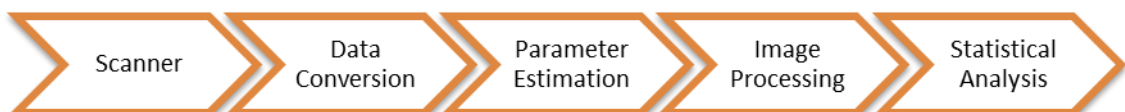


**Figure 2.18: Data processing.** Once data is obtained from the scanner, it needs to be converted into a format which can be easily processed. The parameters related to the data acquisition can then be calculated, followed by any necessary image processing and statistical analysis in order to test the experimental hypothesis.

Once an image is acquired on an MR scanner as described in the previous section, the data is made available such that it can be viewed and analysed. Clinical data can be easily accessed using a picture archiving and communication system (PACS). However,

if any more information is required other than is available on the system, particularly in terms of answering a specific research hypothesis or clinical question, images may need to be processed further through additional tools. This section outlines the process of obtaining data from the scanner and describes tools available to analyse such data, according to the data processing steps shown in Figure 2.18.

### 2.2.1 DATA TYPES AND DATA CONVERSION

As imaging tools became an important component of patient management, and particularly as multiple images needed to be exchanged from one system to another, a need for standardising medical images across hospitals arose. In order to alleviate compatibility issues, the digital imaging and communications in medicine (DICOM) format was created. Although DICOM is the standard clinical image format, some manufacturers do use specifically developed formats, such as the Philips PAR/REC format, which would still however be compatible with the DICOM format.

A DICOM image consists of two parts, the header – which contains patient and scan details, and the image data. While it has solved issues of compatibility in the clinic, the defined standard is broad and may be difficult to work with. Hence, more compact image formats tend to be applied in research. More specifically, most image processing software will use the ANALYZE or NIfTI<sup>18</sup> formats, with NIfTI being the most commonly used format.

Various software exist that convert data from DICOM to NIfTI. As well as being dependent on the computer platform and operating system in use, the choice of software may be affected by what scanner the images are coming from. Some software may work better with scanners from one manufacturer over another. Data conversion software available and explored in this work include MRIConvert<sup>19</sup>, dtoa<sup>20</sup>, dcm2nii<sup>21</sup>, TractoR<sup>22</sup> and SPM<sup>23</sup>.

### 2.2.2 PARAMETER ESTIMATION

Diffusion imaging parameters may be output directly from the scanner, and hence available after data conversion. However, for the purpose of image analysis, it may be

important to estimate the parameters using a specific method and hence different software, such as MATLAB<sup>24</sup>, may be used.

#### 2.2.2.1 ADC

ADC is generally calculated directly by the scanner. However, no standard way of calculating this parameter exists and the exact equation used is generally not published by the manufacturer<sup>25</sup>. Hence, in order to be able to reproduce the exact results across different scanners it may be important to calculate the ADC images using a specific script. ADC images from the b-value images output by the scanner can thus be produced by using the definition of ADC given in equation (2.7) and by averaging the measurement over the three orthogonal directions imaged by the scanner.

#### 2.2.2.2 *D* and *f*

IVIM parameters are generally not estimated by the scanner directly but need to be calculated separately. Parameters given by the model in equation (2.10), can be calculated in different ways as mentioned in<sup>26</sup>.

#### 2.2.2.3 MD and FA

DTI parameters are normally calculated by the scanner, however, similar to ADC, the method employed is not standardised. In particular, one might want to correct for eddy currents or image registration issues. Therefore MD and FA can be calculated through own scripts or by using diffusion imaging processing software such as FSL<sup>27</sup>.

### 2.2.3 IMAGE PROCESSING

Once images are obtained from the scanner and the parameters calculated, images can be further processed through other image analysis software. The specific image processing carried out is dependent on the analysis required. Some analyses require registration and/or segmentation, described in the next sections. Analysis may also include other mathematical and statistical operations. Using MATLAB, images can be imported in a matrix format, which can be easily manipulated in order to conduct the necessary measurements.

### 2.2.3.1 Registration

Image registration is an important image analysis tool. It allows for comparison of two images and reduces problems related to motion. Various techniques of image registration exist and include linear and non-linear methods, which have been implemented in software such as SPM<sup>23</sup> and FSL<sup>27</sup>.

### 2.2.3.2 Segmentation

Image segmentation can be important in brain image analysis. In particular, SPM and FSL can be used to segment grey and white matter while other software such as FreeSurfer<sup>28</sup> is able to carry out cortical and subcortical segmentation. Automated image segmentation is likely to introduce some errors and a degree of manual segmentation may help improve the results.

## 2.2.4 STATISTICAL ANALYSIS

After having estimated the diffusion parameters and processed the images so as to obtain the required measurements, statistical analysis is generally performed in order to infer possible conclusions from the analysis carried out. Various statistics software, such as R<sup>29</sup>, exist to perform these tasks.

## 2.3 MRI in the Clinic

In the beginning of this chapter we mentioned why MRI is considered to be a very useful imaging tool – in that it is both safe and non-invasive. In this section we explore the safety concerns and limitations of MRI, and mention the basic clinical protocols available together with an outline of the uses of diffusion imaging in the clinic.

### 2.3.1 MRI SAFETY

The main concern for MRI safety is related to the high magnetic field and radio frequency exposure, and a number of safety practices have been issued as guidance in order to mitigate risks<sup>30</sup>. While the presence of a large static magnetic field has not been shown to post a health concern in itself, its presence implies a number of safety issues. Very few fatalities have resulted from MRI. The main cause of such accidents was the effect of the static magnetic field on implants such as cardiac pacemakers, and

ferromagnetic objects which can act as a projectile. Furthermore, the effect of large field strengths has still not been studied thoroughly and current recommendations include applying a maximum field strength of 4T on foetuses and infants, while suggesting caution in experimental setups with field strengths higher than 8T<sup>31</sup>.

RF radiation may generate heat due to the increased energy deposited in the molecules. The increase in temperature is small ( $\approx 0.5^{\circ}\text{C}$ ) and can be controlled by altering the specific absorption ratio, a measure which needs to take into account both field strength and patient weight.

Another safety issue, which needs to be considered in the clinic, is that the time varying magnetic fields introduced by the gradients may cause peripheral nerve stimulation. Apart from this, the noise generated by these gradients can exceed safety limits, and ear plugs are generally used by the patient and anyone else in the scanner room during scanning.

While the above concerns need to be taken into account in the clinic, and caution is important, the safety of MRI is much greater than that of other imaging modalities such as PET, X-ray or CT, which all use ionising-radiation.

### 2.3.2 LIMITATIONS OF MRI

The main limitation of MRI is the low sensitivity. As described in the above sections, MRI requires a large number of nuclei to image what is known as a voxel. The size of the voxel therefore offers the limit which can be imaged – implying voxels may include in them more than one type of tissue, and particularly at boundaries MRI is susceptible to partial volume effects. This means that fine structures cannot be resolved using MRI. While voxel size can be reduced to increase resolution and decrease partial volume effects, the reduction in voxel size is limited by scan time and SNR. Another limitation for MRI in the clinic is its cost. MRI is more costly than X-ray, CT and ultrasound, both in financial terms and in terms of scanning time. In addition, in order to obtain good quality images it is important for the patient to cooperate and lie still in the scanner. This may be a challenge, particularly when imaging young children, and sedation or anaesthesia may be necessary.

### 2.3.3 BASIC CLINICAL BRAIN IMAGES

In the brain, basic clinical imaging will include  $T_1$  and  $T_2$ -weighted images in the coronal, sagittal and axial planes. Post-contrast imaging, generally gadolinium, is also a common technique used in order to detect pathologies affecting the blood-brain barrier. Gadolinium affects the MRI signal by shortening  $T_1$  values and thus makes the areas it reaches appear brighter. DWI is also a common clinical imaging sequence, normally carried out in the axial plane.

### 2.3.4 DIFFUSION IMAGING

As stated, diffusion imaging is widely used both as a research tool and in the clinic. In particular it is beneficial in acute and chronic stroke, in assessing brain development, multiple sclerosis, epilepsy, neurodegenerative disorders, psychiatric disorders and brain tumours. Clinically, it is used both in the assessment of diseases and for neurosurgical planning. As this thesis focuses on diffusion imaging in brain tumours, the next chapter provides a background to cancer and in particular paediatric brain tumours prior to exploring current research work carried out in diffusion imaging in brain tumours.

## Chapter 3 CANCER AND PAEDIATRIC BRAIN TUMOURS

The main aim of this chapter is to provide a background of cancer biology, followed by an overview of brain anatomy. This chapter then focuses on paediatric brain tumour classification and treatment, concluding with a summary of imaging modalities used in brain tumour imaging.

### 3.1 Cancer

#### 3.1.1 BACKGROUND

Cancer is the second leading cause of death after cardiovascular disease. It is said that more than one in three people will develop cancer in their lifetime and it is thus not surprising that cancer research charities are amongst the charities receiving most income in the UK. Funding is driven by the general public's awareness of the importance of improving cancer treatment, implying a need for understanding how cancer develops, evolves and reacts to treatment; and highlights how public engagement can have a considerable impact on scientific research.

#### 3.1.2 A BRIEF HISTORY

The word “cancer” is Latin for the ancient Greek word “karkinos”, meaning crab, and was first used to describe the disease by Hippocrates (460 BC – c. 370 BC). Although this is the earliest mention of the term, the disease itself was known from Egyptian times (1500 BC)<sup>32</sup>. Different theories on how cancer developed were proposed throughout the centuries, but the main advances in cancer research happened following the discovery of the double helix DNA structure in 1953. In order to understand how cancer forms and develops we need to first start with the basic unit of life, the cell.

#### 3.1.3 SOME CHARACTERISTICS OF CELLS

Two types of cells exist, one with and one without a nucleus, and here we are interested in the cell type of multi-cellular organisms - eukaryotic cells, i.e. cells which

contain a nucleus. The nucleus is an organelle inside a cell which contains the genetic material stored in the deoxyribonucleic acid (DNA) molecule. The basic structure of a cell together with a description of some of the organelles is given in Figure 3.1.

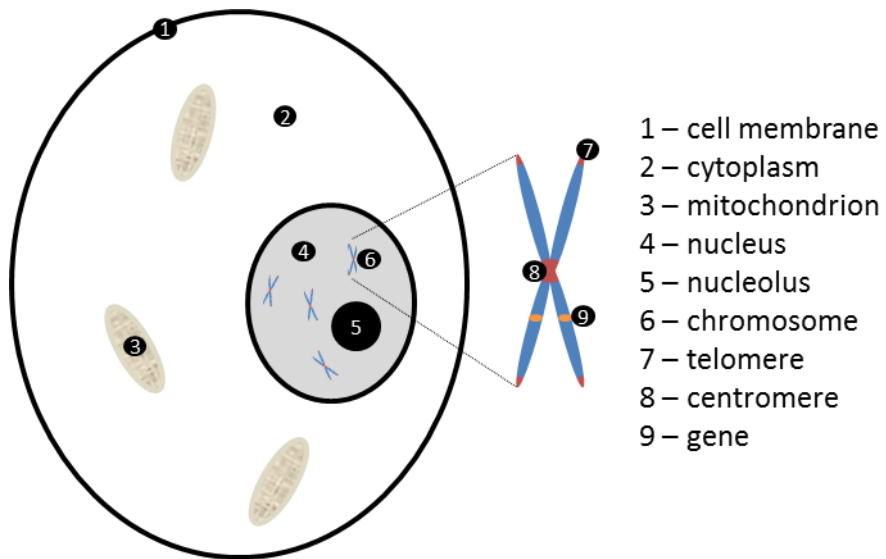


**Figure 3.1: Structure of a cell.** A eukaryotic cell consists of (1) a *cell membrane* that separates the intracellular space from the extracellular space, protecting the cell by controlling the movement of substances in and out of the cell; (2) the *cytoplasm*, the part of the cell held within the cell membrane and containing the cytosol (the intra-cellular fluid) and all organelles, excluding the nucleus; (3) the *mitochondria*, which generate most of the cell's energy and are involved in controlling cell growth and the cell cycle; and (4) the *nucleus*, which contains most of the cell's genetic material. The nucleus contains (5) the *nucleolus*, which is responsible for assembling ribosomes (organelles which synthesize proteins within the cell); and (6) the *chromosomes*, which are the organised structure of the DNA. Chromosomes include (7) the *telomeres*, which are repeated strands of DNA at the ends of the chromosome, responsible for protecting it; (8) the *centromere*, which joins together two identical copies of the chromatid to form the chromosome, and helps keep the chromosomes aligned during cell division; and (9) *genes*, which are segments of DNA that represent a specific trait. Note that the centromere is not normally in the centre of the chromosome and the short arm is referred to as the p region while the longer arm is referred to as the q region.

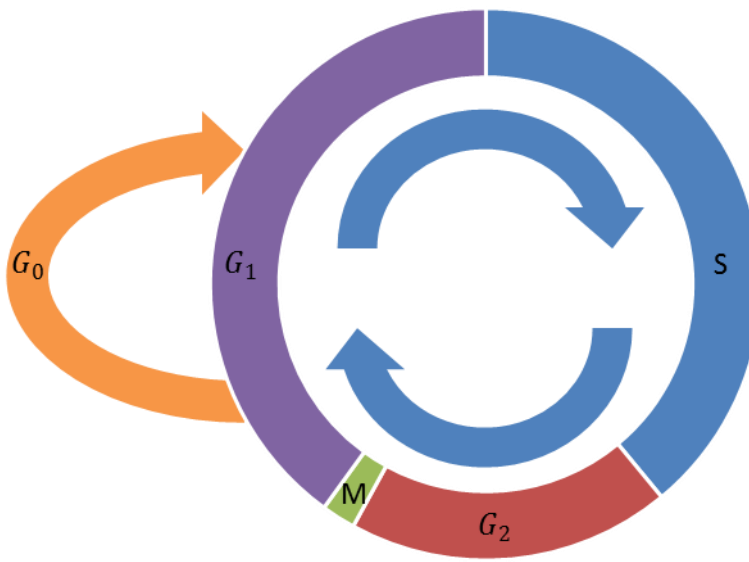


**Figure 3.2: The cell cycle.** Cells which are not in a replicative stage are said to be in quiescence in the  $G_0$  stage. Once a cell moves back into the cell cycle, at the  $G_1$  stage, it starts to increase in size and the cell gets ready for DNA synthesis by preparing the necessary components. The cell then moves in the synthesis stage, the S-stage, and DNA synthesis occurs such that all chromosomes are replicated. In the mitotic phase, the M-stage, nuclear division occurs, following which the cell divides in two daughter cells. Checkpoints exist during each of the stages to ensure that replication occurs without errors.

One of the basic requirements of a cell is the ability to replicate. The cell division cycle occurs in a number of stages, shown in Figure 3.2. A cell that is in a non-dividing stage is said to be in the  $G_0$  stage. Once a cell is dividing it will enter the  $G_1$  gap stage where cells grow while carrying out normal metabolism. The cell then moves to the S-phase or the DNA synthesis-phase where DNA replication occurs and chromosomes duplicate inside the nucleus. From the S-phase, the cell enters the  $G_2$  gap stage, where the cell continues to grow and prepares for its actual division. In the M-phase or mitosis-phase, the nucleus in the cell will separate the duplicated chromosomes into two nuclei. The cell can then divide into two daughter cells.

The cell cycle is complex, and findings from a study in 1970<sup>33</sup> suggested that the cell cycle is regulated by certain factors. A number of mechanisms, defined as checkpoints, exist so as to ensure that a perfect copy of the cell results after cell division<sup>34</sup>. A checkpoint detects errors and makes sure the cell cycle is stopped if one is identified.

For example, in response to DNA damage or failure in DNA replication, protein kinases are activated which prevent the cell from going into the mitotic phase<sup>35</sup>. When these checkpoints fail due to genetic mutations, a cancer cell may form.

### **3.1.4 FORMING A CANCER CELL**

Cancer is a genetic disease and a cancer cell forms after a number of genetic mutations. The genes which drive tumourigenesis, the formation of a tumour, can be divided into three categories: tumour suppressor genes, oncogenes and genomic stability genes. Tumour suppressor genes suppress the formation of tumour, oncogenes induce the loss of growth control, and genomic stability genes keep mutations to a minimum by identifying DNA damage and correcting errors made during normal DNA replication. While these three categories represent the genes that contribute to forming a cancerous cell, specific genes may belong to more than one of these categories, and an example of one such gene is the TP53 gene.

The TP53 gene is primarily a tumour suppressor gene and has significant consequences once mutated. TP53 encodes the polypeptide p53 – a transcription factor which activates genes involved in the regulation of the cell cycle and apoptosis (programmed cell death). When TP53 is activated as a response to stress or senescence, it forces the cell to stop growing and can also force apoptosis. Secondly, the gene is activated by proteins responding to DNA damage, stopping replication in the case of severe damage. If the gene is not activated, a loss in genomic stability occurs, allowing for more mutations to occur. Thirdly, some mutations to the TP53 gene result in a gain of an oncogenic function. While this gene is the most frequently mutated gene in adult cancer, it is rare in childhood cancer.<sup>36</sup>

Most cancer mutations are developed during one's lifetime. However, some forms of cancer mutations are inherited, which makes it more likely for the person to develop the disease. The fact that certain types of cancer are prevalent in certain families implies that genetic mutations that induce cancer can be inherited, and the loss of tumour-suppressor genes is one such mutation. Inherited mutations are termed germline mutations and these mutations are present at the formation of the embryo.

Mutations which occur in the body are termed somatic mutations. Somatic mutations occur in specific tissue in the body and may result in cancer, however these mutations are not passed on to any offspring.<sup>37</sup> Genetic mutations forming cancer cells may occur as a result of exposure to carcinogenic chemicals, ionizing radiation, as well as a variety of tumour-inducing viruses<sup>38</sup>. In most cancers, all cells arise from a single cell which then proceeds to replicate uncontrollably. While cancer cells vary widely they may share some of the features described in Hanahan and Weinberg's "Hallmarks of Cancer"<sup>39,40</sup> and summarised in the next section.

#### **3.1.5 HALLMARKS OF CANCER**

**Figure 3.3: Hallmarks of cancer.** Initially six hallmarks of cancer were suggested: sustaining proliferative signalling, evading growth suppressors, enabling replicative immortality, activating invasion and metastasis, inducing angiogenesis, and resisting cell death. These were expanded to include four new hallmarks: avoiding immune destruction, tumour-promoting inflammation, genome instability and mutation, and deregulating cellular energetics. (Adapted from Hanahan and Weinberg, 2011.<sup>40</sup>)

#### *3.1.5.1 Sustaining proliferative signalling*

As mentioned, a cancer cell will replicate uncontrollably. This is in part due to the ability of cancer cells to sustain proliferative signalling. Whereas in healthy tissue the cell cycle is controlled by growth-promoting signals, in cancerous tissue cells gain the ability to take control of these signals, either by producing the required growth factors, or by stimulating normal cells around the tumour stroma to supply the required growth factors. In this way a positive feedback signalling loop is created such that tumour proliferation may continue.

#### *3.1.5.2 Evading growth suppressors*

Cells respond to both positive growth-inducing signals and signals which negatively regulate proliferation. These growth suppressors work by forcing a cell into the  $G_0$  stage of the cell cycle, a quiescent stage in which the cell is no longer in the cell division cycle, yet is still able to enter the cycle at a later time point. The alternative is to induce cells into a state where they can no longer enter the cell division cycle. This negative regulation can be brought about by tumour suppressor genes which limit cell growth and proliferation. The evidence of these signals can be seen in tissue culture, where normal cells will proliferate to yield a single layer of cells only, and further growth is suppressed through a variety of mechanisms. Cancer cells will however continue to propagate and pile up in order to form clumps. Cancer cells thus need to evade the growth suppressor signals in order to thrive.

#### *3.1.5.3 Avoiding immune destruction*

The role that the immune system plays in fighting cancer, both in cancer formation and progression, is not well understood. Theory suggests that the immune system is constantly alert and as soon as a new tumour is detected it is destroyed. Tumours therefore need the ability to avoid destruction by the immune system. One possibility here is that cancer cells may use immune-suppressive factors to avoid the immune system.

#### *3.1.5.4 Enabling replicative immortality*

Normal cells in the body are only able to go through a limited number of consecutive cell growth and division cycles. The limit is provided by senescence, i.e. when a cell enters into a non-replicative state, and apoptosis. The replication limit is provided by telomeres at the end of each chromosome which shorten with each cell division until the minimum length is achieved. Variants of cells which are able to multiply without limit are defined as immortal cells. Cancer cells acquire this unlimited replicative potential by expressing telomerase. This extends telomeric DNA such that it is able to counter the telomere erosion which would otherwise occur, avoiding the triggering of senescence and apoptosis – both mechanisms which act as an anticancer defence.

#### *3.1.5.5 Tumour-promoting inflammation*

Almost all tumours will contain some immune system cells. The immune system response has been seen to be an attempt to destroy the tumour. However, the inflammatory response of the immune system appears to aid the tumour by supplying biological molecules which may sustain proliferation, resist cell death, encourage angiogenesis as well as facilitate invasion and metastasis. Thus the inflammation caused by the immune system may be considered as a characteristic which enables the tumourigenic process.

#### *3.1.5.6 Activating invasion and metastasis*

Tumours can invade other tissues through local invasion or metastatic spread. In local invasion, a tumour may invade the tissue surrounding it. In metastatic spread, the tumour spreads to tissues which are farther away from the original tumour. This section focuses on invasion through metastatic spread.

Tissue invasion is the ability of a tumour to move to a different site and the tumour which forms in this new location is called metastatic tumour, a major cause of cancer-related deaths in humans. In these new areas, cancer cells have access to more nutrients and space. The process of cancer metastasis is termed the invasion-metastatic cascade. After a cancer cell is transformed and grows into a local tumour, angiogenesis is induced. Cancer cells may detach from the rest of the tumour and

enter the blood and lymphatic vessels by motility and a process termed as intravasation. Once in the vessels, embolization occurs such that the vessel is obstructed and these emboli are carried within the vascular system to a capillary bed. Here extravasation occurs such that the tumour emboli exit the blood and lymphatic vessels and reach an organ parenchyma, where they are able to grow similarly to the primary tumour but with the adaptations required according to the microenvironment of the host tissue.<sup>41</sup> The process by which the growth of the micro-metastatic lesion grows into a macroscopic tumour is termed colonization and requires the metastatic tumour to establish a microenvironment in which it can survive. The process of invasion and metastasis is thus likely to involve a number of complex cell-biological programs. That said, the dissemination of metastasis is considered to be the final step of primary tumour progression and carries much lower survival rates.

#### *3.1.5.7 Inducing angiogenesis*

All tissue in the body needs access to nutrients and oxygen, and must be able to remove any metabolic waste and carbon dioxide. This is generally done through blood. In tumours, new blood vessels are created through a process called angiogenesis. While in normal tissue angiogenesis occurs only for short periods of time, in tumours angiogenesis is almost always activated. It is governed by both angiogenic regulators which may either induce or inhibit angiogenesis. Whereas in normal tissue vasculature is organised, in tumour tissue it tends to be random and chaotic, and is characterised by increased leakiness and an abnormal level of endothelial cell proliferation and apoptosis. The way tumours induce neovascularisation varies and the expression of angiogenic regulators may be upregulated by oncogenes present in the cancer cell. One such angiogenic regulator is the vascular endothelial growth factor (VEGF) and anti-VEGF antibodies are one of the therapeutic mechanisms used in order to impair neovascularization.

#### *3.1.5.8 Genome instability and mutation*

Genome mutation and instability provides a basis for cancer cells to prosper. Gene mutations may provide advantages to specific cells such that tumours may outgrow the local tissue micro-environment. Cancer can be seen as a multi-step process of

genetic mutations<sup>42</sup>. Cancer cells thus have an increased sensitivity to mutagenic agents and are also able to debilitate the defence mechanism of cells which aim to either resolve DNA mutations or force mutant cells to go into senescence or apoptosis. Genome instability is able to hasten the speed by which cancer cells obtain advantageous mutations and hence is instrumental in enabling tumour progression.

#### *3.1.5.9 Resisting cell death*

For a tumour to expand it needs to both proliferate and resist cell death. Apoptosis may occur as a way of destroying cells which would have replicated incorrectly, thus helping to prevent cancer development. Cancer cells may however develop a resistance to apoptotic pathways. This can be done in a variety of ways and is most commonly done through the loss of the TP53 tumour suppressor gene, which acts as a sensor for DNA damage. Cell death may also be resisted by increasing the expression of anti-apoptotic regulators or by decreasing the expression of pro-apoptotic regulators.

While apoptosis is a programmed cell death, cancer cells may also be at risk of dying due to resource starvation. The increased proliferation of cancer cells implies that in certain areas of a tumour, cells may experience nutrient starvation such as a lack of glucose and oxygen. In these cases, cancer cells may use autophagy, a process by which cells will break down less important organelles to produce the required energy so as to survive. Autophagy is also a process which is regulated by the cells. Cancer cells which undergo this process may enter a state of reversible dormancy, which may result in tumour regrowth following treatment. Thus while autophagy limits the cell's replicative capabilities, it may contribute to tumour progression.

Cells may also die through a necrotic process which represents a form of traumatic cell death. Through necrosis cells become bloated and explode, resulting in the contents of the cell becoming part of the tissue micro-environment. Necrosis may also be controlled through a genetic process, and it has been suggested that necrotic cells could recruit inflammatory cells which are responsible for removing the necrotic debris. These same cells may however stimulate growth by enabling angiogenesis and

further proliferation of cancer cells. Necrosis may thus also contribute to tumour progression.

#### 3.1.5.10 *Deregulating cellular energetics*

Apart from being able to proliferate, cancer cells need to make adjustments to the energy metabolism of the cell in order to promote cell growth and division. Cells can produce energy in one of two ways, either by using aerobic respiration (with oxygen) or by using anaerobic respiration (without oxygen). In aerobic respiration, glucose is converted to pyruvate via glycolysis in the cytosol of the cell, and pyruvate is then transported to the mitochondria in the cell to be further broken down into carbon dioxide and water through oxidisation. In anaerobic respiration glycolysis still occurs, however pyruvate is not oxidised, and thus much less energy is produced. Cancer cells, which often suffer from hypoxic conditions, appear to be able to regulate the metabolism of glucose to use only glycolysis, even in the presence of oxygen. In order to produce more energy some cancer cells will regulate the glucose transport so as to bring more glucose into the cytoplasm. The reprogramming of the cellular energy metabolism may thus be an important factor to consider in understanding how tumours progress and how they react to treatment.

#### 3.1.6 HISTOPATHOLOGY AND GRADING

A number of features define the histopathological features of cancer. First, the morphology, or shape, of cancer cells is different from that of normal cells. Second, the architecture of a tumour is less organised than the parent tissue, as can be seen in the vascular network which tends to be more chaotic and leaky. Third, cancer cells may have an increased nucleus to cytoplasm ratio and some cells may be multi-nucleated. That said, cancers can be heterogeneous and different cells can vary in size.<sup>43</sup>

Histopathologically it is important to be able to differentiate between benign and malignant tumours. Benign tumours grow slowly in a confined space within a tissue and do not invade or metastasize. Malignant tumours, on the other hand, grow more rapidly and appear to be invasive and may also metastasize.

One of the important tumour classifications carried out histopathologically, is tumour grading. Tumour tissue is analysed in order to determine whether it is similar to the tissue of origin, and if it is similar it is defined as well differentiated. Tumour tissue which does not have the features of the tissue of origin and shows aggressive growth and high mitosis is defined as poorly differentiated. While grading can differ from one cancer type to another, a basic grading system will define a well differentiated tumour as grade 1 and is considered a low grade tumour, a moderately differentiated tumour is defined as grade 2, a poorly differentiated tumour is defined as grade 3 and an undifferentiated tumour is defined as grade 4 and is considered a high grade tumour. Tumour grading carries prognostic significance and it is expected that patients with higher grade tumours will have a lower survival rate than those with low grade tumours.

Histopathological reports include, where possible, the tumour size, grade, architecture, rate of mitosis, margin involvement and invasion of the vascular network. While histopathological analysis is important in identifying tumour severity, other factors need to be taken into consideration when staging a tumour. In particular, the size of the primary tumour, the presence of nearby lymph nodes and the presence of distant metastases need to be considered through clinical examinations and radiological analysis. Finally, in addition to the above, the location of the tumour carries a large significance in the prognosis of a tumour.

As this thesis focuses on paediatric brain tumours, a basic anatomy of the brain is presented prior to describing childhood brain tumours in more detail.

## 3.2 The Brain

### 3.2.1 BACKGROUND

The brain and the spinal cord form the central nervous system (CNS), which, together with the peripheral nervous system detects changes in the internal and external environments and brings about the required responses from muscles, organs and glands.<sup>44</sup>

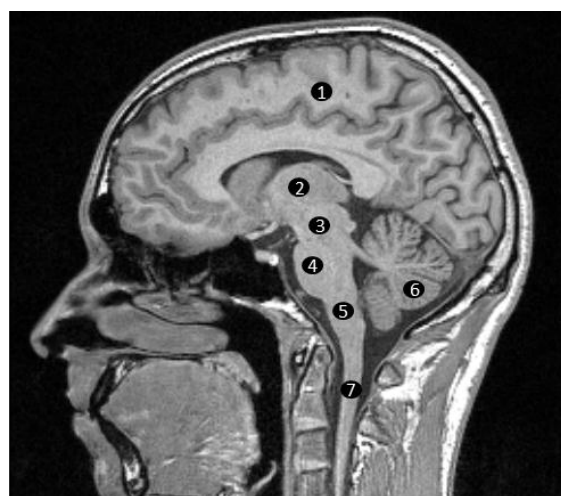
### 3.2.2 CELL TYPES

The nervous system consists mainly of nerve cells, or neurones, and neuroglial cells, or glia. Neurones need to be able to gather information from sensory receptors or organs and transmit these to other neurones or organs. Generally, neurones consist of the cell body, dendrites and axons. Dendrites emerge from the cell body and are able to receive information. The cell is then able to code the information in terms of electrical energy and transmit it via axons.

Glia outnumber neurones and their role is to ensure that neurones function normally. The main types of glial cells are the oligodendrocytes, which are responsible for forming myelin sheath around nerve cell axons, forming an insulating cover and increasing the efficiency of electrical energy transmission; the astrocytes, which are thought to support the formation of the blood-brain barrier; and the microglia, which act as part of the immune defence system in the CNS.

The CNS is a heterogeneous structure, with areas most abundant in neuronal cell bodies known as grey matter, and areas most abundant in myelinated axons known as white matter.

### 3.2.3 ANATOMY



- 1 – cerebrum
  - 2 – diencephalon
  - 3 – midbrain
  - 4 – pons
  - 5 – medulla
  - 6 – cerebellum
  - 7 – spinal cord
- } brain stem

**Figure 3.4: Anatomy of the brain.** The brain can be divided into four main regions: the *cerebral hemispheres* (1), the *diencephalon* (2), the *brain stem* comprising the *midbrain* (3), *pons* (4) and *medulla* (5), and the *cerebellum* (6). The brain, together with the *spinal cord* (7) make up the CNS.

The brain can be broadly divided into four sections – the cerebral hemispheres (left and right), the diencephalon, the cerebellum and the brain stem, as shown in Figure 3.4. The two cerebral hemispheres are not completely separated and are linked to each other through the corpus callosum. In addition, the brain includes the ventricular system.

The cerebral hemispheres are the largest sections of the brain and consist of an outer layer of grey matter, described as the cortex, and an inner area of white matter. Their function lies in conscious awareness, thought, memory and intellect. All sensory modalities and motor functions are represented consciously in the cerebral cortex. The cerebrum is divided into four lobes: the frontal lobe containing the primary motor cortex which controls movement; the parietal lobe containing the primary somatosensory cortex which controls touch, pressure, pain and temperature; the occipital lobe containing the visual cortex; and the temporal lobe containing the auditory cortex. The effect of lesions in the four lobes is dependent on the location in which they occur and may differ from person to person, as different areas may be used for a similar function. For example, language is normally dominant on the left side of the brain but this is not universal to everyone and thus lesions on the right side may also cause speech deficits. The left and right side of the brain connect through the corpus callosum and lesions in these areas may effect communication between two sides of the brain. Another important structure, lying deep within the subcortical white matter is the basal ganglia which functions to facilitate useful and purposeful movements, and inhibit unwanted movements. Lesions in this region thus lead to a loss of control of voluntary movement.

The diencephalon includes the thalamic regions: the epithalamus includes the pineal gland; the thalamus has an important role in sensory, motor and cognitive functions; the subthalamus is related to the basal ganglia in function; and the hypothalamus is involved in the autonomic nervous system, the limbic system and the neuroendocrine system. A lesion in the thalamus leads to a loss of sensation in the face and limbs contralaterally – on the opposite side of the body as to where the lesion is.

---

The brain stem, comprising of the midbrain, pons and medulla, constitutes a small part of the brain but provides a vital function as it links the brain to the spinal cord, and also controls some vital functions such as respiration and the cardiovascular system. A lesion in the brain stem will cause cranial nerve dysfunction and incoordination ipsilaterally – on the same side of the body; and hemiparesis (weakness on one side of the body), hyperreflexia (an over-reactive reflex system) and hemisensory loss (loss of sensation on one side of the body) contralaterally.

The cerebellum is linked to the medulla, pons and midbrain through nerve fibres. The outer part of the cerebellum consists of grey matter, which surrounds a white matter core. The main role of the cerebellum lies in the coordination of movement and operates at an unconscious level. The symptoms of a lesion in the cerebellum differ by the region in which the lesion is present. In the midline a lesion results in loss of postural control and thus an inability to sit or stand. Unilateral lesions cause symptoms ipsilaterally such that a lesion on the right of the cerebellum causes incoordination in the right arm and right leg. Eye coordination is also effected by lesions to the cerebellum.



**Figure 3.5: The ventricular system.** The ventricular system consists of a series of connecting chambers filled with CSF. The *lateral ventricles* (1) are located on either side of the cerebral hemispheres. They are then linked to the *third ventricle* (2) which continues to become the *cerebral aqueduct* (3). The cerebral aqueduct extends through the midbrain to link the third and the *fourth ventricle* (4). The fourth ventricle is located between the brain stem and the cerebellum.

The ventricular system includes the lateral ventricles, the third ventricle, the cerebral aqueduct and the fourth ventricle as shown in Figure 3.5. The ventricular system is filled by CSF which is produced by the choroid plexus, located in the lateral, third and fourth ventricles. The CSF acts so as to protect the brain from damage, remove waste products and provide some of the nutrients required. If the flow of CSF is obstructed, such as in the case of a brain tumour, an increase in fluid pressure occurs causing the ventricles to swell up. This is known as hydrocephalus and the main symptoms include headaches and unsteadiness. Hydrocephalus occurs when the rate of CSF production is higher than that of CSF absorption. Clinically, a shunt may be inserted in order to drain the excess CSF into another area of the body, normally the abdomen, and to the venous system through which it would have been absorbed under normal conditions.

### 3.3 Paediatric Brain Tumours

#### 3.3.1 BACKGROUND

Childhood cancer is the leading cause of disease related deaths in children aged 1-14.<sup>45</sup> Brain tumours are the second most common cancer in children, with leukaemia being the most common. Although brain tumours only account for between 20 and 25% of all cases, they are the main cause of cancer related deaths in children.<sup>36</sup> Besides the higher mortality, due consideration needs to be given to the toxicity of treatment of brain tumours, with the aim in particular being to reduce late effects and diminish treatment side-effects.

#### 3.3.2 COMPARISON TO ADULT BRAIN TUMOURS

When comparing adult tumours to those in childhood, it can be observed that childhood cancer is closely linked to tissue development, while in adults it is related to the interaction of cells with environmental carcinogens. In children, the primary event to initiate the tumour may occur during the development of the embryo, as in the case of embryonal tumours such as medulloblastoma.<sup>36</sup>

The most common primary brain tumours in children are low grade gliomas and medulloblastoma, while the most common primary brain tumours in adults are

glioblastoma and meningioma<sup>46</sup>. Apart from tumour type, tumour location also varies between adults and children, with a much lower percentage of adults presenting with brain tumours involving the cerebellum than children. Children are also more sensitive to radiotherapy and chemotherapy and thus treatment has more potential side effects.<sup>47</sup>

Unlike in the case of children, where most brain tumours are primary tumours, those in adults are tumours which would have metastasised from other parts of the body, such as lung cancer, breast cancer, melanoma and kidney cancer.<sup>48</sup> Hence the biology of these tumours varies significantly from those in children. Only 2% of cancers are primary brain tumours in adults, compared to the 20-25% in children, and the vast majority of these are gliomas.<sup>49</sup> Due to the differences in biology, location and sensitivity to treatment, childhood tumours need to be considered in a different light to adult tumours, and the rest of this chapter focuses on paediatric brain tumours.

### **3.3.3 CLINICAL PRESENTATION**

The median symptom to diagnosis time interval varies by country – between 5 and 14 weeks.<sup>36</sup> Longer time intervals are generally related to slow growing tumours with vague symptoms. Brain tumour symptoms are non-specific and neuroimaging is required to confirm diagnosis. Clinical presentation may show signs of increased intracranial pressure. Symptoms vary widely and include headaches, nausea, vomiting, visual disturbance, behavioural issues and epilepsy, and are dependent on the site and type of the tumour.

### **3.3.4 TUMOUR CLASSIFICATION**

Tumours are defined according to the location and cell type from which they are derived and the ICD-O classification for CNS tumours<sup>36</sup> is shown in Table 3.1. A brief description of some of the tumour types is given in this section.

**Table 3.1: Central nervous system tumour classification (ICD-O 9380–9539)**

Neuroepithelial (brain tumours, spinal tumours)	Glioma	Astrocyte	Astrocytoma (Pilocytic astrocytoma, Pleomorphic xanthoastrocytoma, Fibrillary (also diffuse or low grade) astrocytoma, Anaplastic astrocytoma, Glioblastoma multiforme)
		Oligodendrocyte	Oligodendrogloma
		Ependyma	Ependymoma Subependymoma
		Choroid plexus	Choroid plexus tumour (Choroid plexus papilloma, Choroid plexus carcinoma)
	Multiple/ unknown		Diffuse intrinsic pontine glioma
			Oligoastrocytoma
			Gliomatosis cerebri Gliosarcoma
	Mature neuron		Ganglioneuroma: Ganglioglioma, Retinoblastoma, Neurocytoma, Dysembryoplastic neuroepithelial tumour, Lhermitte-Duclos disease
	PNET		Neuroblastoma (Esthesioneuroblastoma, Ganglioneuroblastoma), Medulloblastoma, Atypical teratoid/rhabdoid tumour
	Primitive		Medulloepithelioma
Meningiomas (meninges)	Meningioma	Meningioma	
Hematopoietic	Primary central nervous system lymphoma		

Adapted from <sup>36</sup>

### 3.3.4.1 Low-grade Gliomas

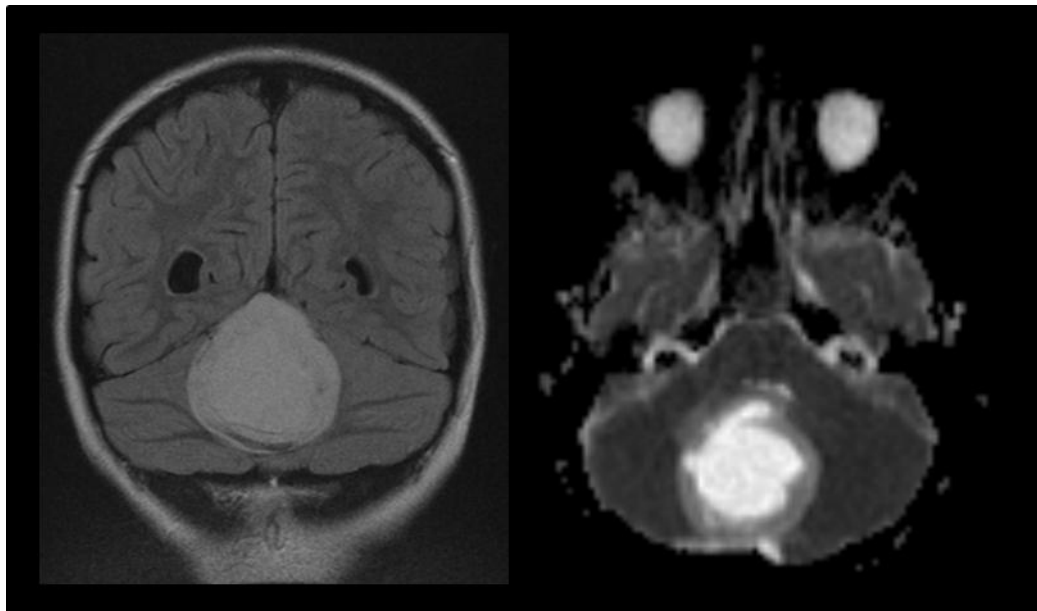


**Figure 3.6: Juvenile pilocytic astrocytoma in a 9 year old female patient.** A coronal FLAIR image (left) and an axial ADC image (right) are shown for a patient with JPA. Bright areas in ADC are representative of fluid areas and in this case gliomatous areas can be observed. These appear as cystic on the ADC image as they are more fluid than normal brain parenchyma. However, they are less fluid than areas of CSF and are not suppressed in the FLAIR image. The patient was treated via surgery, with two surgical resections taking place, followed by a watch and wait protocol. The patient was well at last follow-up, five years after diagnosis, age 14.

**Juvenile pilocytic astrocytoma:** The majority of low grade astrocytomas are pilocytic astrocytomas – also termed juvenile pilocytic astrocytomas (JPA) due to their prevalence in children and adolescents. These tumours occur mostly in the cerebellum, are well circumscribed, have a low cellularity and do not infiltrate the surrounding brain. Many JPAs are associated with neurofibromatosis type 1 (NF1) – a gene responsible for activating the protein neurofibromin. Mutations to this gene can arise sporadically or can be passed on through germline transmission of an already established mutation. On MRI, JPAs may show cystic changes and show minimal or no contrast enhancement. These tumours are best visualised on a FLAIR (fluid attenuated inversion recovery) sequence. Following treatment, serial imaging is important due to the likelihood of recurrence.

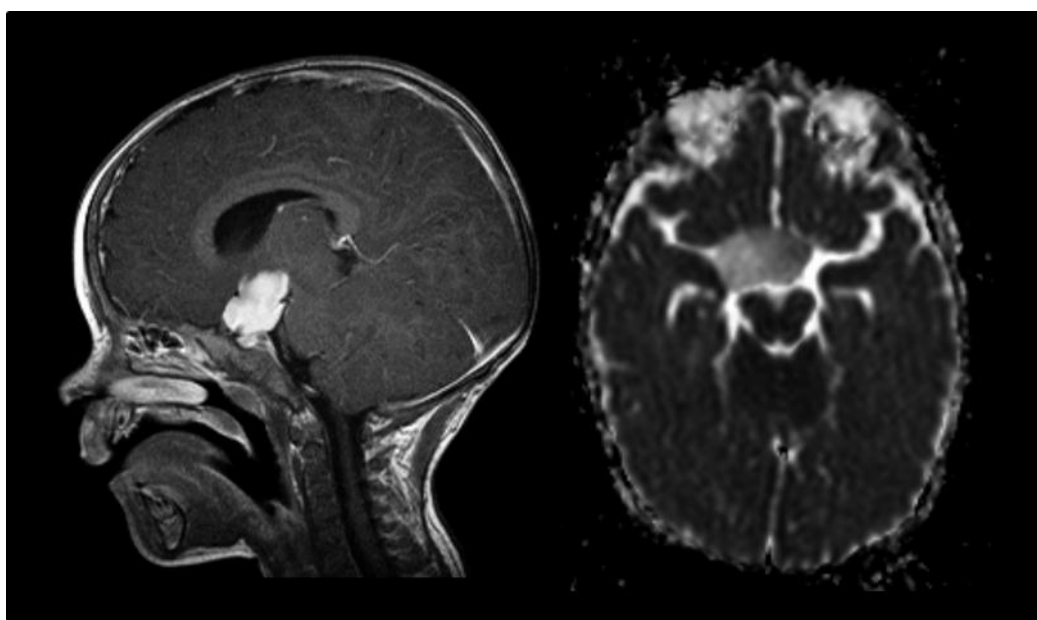


**Figure 3.7: Optic pathway glioma in a 1 year old female patient.** A sagittal post-contrast T1 weighted image (left) and an axial ADC image (right) are shown, showing the tumour in the optic chiasm. A watch and wait protocol was first employed and this was followed with chemotherapy following progression. The patient received proton therapy at age 5 and was well at last follow-up, age 6.

Optic pathway gliomas: These tumours represent 5% of paediatric CNS tumours and are a subtype of JPA which arise within the visual pathways (the optic nerve, chiasm, tract and radiation). They are also a low grade tumour. However, in contrast with JPA, they infiltrate the brain and can extend into the posterior visual cortex and other structures such as the hypothalamus. Their border is not well defined and surgery is generally avoided. Clinical presentation of optic pathway gliomas (OPG) includes a visual deficit, which may be difficult to detect, particularly in infants. Tumours which involve the hypothalamus will affect the endocrine system of the patient and may result in precocious puberty. Tumours which involve the thalamus may result in motor deficits. Biopsies are not required in these tumours where the appearance on MRI is typical, and surgery is often only carried out in more advanced stages of the tumour, where there is no vision. These tumours are generally treated via radiotherapy; however chemotherapy is used in order to delay radiotherapy in young children under the age of three. Although the overall survival of OPG patients is high, these children tend to suffer from considerable visual deficits.

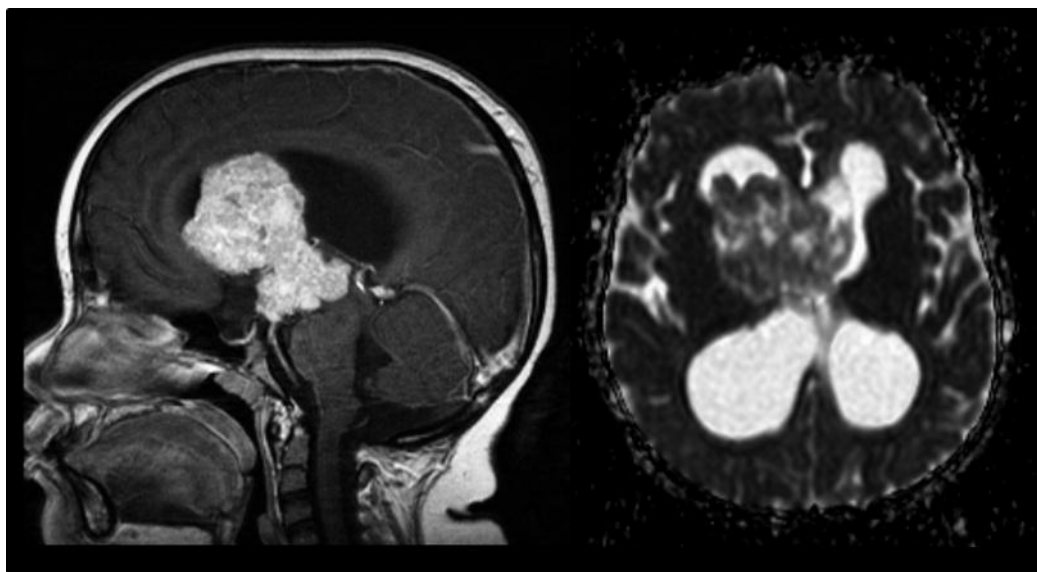


**Figure 3.8: Subependymal giant cell astrocytoma in an 11 year old male patient.** A sagittal post-contrast T1-weighted image (left) and an axial ADC image (right) are shown. Ventricular enlargement can also be observed in the images. Surgery was attempted but failed due to haemorrhage. The patient was treated via chemotherapy, reducing the size of the tumour and allowing for complete surgical resection. The patient was doing well at last follow-up, age 16.

**Subependymal giant cell astrocytoma:** This is a benign tumour which occurs mostly in patients with tuberous sclerosis – a rare genetic condition. Subependymal giant cell astrocytomas (SEGA) are treated via surgery. Where surgery is not possible, new chemotherapeutic techniques such as rapamycin, which is able to target the molecular pathways affected by the tuberous sclerosis gene mutation, may be employed. These agents are able to decrease the size of the tumour in order to improve the likelihood of complete surgical resection. Although classified as an astrocytoma, tumour cells tend to be of both neuronal and glial origin.

### 3.3.4.2 High-grade gliomas

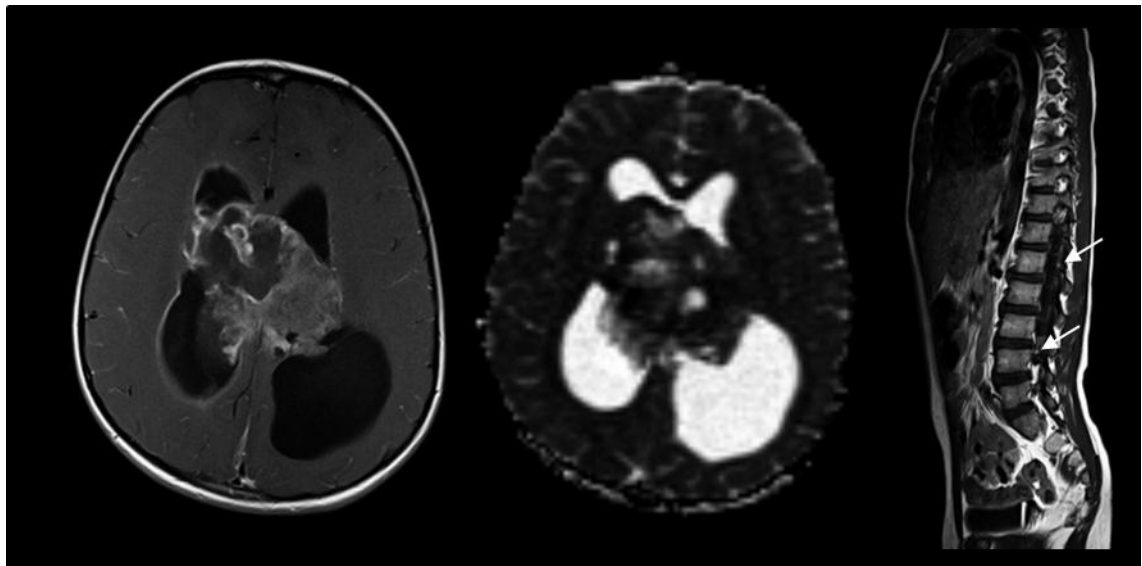


**Figure 3.9: Glioblastoma multiforme in a 7 year old male patient.** Axial post-contrast T1-weighted (left), ADC (middle) and sagittal spinal (right) images are shown. The patient had disseminated disease in the spinal cord and also hydrocephalus. The patient was treated via chemotherapy and radiotherapy, and received palliative care as the solid component and metastases grew further. The patient died 8 months after diagnosis.

Glioblastoma multiforme: High-grade astrocytomas represent between 10 and 20% of paediatric CNS tumours and occur mostly in the supratentorial region (in the cerebral regions) and in the brain stem. Mostly these tumours include anaplastic astrocytoma and glioblastoma multiforme (GBM). Both tumours are diffusely infiltrative, making it difficult for the surgeon to identify tumour borders, and show high mitotic activity. GBM tumours tend to exhibit areas of necrosis, cystic regions, haemorrhagic areas and areas of high cellularity and thus the tumour itself is heterogeneous. While the clinical symptoms of high-grade tumours varies by site, age and biological aggressiveness, the time interval between onset of symptoms and diagnosis is much shorter in high-grade tumours than in low-grade tumours. Children with high grade tumours are generally treated first by surgery, requiring an aggressive resection while aiming to preserve neural function. Radiotherapy is generally a standard mode of treatment following surgical resection together with adjuvant chemotherapy. Survival of patients with high-grade gliomas is still low, with less than 20% of patients surviving five years.

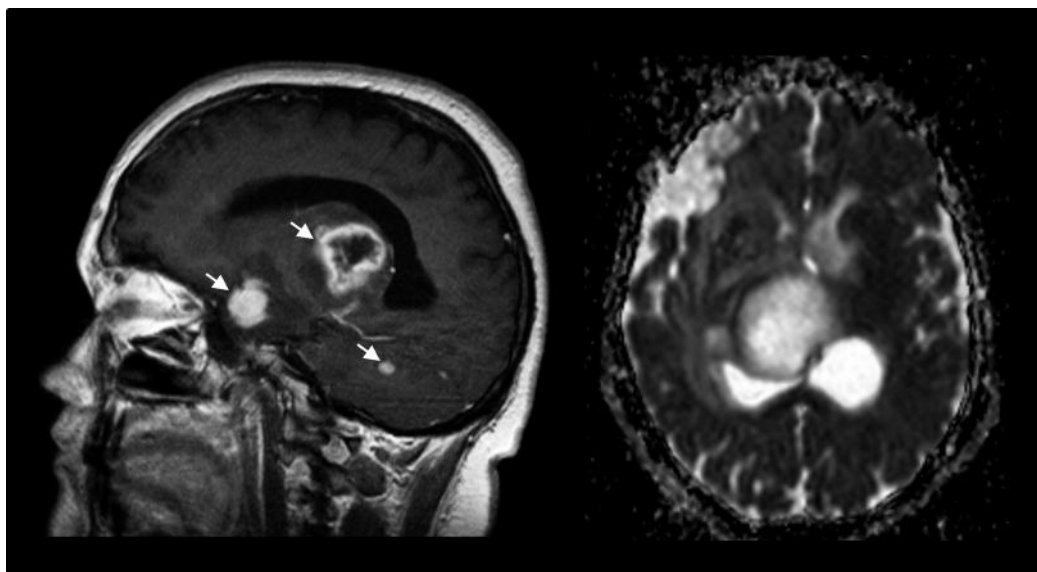


**Figure 3.10: Gliomatosis cerebri in a 17 year old male patient.** Post-contrast T1-weighted (left) and ADC (right) images show the tumour to have spread in different regions. The patient was diagnosed age 16 and following the shown imaging was given palliative care. The patient died 1 year and 2 months after diagnosis, age 17.

Gliomatosis cerebri: This rare high grade-glioma is characterised by a diffuse pattern of spreading across the brain parenchyma and defined by the World Health Organization (WHO) to involve at least 2 critical lobes, but often extending to infratentorial structures<sup>50</sup>. Histological samples are consistent with those of GBM, but total surgical resection is in this case not possible due to the diffuse nature of the tumour. Whole brain radiotherapy is thus the offered treatment, together with chemotherapy. Prognosis of patients with gliomatosis cerebri (GC) is very poor.

### 3.3.4.3 Brainstem gliomas

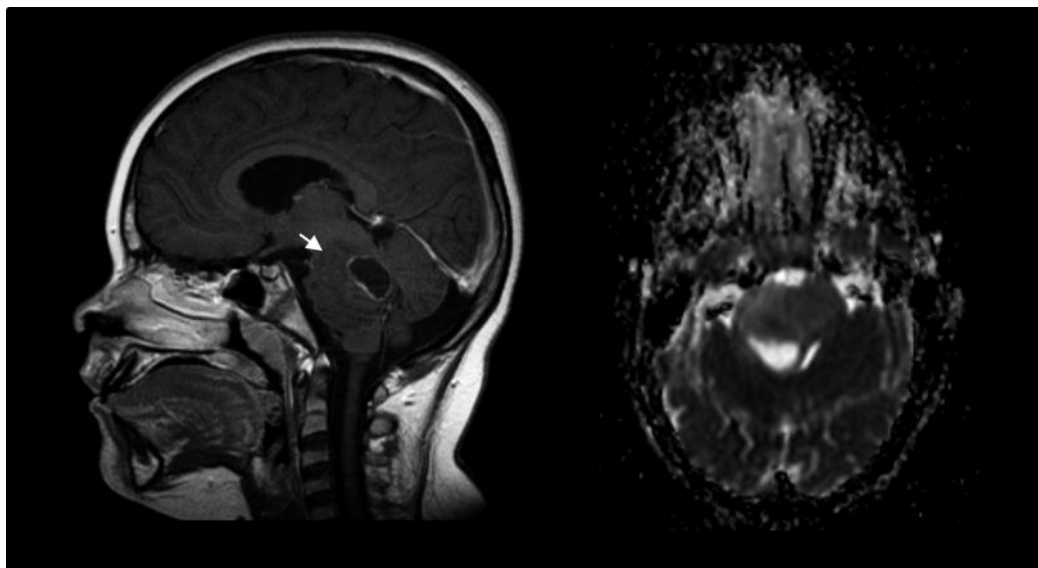


**Figure 3.11: Diffuse intrinsic pontine glioma in a 9 year old male patient.** Sagittal post contrast T1-weighted (left) and axial ADC (right) images show the tumour in the brain stem. The patient was treated with chemotherapy and radiotherapy and died 7 months after diagnosis, age 10.

**Diffuse intrinsic pontine glioma:** Brain stem gliomas constitute between 10 and 20% of paediatric CNS tumours and most tumours arise in the pons but may extend into the medulla and midbrain. The vast majority of these tumours (75-85%) are diffuse intrinsic pontine gliomas (DIPG) and carry a very poor prognosis. DIPG tumours are a heterogeneous group of tumours, mostly grade 2-3 astrocytoma, which are generally not biopsied or resected due to their location. Diagnosis is normally carried out radiologically without histological analysis to determine the exact tumour type. DIPG tumours are treated with radiotherapy and chemotherapy, however, the survival outcome is dismal, with less than 10% of children surviving more than two years after diagnosis<sup>51</sup>.

#### 3.3.4.4 Ependymoma

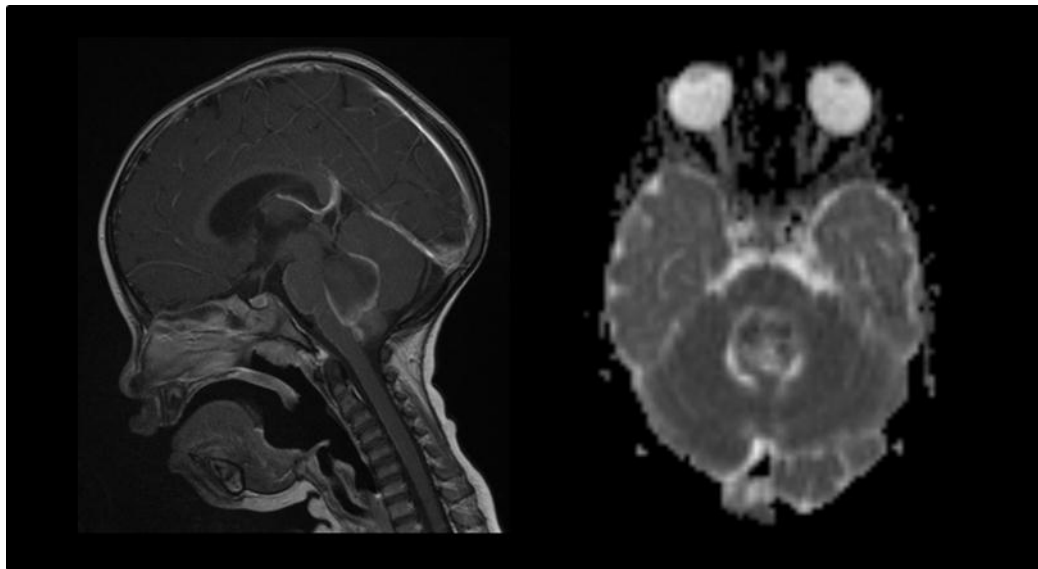


**Figure 3.12: Ependymoma in a 2 year old female patient.** Post-contrast sagittal (left) and ADC (right) images show the tumour in the posterior fossa. Surgery and chemotherapy was given, with the tumour classified as a grade 2 tumour. The patient was alive at last follow-up, 7 years after diagnosis, age 9.

Ependymomas are gliomas which arise from the ependymal cells lining the ventricular system. They constitute about 8% of all paediatric brain tumours and 25% of spinal cord tumours. In the brain, they occur mostly in the posterior fossa (infratentorial) and the most common sites are the fourth, third and lateral ventricles. Variants can be classified between grade 1 and 3. They are normally well delineated and may show areas of calcification, haemorrhage and cysts. Ependymomas are treated via surgery – aiming for gross total resection, with radiotherapy being a standard adjuvant therapy in older children and chemotherapy being used instead of radiotherapy in young children. Longer-term survival over 5 years is seen in over 50% of patients, and hence the effects of treatment need to be taken into consideration in order to reduce long-term sequelae.

#### 3.3.4.5 Choroid plexus tumours

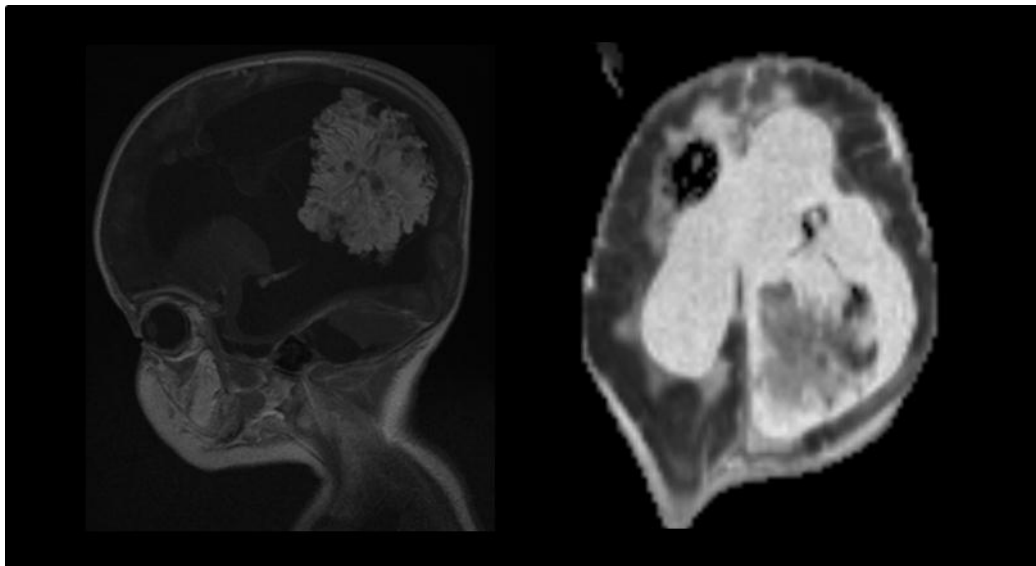


**Figure 3.13: Choroid plexus papilloma (grade 1) in a one month old male patient.** Post-contrast T1-weighted (left) and ADC (right) images show a large mass in the ventricles, causing hydrocephalus. The patient was treated via surgery and was alive at last-follow-up, 7 years after diagnosis, age 7.

Choroid plexus tumours account for between 1 and 5% of paediatric CNS tumours. The choroid plexus is responsible for producing CSF and hence these tumours tend to appear as a mass arising in the ventricles, secreting CSF and thus causing hydrocephalus. Choroid plexus tumours vary in grade between grade 1 and 3 and are removed via surgical resection, while also introducing a shunt in order to drain the ventricles and reduce the tension on the brain. Adjuvant radiotherapy and chemotherapy may also be provided depending on the age of the child and the extent of surgical resection. However, gross total resection and tumour grade are the most important prognostic factors. The long-term overall survival (>5years) is around 80% in children with choroid plexus papilloma (grade 1) and between 40 and 60% in children with choroid plexus carcinoma (grade 3).

#### 3.3.4.6 Embryonal tumours

Embryonal tumours constitute a large proportion of paediatric brain tumours. Historically they have been grouped under the term primitive neuroectodermal tumours (PNET) and were characterised by a relatively homogeneous histological

appearance which consisted of small round cells – undifferentiated neuroepithelial cells, exhibiting a high rate of mitosis. PNETs have been shown to be a heterogeneous group of tumours and embryonal tumours now include medulloblastoma, atypical teratoid/rhabdoid tumour (ATRT), supratentorial PNET (sPNET) and pineoblastoma.

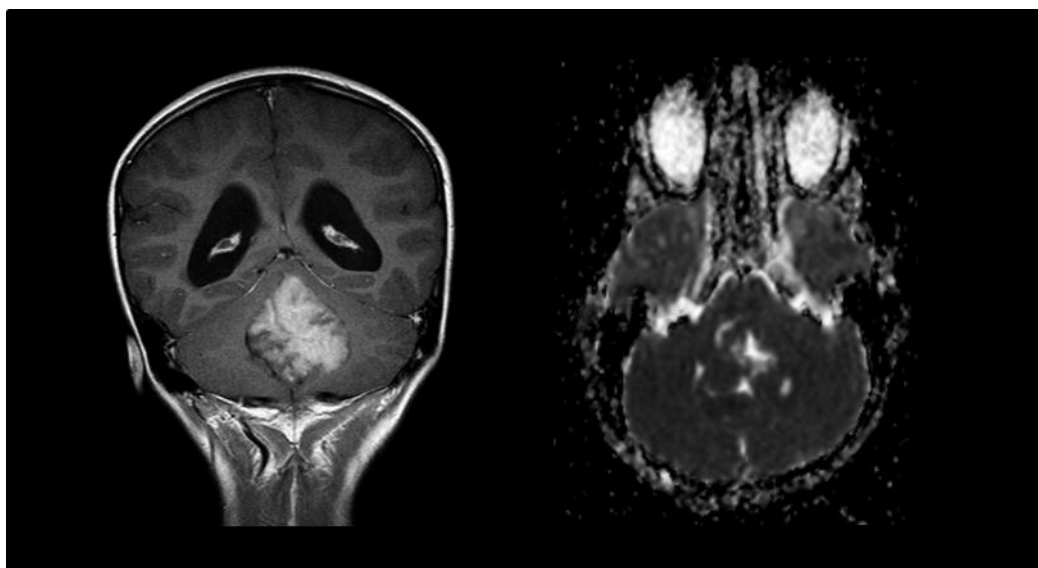


**Figure 3.14: Medulloblastoma in a 7 year old female patient.** Post-contrast T1-weighted (left) and ADC (right) images show a large mass in the cerebellum. The patient was treated with surgery, chemotherapy and radiotherapy and was doing well at last follow up, 6 years after diagnosis, age 13.

Medulloblastoma: This tumour was originally referred to as an infratentorial PNET. However, advances have shown medulloblastoma to exhibit different biology and while histopathologically it is divided into four main WHO subgroups (classical medulloblastoma, anaplastic/large cell medulloblastoma, nodular desmoplastic medulloblastoma and medulloblastoma with extensive nodularity), it can also be subdivided into four main molecular subgroups (Wnt, Sonic Hedgehog or Shh, Group 3 and Group 4)<sup>52</sup>.

Overall, medulloblastoma is the most common malignant CNS tumour and constitutes around 20% of paediatric CNS tumours. It is thus the second most common paediatric brain tumour after JPA. All medulloblastoma types are classified as grade 4; however certain subgroups have a much better prognosis. Clinically, they present most often in the midline of the cerebellum close to the fourth ventricle and symptoms may include

behavioural changes and lower school performance, followed by headaches, vomiting and other neurologic signs such as ataxia. Tumours are removed via surgery in order to try and achieve gross total resection. Following resection, staging needs to be conducted in order to determine whether the tumour has disseminated. Prognosis is better in patients where there is no evidence of metastases, having had gross total resection, and who are over three years of age. Children less than three are unlikely to receive radiotherapy treatment and proceed with only adjuvant chemotherapy. When considering the molecular subgroups, those in the Wnt group have survival rates over 90%<sup>52</sup>. Considering all subtypes, the overall 5 year survival stands at 60%.

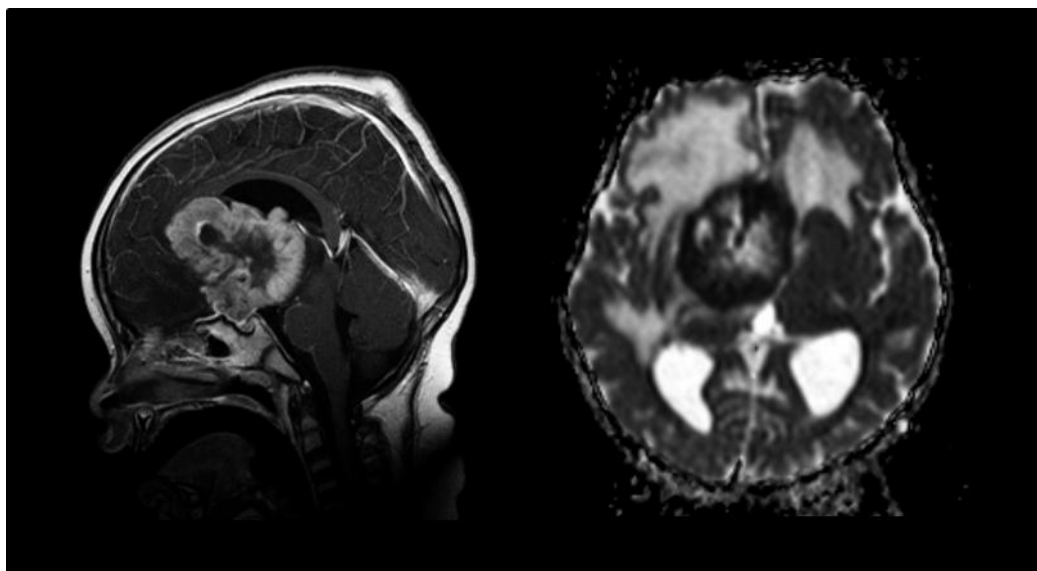


**Figure 3.15: Atypical teratoid/rhabdoid tumour in a 2 year old male patient.** Post-contrast T1 weighted (left) and ADC (right) images show a supratentorial tumour growing from the third ventricle. The ADC image also shows large areas of oedema surrounding the tumour. The patient was treated via surgery and chemotherapy and died 3 months after diagnosis, age 2.

Atypical teratoid/rhabdoid tumour: ATRT is a rare tumour which constitutes between 1 and 2% of paediatric CNS tumours and is more frequent in infants. It is a malignant grade 4 tumour and the majority occur in the posterior fossa. On MRI, ATRT has similar appearance to medulloblastoma and molecular diagnosis is required in order to determine whether a tumour is ATRT. Although these patients receive surgery and chemotherapy, prognosis is extremely poor, with the median survival being less than 10 months and the majority of children dying within a year. Radiotherapy is only given

to children who are old enough to tolerate its effects, and hence older children have a better long-term survival.

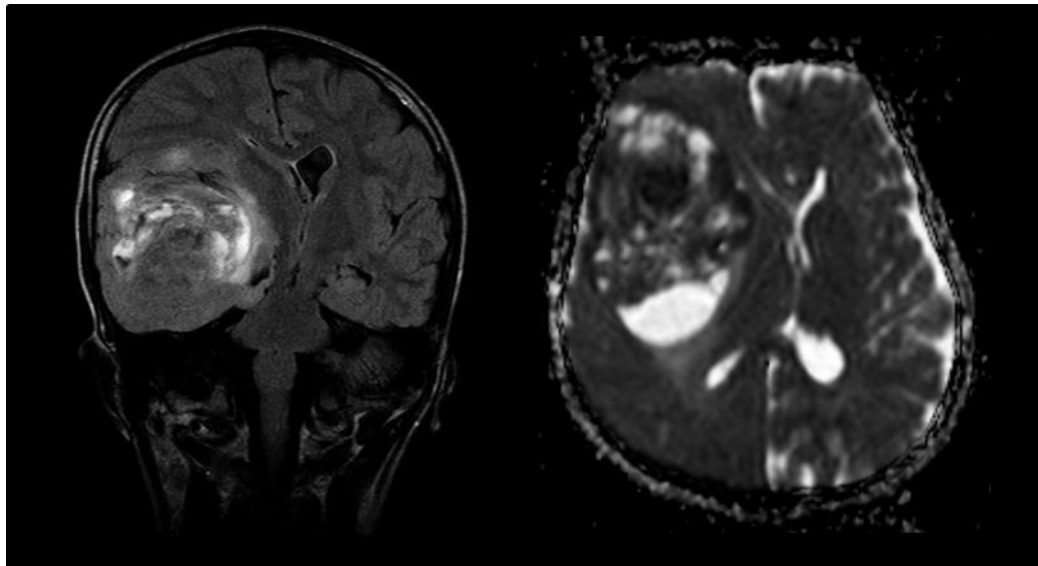


**Figure 3.16: Supratentorial primitive neuroectodermal tumour in a 9 year old male patient.** T2-FLAIR (left) and ADC (right) images show a supratentorial mass in the right temporal lobe. The patient was treated via surgery, chemotherapy and radiotherapy and died 1 year after diagnosis, age 10.

Supratentorial primitive neuroectodermal tumour: sPNET tumours are located in the cerebrum and occur in around 2.5% of paediatric CNS tumours<sup>53</sup>. While sPNET tumours tend to share many similar features to medulloblastoma, they tend to have a much worse prognosis with a 3-year survival of 33%<sup>54</sup>.

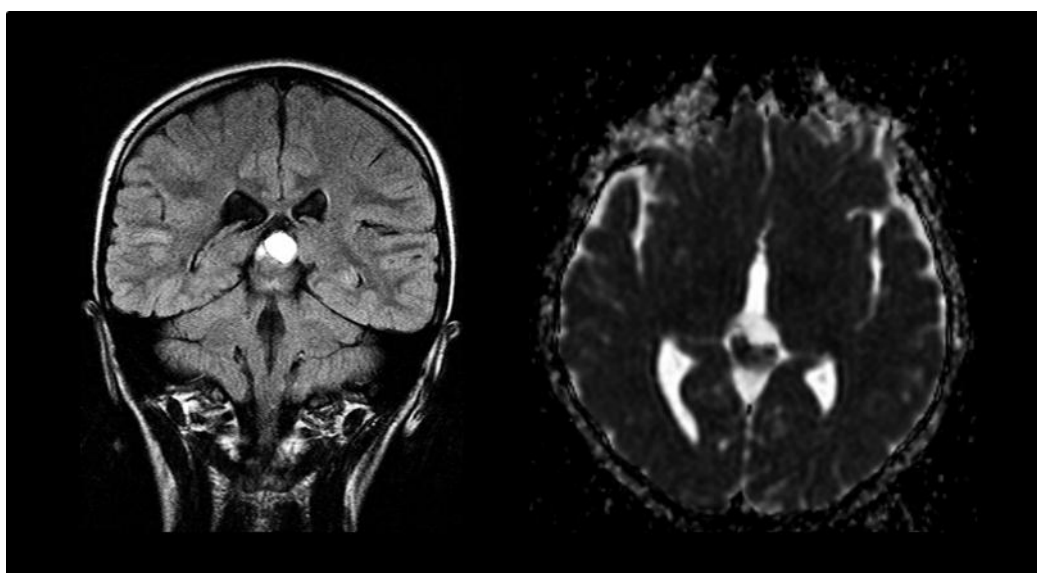


**Figure 3.17: Pineoblastoma in a 10 year old male patient.** T2-FLAIR (left) and ADC (right) images show a mass in the pineal gland. The patient was treated with surgery, radiotherapy and chemotherapy and was doing well at last follow-up, 3.5 years after diagnosis, age 14.

Pineoblastoma: Tumours occurring around the pineal gland are rare and account for less than 3% of paediatric CNS tumours with pineoblastoma accounting for half of these tumours<sup>55</sup>. Pineoblastoma resembles medulloblastoma, is also classified as grade 4 and can also metastasize. Children with pineoblastoma have a better survival than those with sPNET.

### 3.3.5 A NOTE ABOUT OEDEMA AND NECROSIS

Oedema is a common feature amongst many brain tumours. The term itself means swelling and this swelling may cause increased intracranial pressure. Oedema is currently classified into cytotoxic and vasogenic<sup>56</sup>. Cytotoxic oedema results as cells swell up and can occur in both grey and white matter. It therefore occurs on an intracellular level and leads to a slight decrease in extracellular fluid volume. Vasogenic oedema, on the other hand, results when the blood brain barrier becomes more permeable, allowing an extra net fluid flow into the extracellular space<sup>57</sup>. It therefore represents an increase in extracellular fluid volume, and can be found in areas of white matter. Brain tumour oedema is a result of more fluid moving into the brain than out of the brain and is likely to be vasogenic oedema<sup>56</sup>.

Necrosis is another common feature amongst brain tumours. It may occur as a result of hypoxia or ischaemia which comes about as the tumour outgrows its blood supply, resulting in a lack of oxygen and nutrients to cells. Apart from stress-induced necrosis, areas of necrosis may occur as a result of treatment, with chemotherapy targeting specific pathways inducing necrosis<sup>58</sup>. Of important note, radiotherapy may also induce necrosis and this radiation necrosis can sometimes act as a confound in imaging techniques as it may be difficult to differentiate between radiation necrosis, tumour recurrence and what is known as pseudoprogression – a possibly cytotoxic reaction to chemo or radiotherapy treatment which is associated with inflammation and oedema<sup>59</sup>.

### **3.3.6 TREATMENT**

Treatment strategies generally involve a combination of radiotherapy, chemotherapy and surgery. Proton therapy is also considered in certain patients meeting the required criteria. As such treatment can be with curative intent or as a form of palliative care and the type of treatment given is thus dependent on the patient and disease stage.

#### *3.3.6.1 Radiotherapy*

Radiotherapy is used either as a curative method or as part of adjuvant treatment following surgery. An understanding of how radiotherapy works needs to start with an understanding of radiation biology. Radiation biology studies the effect of primarily ionising radiation on biological systems. Ionising radiation has enough energy such that when it interacts with an atom it forces the atom to become ionised by removing at least one electron.<sup>60</sup>

Ionising radiation is reported in terms of the absorbed dose with the standard unit being the gray (Gy) and defined as  $1Jkg^{-1}$ . It is able to produce damage to DNA and is most significant when damage causes breaks in both strands of the DNA and at multiple-points, making it difficult for the cell to repair. Ionising radiation forces cells to die through the loss of mitotic reproductive integrity or apoptotic pathways. The key features which affect a cell's response to ionising radiation are radio-sensitivity, repair, redistribution, repopulation and reoxygenation.

Radio-sensitivity describes a tumour's sensitivity to radiation therapy and thus determines the dose required to achieve control of the tumour. Different tumours will have a different radio-sensitivity, with tumours such as glioblastoma multiforme unlikely to be controlled with reasonable doses. Repair refers to the ability of the tissue to repair the damage incurred following the radiation dose given. Redistribution refers to the cells' stage in the cell cycle at the time of radiation. As cells in the S-stage are most resistant to radiation and those in the  $G_2/M$  stage are the most sensitive, those in the latter stage are more likely to be killed. However the cells' stages will redistribute in between radiation doses such that the radio-sensitivity of the cell population does not change with time. Repopulation refers to the tumour's ability to proliferate and repopulate following radiotherapy. Finally, reoxygenation refers to the fact that the oxygenation status has a great effect on the radio-sensitivity of a tumour, with hypoxic regions being able to resist radiation damage much more effectively than oxygenated regions.

The radiation dose given to a tumour is dependent on the location and the surrounding tissue's radio-sensitivity. Different methods are employed in order to limit the damage done to healthy tissue while effectively treating the tumour. Fractionated radiotherapy involves spreading the dose given to a patient over a period of time in order to allow normal tissue to repair itself in between treatment fractions, and to allow for tumour cells which were hypoxic to reoxygenate, as well as for the cells to redistribute. Generally radiation is thus delivered once a day, five days a week for a number of weeks. Intensity modulated radiotherapy seeks to limit the dose to neighbouring healthy tissue. Limiting radiation damage to healthy tissue is important to reduce late effects associated with radiotherapy. In particular, younger children have a higher toxicity towards radiotherapy and it is not recommended in children under the age of three.

### *3.3.6.2 Proton therapy*

Proton therapy is a form of radiotherapy which uses protons rather than photons. Protons have the advantage of being able to travel a finite distance and then deposit the majority of their energy at the end of the path. Therefore proton therapy is able to

direct most energy to the tumour while only delivering a moderate dose to the tissue in the path of the beam. Higher doses can thus be delivered to tumours in close proximity of radio-sensitive areas such as the brain stem. The main issue with proton therapy is the cost, which is much higher than for conventional radiotherapy, even more so due to the unavailability of facilities within the UK.

### 3.3.6.3 *Chemotherapy*

Chemotherapeutic agents work by targeting one of the hallmarks of cancer described in section 3.1.5. They can either interfere directly with the DNA replication and cell-cycle, target specific intracellular biochemical pathways, or they can also work by targeting the requirements of a tumour such as anti-angiogenic agents which work by stopping the formation of new blood vessels.

Drugs and their dose need to be chosen such that the anti-tumour effect is obtained with the minimum acceptable level of toxicity and is dependent on the tumour type. When administering chemotherapeutic drugs, the dose is measured taking into consideration the absorption, distribution, metabolism and elimination from the body of the specific drug. In principle, in order to be effective, chemotherapeutic agents for treating brain tumours need to be able to cross the blood-brain barrier. However, it can be observed that in some cases the blood brain barrier is disrupted around the tumour and thus the concentration of the drug may be seen to be higher in the tumour region than in the rest of the brain<sup>54</sup>.

Chemotherapy in children has been shown to be successful when used in an adjuvant setting so as to control microscopic disease following surgery and/or radiotherapy. In these cases the aim is to reduce the risk of tumour recurrence. In other settings chemotherapy can be used as a neoadjuvant treatment, that is, it is administered prior to treatment via surgery. In this case the goal is to reduce the size of a tumour so as to make it operable or increase the likelihood of total resection. Chemotherapy can also be used in children under the age of three, and who do not tolerate radiotherapy treatment well in order to delay such treatment.

As such, chemotherapy is part of the standard care paediatric brain tumour patients receive. However, it is not selective to cancer cells and thus carries a degree of toxicity and its effects, both short and long-term, need to be assessed.

#### *3.3.6.4 Surgery*

The extent of surgical resection is one of the most important predictors of survival in paediatric brain tumours.<sup>54</sup> While this would call for an aggressive procedure, the extent of resection possible is dependent on the proximity of the tumour to important functional areas – such as areas of eloquent cortex that include motor and language pathways, the location of the tumour itself – particularly when the tumour involves the brain stem, and the presence of metastases at presentation.

Improving surgery outcomes is possible by providing useful imaging methods. Neuro-navigation can be provided by MRI which aids in planning the safest surgical route, avoiding important neural and vascular structures. Functional MRI (fMRI) and DTI can be used in order to build images of important areas and white matter pathways to be avoided so as to limit neurological deficits. Another imaging method which is employed in some centres is intra-operative MRI which allows for updated images throughout the surgical procedure and improves the extent of surgical resection. PET is another imaging method which can be used in operating brain tumours as a means of identifying eloquent cortex and in selecting areas to biopsy.

#### *3.3.6.5 Palliative care*

Depending on the stage of the tumour, treatment may either be with curative intent or terminal. In both cases palliative care can be provided. Palliative care involves dealing with the effects of the tumour, and therefore the symptoms, rather than treating the tumour itself. It may include the use of analgesics, chemotherapy and radiotherapy, and any specific symptoms should be taken care of as part of palliative care, whilst also offering psychological support.

### **3.3.7 LATE EFFECTS**

The long-term morbidity in survivors of childhood cancer relates mostly to the treatment received, i.e. the effects of surgery, chemotherapy and radiotherapy, but

can also result due to the cancer itself. In childhood tumours, treatment aims to give the child a good quality of life rather than only long-term survival.<sup>61</sup> The morbidity associated with late effects of treatment of brain tumours include effects on the endocrine system, neurological and cognitive effects, hearing and vision problems, and secondary tumours.<sup>62</sup>

In particular, radiotherapy and chemotherapy can have severe effects on the endocrine system and can effect, amongst others, growth, puberty and fertility. Children who receive radiotherapy and chemotherapy are monitored by an endocrinologist and hormone replacements are administered to those children suffering from hormone deficiencies in order to mitigate these effects.

Neurological and cognitive deficits are likely to occur in the treatment of brain tumours in children, but are specifically dependent on the location of the tumour and the aggressiveness by which they are treated. Nevertheless, the treatment of brain tumours in children is expected to impact on the cognitive and social abilities of the patient, and the psychological needs of these patients thus need to be addressed.

Furthermore, tumours such as optic pathway gliomas will impact on vision and can result in blindness, while certain types of chemotherapy can result in hearing impairments, with 12% of CNS tumour survivors being reported to have suffered chronic hearing loss<sup>36</sup>. Finally, the formation of secondary brain tumours following previous successful treatment cannot be ruled out.

In view of all the above late effects of treatment, patient follow-up needs to take place at a frequency which is patient and treatment dependent and in a setting which would ideally be multi-disciplinary in order to fit the needs of the patient.

#### **3.3.8 IMAGING**

Imaging is an important aspect of tumour diagnosis and management, and is generally carried out both before and after treatment. A number of imaging modalities exist with each having a specific purpose. Ultrasound can be useful for the diagnosis of abdominal and pelvic tumours, and plain x-rays can be useful for diagnosing bone

tumours<sup>36</sup>. However, when it comes to brain tumours, the major imaging modalities used are MRI, CT and PET.

CT is utilised for assessing calcification in tumours and PET is effective in determining the metabolic activity of the tumour and can be helpful in distinguishing tumour from radiation necrosis. Both CT and PET however carry a safety risk in terms of radiation dose. MR is the most commonly used imaging modality to assess brain tumours and apart from standard  $T_1$ ,  $T_2$  and post-contrast imaging, a number of advanced MR techniques have been employed in assessing brain tumours. In particular MR spectroscopy, perfusion and diffusion have been found to be valuable. MR spectroscopy can be used as a non-invasive technique for determining metabolic information and can aid the radiologist in identifying tumour tissue, differentiating tumour type and to guide stereotaxic biopsies. MR perfusion is a modality used to image the perfusion dynamics by determining the cerebral blood volume, the cerebral blood flow and the mean transit time. It can be helpful in grading tumours and distinguishing radiation necrosis from tumour recurrence. MR diffusion has been shown to be useful in analysing tissue cellularity and visualising the involvement of white matter tracts for treatment planning. Diffusion imaging as a tool for the diagnosis and management of brain tumours is explored in the next chapter, with a particular focus on paediatric brain tumours.

## Chapter 4 DIFFUSION IMAGING OF BRAIN TUMOURS

The aim of this chapter is to bring together the imaging and cancer chapters and describe current research in diffusion imaging of brain tumours, with a particular emphasis on that which led to the research carried out as part of this thesis. The chapter starts by describing the need for reproducibility studies and covers some of the reproducibility work which has already been published. This is followed by a literature review of diffusion imaging as a diagnostic and prognostic tool, and as a tool for treatment response. As paediatric work is limited, studies carried out both in adults and children are explored, with a focus on childhood brain tumours where possible.

### 4.1 Reproducibility Studies

#### 4.1.1 BACKGROUND

Repeated measurements taken using a specific method should, ideally, yield identical results. However, variations exist which may be both equipment-dependent and operator-dependent. Reproducibility refers to the ability of a method to be repeated so as to give similar results, and measures the variability that exists between repeated measurements. It is an important feature of any imaging technique as it shows that the method can be employed so that the resultant images are directly comparable to each other. A reproducible imaging measure should thus be independent of scanner, centre and time-point.

As mentioned, limited studies exist in childhood tumours and this may be a reflection of the difficulty of analysing tumours which are relatively rare and hence data is sparse. One way of reducing this limitation is to increase data available by combining data from multiple centres. Multi-centre studies are recognised to be essential not only in contributing to larger data sets but also in improving our understanding of how data can be used at different centres in order to aid clinicians with the diagnosis and management of brain tumours.

In order to be able to conduct any multi-centre imaging studies, we need to first ensure that data acquired at one centre is comparable to the data acquired at other centres. This can be done by carrying out multi-centre reproducibility studies. The importance of reproducibility studies can also be seen in terms of analysing data from different scanners, different centres, and multiple time points. Hence, in addition to multi-centre analyses, an analysis of reproducibility is important both in conducting single-centre longitudinal analyses and single-centre biomarker validation.

#### 4.1.2 PHANTOM STUDIES

One way of analysing reproducibility of diffusion parameters is through the use of phantoms. Phantom studies benefit from the fact that the same phantom can be scanned on multiple scanners and patient motion is not an issue. However, these studies lack the realism of in-vivo clinical studies and a number of ways of overcoming specific limitations have been explored.

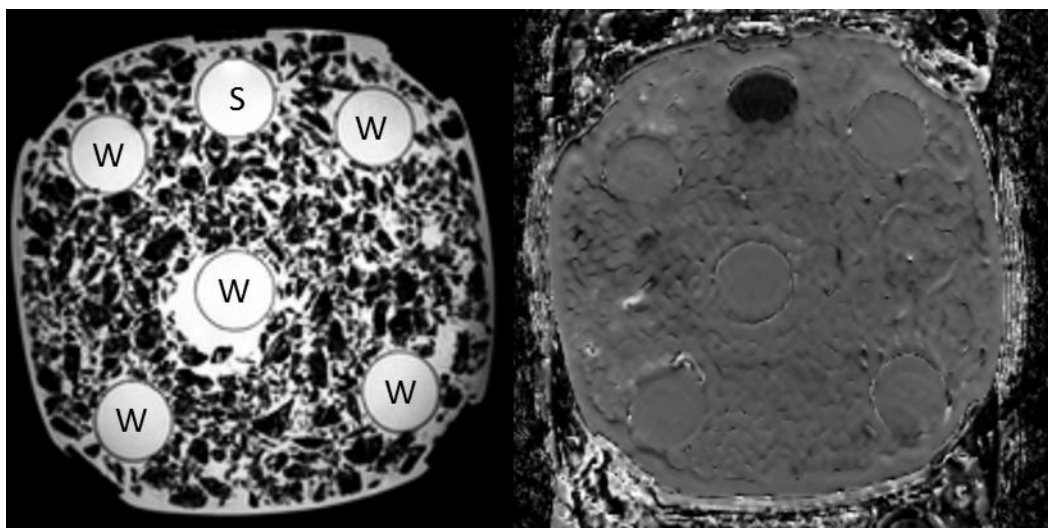


**Figure 4.1: Ice-water phantom.** The ice-water phantom consists of five water tubes (W) and one sucrose tube (S). The T1 image (left) shows the six tubes surrounded by a mixture of ice and water. The ADC image (right) is able to show the contrast between the tubes filled with water and the one tube filled with sucrose.

One of the limitations of scanning phantoms is that diffusion parameters are temperature dependent and while human temperature is relatively stable at 37°C, phantom temperature may easily differ. In order to overcome this, an ice-water

phantom was proposed, which ensures that the phantom is scanned at a fixed temperature of 0°C. The use of the ice water phantom has been shown by Chenevert et al<sup>63</sup> and Malyarenko et al<sup>64</sup>. Both studies were performed by the same group, with the second paper being an update of the first. The second study was conducted on thirty five scanners, from three manufactures and including both 1.5 and 3T machines, across eighteen sites. A standard sequence was used, with scan parameters allowing a certain degree of variability, accounting for manufacturer requirements and limitations. The basis of the ice-water phantom, shown in Figure 4.1, is that water at a temperature of 0°C has a known ADC value. In order to ensure that the water being scanned is at this temperature, the phantom is filled with ice-water, which will force the water in the tubes present in the phantom to stay at a temperature of 0°C until the ice is dissolved. Using this phantom, the authors of the study found ADC values between sites to vary by less than 3% at the iso-centre.

While the ice-water phantom has been shown to be useful in analysing ADC measurements, phantoms which are able to reproduce the white matter structures of the brain, and which would thus be ideal for analysing the reproducibility of FA, provide a bigger challenge. One study by Teipel et al<sup>65</sup> assessed the reproducibility of FA in a phantom consisting of a ring of fibres with constant anisotropy. The phantom was imaged on sixteen scanners, with only half of these having good enough quality to be used. The mean CV was in this case found to be 6.9%. New phantoms are able to create FA variations in phantoms<sup>66</sup> and their use could benefit the scientific community in measuring the reproducibility of FA parameters.

Phantom studies provide information about the inherent reproducibility of in-vivo clinical measurements and these studies are important in order to test reproducibility factors related to the scanner itself and the environment it is in, in a more feasible way. However, in-vivo studies provide a more realistic view of the reproducibility of imaging parameters in the clinic. Various in-vivo studies have been conducted, both on single-scanners and multiple-scanners, as discussed in the next sections.

#### 4.1.3 SINGLE-SCANNER STUDIES

Single-scanner studies give an understanding of the reproducibility of diffusion parameters from the same scanner. Knowledge of the intra-scanner reproducibility is important in conducting analysis which test the said parameters as biomarkers on a number of patients, or when a longitudinal study is carried out – with patients being scanned on the same scanner at two different time-points.

Very few reproducibility studies have been carried out in children. Bonekamp et al<sup>67</sup> analysed the ADC and FA in forty children aged 5.5 to 19.1 years on a single 1.5T scanner. In this case an identical protocol was used on all patients and a reproducibility analysis was carried out on ten of these with repeat scans taking place within 6 weeks from the initial scan. The reproducibility study compared ADC and FA values in six white matter fibre bundles. A coefficient of variation (CV) of between 0.8 and 3.4% was found for the ADC and between 2.6 and 5% for the FA.

Another DTI study was carried out on twenty two healthy adult volunteers by Veenith et al<sup>68</sup>. Each volunteer was scanned twice on a single 3T scanner with a maximum of 6 months between scans. Reproducibility was in this case analysed in twenty-three regions as defined by the Harvard Oxford subcortical atlas. In this case the mean ADC varied by 7.3% and the mean FA varied by 7.9%.

Both studies refer to the reproducibility of ADC as part of a DTI sequence and this ADC could thus also be referred to as the MD. A large difference in reproducibility can be seen between the two studies and this is likely to be due to the method applied to determine the regions of interest used (ROIs). While in the first study the region of interest (ROI) was defined by an observer working on a colour-coded FA map with grey matter signal suppression, in the second study the ROIs were defined in standard MNI space and though these were checked by a clinical investigator, errors due to registration are more likely. In observing the reproducibility of a given parameter, the method employed needs to be thus carefully considered.

#### **4.1.4 MULTI-CENTRE DWI STUDIES**

A few studies have been carried out on ADC parameters, as measured using a DWI protocol. One study by Sasaki et al<sup>69</sup> reports the reproducibility of ADC in twelve healthy volunteers imaged at seven institutions, on eight 1.5T scanners and two 3T scanners, and from four manufacturers. Similar but not identical protocols were used across all scanners. ADC measurements were made in grey and white matter and the reproducibility assessed. Excluding one of the manufacturers, the data from which showed a large difference with the rest of the scanners, the variability between manufacturers was found to be 7% at 1.5T. The variability between scanners was reported to be 8%. The relatively low reproducibility found in this study may be due to the method used to identify grey and white matter. These were determined by one of the authors, drawing an ROI around the bilateral frontal white matter and the thalamus. This provides a limited number of voxels to analyse and results are thus more prone to partial volume effect errors.

#### **4.1.5 MULTI-CENTRE DTI STUDIES**

A number of studies have been carried out on the reproducibility of DTI parameters<sup>65,70–73</sup>. The image protocol parameters were matched as closely as possible in all but one study where the standard manufacturer protocol was used. In that study, by Magnotta et al<sup>72</sup>, five healthy controls were imaged on eight 3T scanners from two manufacturers. MD and FA were measured in six regions of the brain. The intra-subject CV was <1% and the variability between manufacturers was found to be between 1 and 3%. While this study showed good reproducibility, other studies showed a lower FA reproducibility with a variability of 14% when using tract based spatial statistics<sup>65</sup> and variations of 10-15% in grey matter regions<sup>73</sup>.

The method employed can thus be seen to have a considerable impact on the reproducibility of FA parameters. In particular, FA in grey matter is low and it is expected to have poorer reproducibility than that of FA in white matter. Similarly to reproducibility in single-centre studies, careful consideration for the method employed needs to be taken into account when assessing reproducibility values.

#### 4.1.6 CURRENT NEEDS

While various studies have analysed reproducibility of diffusion parameters, most studies tend to use a carefully selected diffusion protocol. Further work carried out in the context of this thesis, and explored in Chapter 5, asks the question of whether diffusion imaging parameters are reproducible across multiple centres using standard clinical protocols.

### 4.2 Diffusion imaging as a diagnostic and prognostic tool

#### 4.2.1 BACKGROUND

Diffusion imaging has been used both to aid in the diagnosis of brain tumours and as a prognostic tool. Such tools are beneficial in assessing the tumour's aggressiveness, which can be in turn used in order to determine what treatment to apply. Firstly, the ADC has been shown to correlate with cell density. Secondly, diffusion imaging has been used in grading tumours and determining tumour types. Finally, diffusion biomarkers for determining the prognosis associated with a given tumour type has also been explored in the literature. This section gives an overview of research which has been carried out in these three areas.

#### 4.2.2 CELL DENSITY

The idea that ADC can be correlated with cellularity was first studied in gliomas by Sugahara et al<sup>74</sup>. Since then many studies have looked at the correlation between ADC and cellularity in different tumour types<sup>75-77</sup>. The basic principle is that the ADC is affected by the diffusion path tortuosity as shown in Figure 4.2. The relationship between ADC and cellularity was studied in more detail in vitro<sup>78</sup> and in the paediatric population<sup>79</sup>. It has been shown that the correlation is both related to the diffusion occurring in the extracellular space and also the diffusion taking place in the intracellular space<sup>78</sup>. Therefore it is not only cell count which affects the ADC, but also the nucleus-to-cytoplasm ratio<sup>79</sup>.

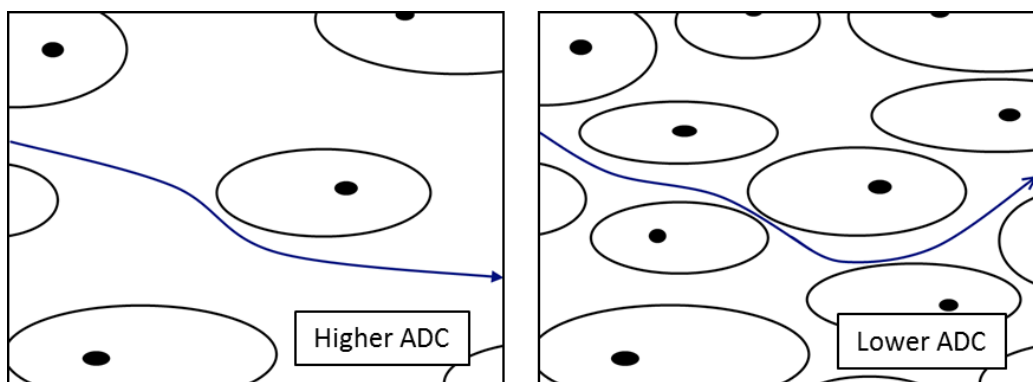


**Figure 4.2: ADC and tumour cellularity.** ADC is affected by the diffusion path tortuosity. In voxels with less cellular areas, the diffusion path is unrestricted and the ADC will be higher (left). Conversely, in voxels with highly cellular areas, the diffusion path is more tortuous and this restricted diffusion will result in a lower ADC.

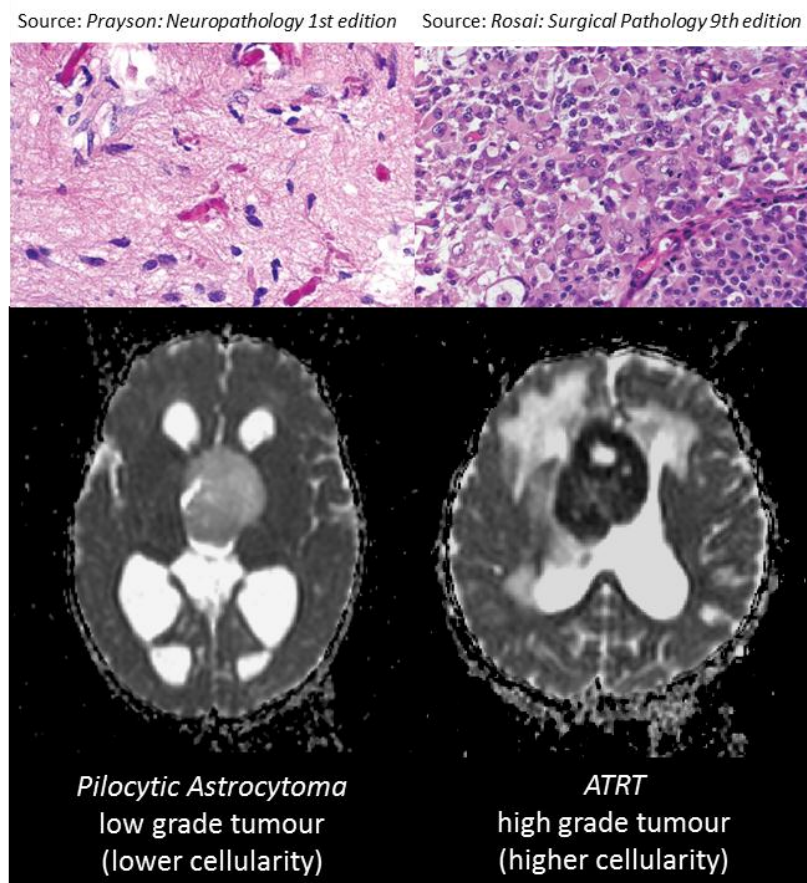


**Figure 4.3: Comparison between ADC and histology.** Tumours with lower cellularity appear brighter on ADC as can be seen in the low grade pilocytic astrocytoma (left). More cellular tumours appear darker on ADC as can be seen in ATRT (right). (Histology images obtained from <sup>80,81</sup>).

The correlation between cellularity and ADC is an important concept in diffusion imaging of brain tumours and a comparison between histology and ADC is shown in Figure 4.3. This correlation has also been studied in paediatric cerebellar tumours, suggesting that while a negative correlation was found between cellularity and ADC, tumour cellularity is unlikely to be the only cause for the difference in ADC<sup>82</sup>. In fact, while low grade tumours can indeed be more cellular than healthy brain tissue, the ADC in Figure 4.3 can still be seen to be higher in the low grade tumour as compared to the surrounding normal appearing brain tissue. This could be explained by the presence of microcystic areas in low grade tumours, driving the ADC to be higher than the less cellular healthy tissue.

While most studies have focused on ADC, the correlation between DTI measures and cell density has also been studied. As MD is very similar to ADC, a similar correlation is expected. However, while the ADC studies mentioned found a negative correlation, a positive but weak correlation has been found in one study<sup>83</sup>. In addition to this, the same study found a negative correlation between FA and cell density, while other studies found a positive correlation<sup>84,85</sup>. A link between FA and proliferation activity, as well as between FA and tumour infiltration has also been suggested in these same studies.

In conclusion, the majority of studies agree on the existence of a negative correlation between ADC and tumour cellularity and this forms the basis of other studies carried out in diffusion imaging on brain tumours, relating to both tumour grading and treatment management.

#### **4.2.3 TUMOUR CLASSIFICATION AND GRADING**

A number of studies have used diffusion imaging for paediatric brain tumour classification and grading and a plot showing the mean ADC in children with different tumours is shown in Figure 4.4. The basis for such studies is that it would provide a non-invasive way of determining the tumour type and grade.

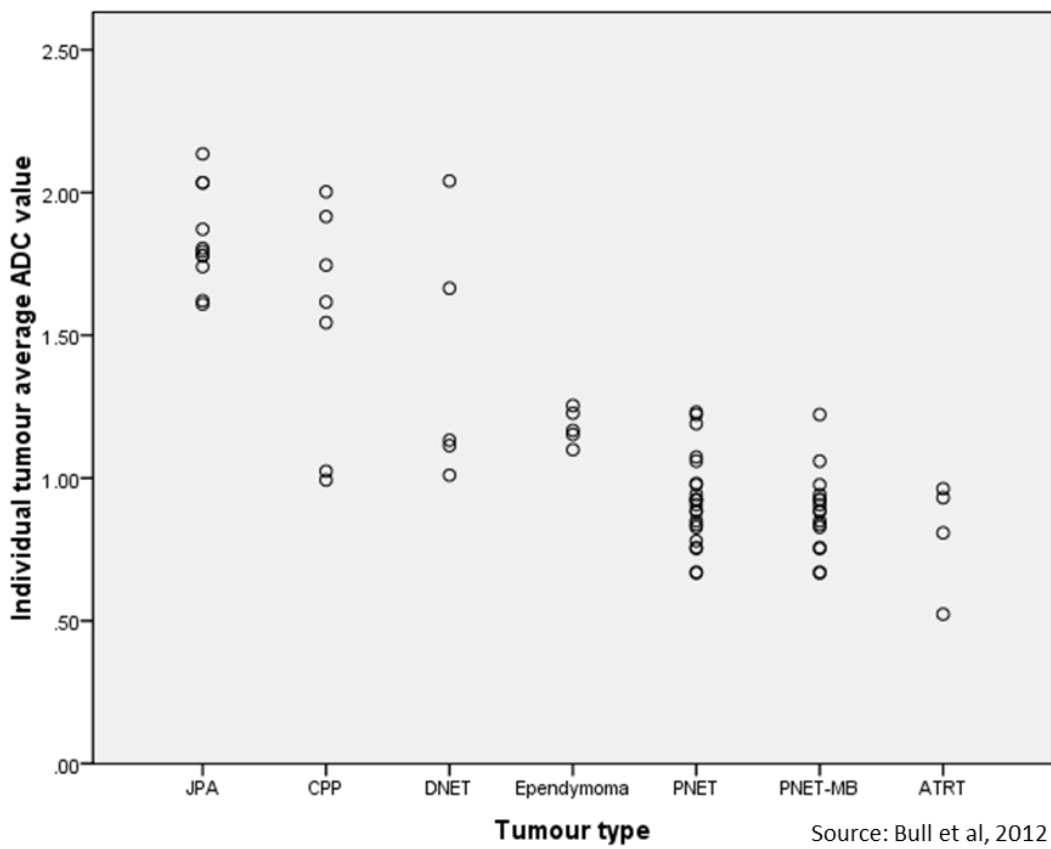


**Figure 4.4: Mean ADC by tumour type in a paediatric cohort.** The plot compares mean ADC in children with juvenile pilocytic astrocytoma (JPA), choroid plexus papilloma (CPP), dysembryoplastic neuroepithelial tumour (DNET), ependymoma, primitive neuroectodermal tumour including medulloblastoma (PNET), medulloblastoma (PNET-MB) and atypical teratoid rhabdoid tumour (ATRT). Using mean ADC, patients with JPA appear to be easily distinguishable from patients with PNET and ATRT, but not from patients with CPP and DNET. (Adapted from Bull et al, 2012<sup>86</sup>)

In one study by Bull et al<sup>86</sup> histogram analysis was performed on fifty-four paediatric brain tumour patients with JPA, choroid plexus papilloma, dysembryoplastic neuroepithelial tumour, ependymoma, PNET (excluding ATRT), and ATRT. The authors conducted a histogram analysis of ADC measures in the tumour, including the peak height, the mean, mode and the 10<sup>th</sup>, 25<sup>th</sup>, 50<sup>th</sup>, 75<sup>th</sup> and 90<sup>th</sup> percentile points. The overall success rate for discriminating between tumour types stood at 74.1%. The authors were able to differentiate between ATRT and other PNET tumours in all cases when these were studied separately from the rest of the tumours.

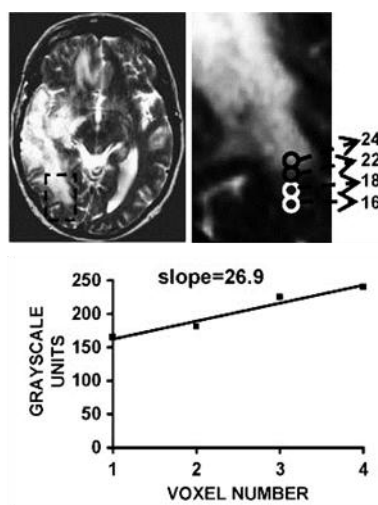
Another study on forty children with posterior fossa tumours (medulloblastoma, JPA and ependymoma) also showed the ability to discriminate between tumours using ADC histogram features<sup>87</sup>. Moreover, this study showed the ability to discriminate classic medulloblastoma from the other types using ADC texture features in 89.4% of the cases. The differentiation of the same tumour types using ADC<sup>88</sup> and using a combination of ADC and MR spectroscopy<sup>89</sup> were also previously shown. That said, an overlap in ADC between the different tumour types does exist and one study showed two out of the ten medulloblastoma tumours analysed did not exhibit restricted diffusion<sup>90</sup>.

Apart from differentiating between tumour types, other studies have also looked at whether ADC can be used to determine tumour grade. One study on twenty-four children with cerebellar tumours confirmed that ADC values were higher in low grade tumours (grades 1 and 2) than in high grade tumours (grades 3 and 4), and the study also suggests carefully excluding necrotic and oedematous areas before conducting the analysis<sup>91</sup>. In another study on supratentorial tumours in children less than one year old, the authors were able to differentiate between high and low grade tumours using the minimum ADC value in the tumour<sup>92</sup>. DTI measures have also been shown to differentiate between tumour grade in children with supratentorial tumours<sup>93</sup>.

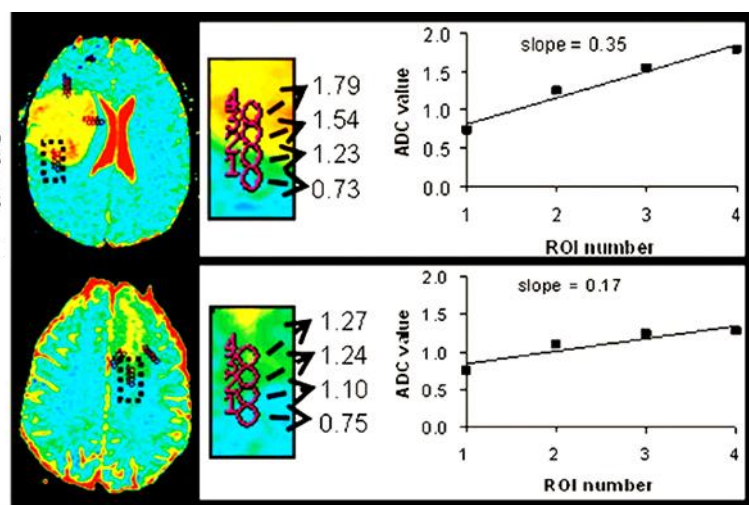
While diffusion imaging is unlikely to be an alternative to a histological analysis, it may prove to be useful in the clinical diagnosis by giving an indication of the tumour type and aiding the surgeons to determine the best area to biopsy, particularly in heterogeneous tumours. Diffusion imaging for classification of tumour types and grading may also be a valuable tool in diagnosing tumours which cannot be biopsied due to the tumour's location. Most studies carried out in paediatric brain tumours indicate diffusion imaging to be a good biomarker to help determine the tumour type. The use of diffusion imaging significantly improves diagnosis of paediatric cerebellar tumours<sup>94</sup>, with the accuracy of such diagnosis being increased when used in conjunction with other imaging techniques and modalities.

#### 4.2.4 PROGNOSTIC BIOMARKERS

Very few pre-treatment diffusion imaging biomarkers have been studied, with the majority of studies being conducted in adults. In one study a correlation was found between DTI metrics and progression free survival in patients with glioblastoma multiforme<sup>95</sup>. Another study showed a link between low ADC values and survival in malignant astrocytoma<sup>96</sup>. In other work, tumour border measures were studied as biomarkers of survival.



Source: Aghi et al, 2005



Source: Jenkinson et al, 2007

**Figure 4.5: Tumour border biomarkers.** The tumour border biomarker, as studied by Aghi et al, looked at the change in T2 values at the tumour border (left). Jenkinson et al applied this to ADC images. In both cases the biomarker consists of the gradient slope measured from four voxels, starting just outside the tumour border and entering towards the tumour core. (Adapted from Aghi et al, 2005<sup>97</sup> and Jenkinson et al, 2007<sup>76</sup>.)

Tumour border measures were studied as shown in Figure 4.5. Aghi et al<sup>97</sup> proposed a tumour border biomarker based on the T2 border sharpness coefficient but their work did not include diffusion imaging. A later study by Jenkinson et al<sup>76</sup> studied the tumour border measure in ADC images and termed it the apparent transient coefficient (ATC). In this study, oligodendroglial tumour genotypes were identified using variations in ADC and ATC. A third study analysed the ATC over the oedema and tumour boundaries in patients with glioblastoma multiforme and found a correlation between the tumour border measure and survival but not the oedema border measure<sup>98</sup>.

While various work has been carried out on tumour cellularity, classification and grading in paediatric tumours, little has been done in terms of prognostic biomarkers. Work carried out as part of this thesis has explored one such prognostic biomarker in children with embryonal brain tumours<sup>99</sup> and is presented in Chapter 6.

## 4.3 Diffusion imaging in treatment management

### 4.3.1 BACKGROUND

Imaging biomarkers which can be used in treatment management may have a significant impact on the outcome. First, imaging is required for treatment planning, particularly in surgical resection and identifying areas to biopsy, as well as in identifying the gross tumour volume to be targeted using radiotherapy. Second, advanced imaging techniques may provide to be useful in differentiating between confounds such as tumour recurrence and radiation necrosis, and in identifying cases of pseudoprogression. Finally, early identification of successful or unsuccessful treatment response could have a considerable impact on the management of brain tumour patients.

### 4.3.2 TREATMENT PLANNING

The main role of diffusion imaging in treatment planning lies in planning the resection itself. When considering surgery, the goal is to achieve a complete tumour resection, with the minimal neurologic deficit possible. This implies that for treatment planning, delineation of the tumour margins as well as locating the important structures and white matter pathways is of high importance. Using tractography, DTI is able to construct white matter pathways which can be visualised by the surgeon prior to surgery, and DTI findings can suggest how white matter is involved with the tumour. Studies have been carried out evaluating the use of DTI in pre-operative surgical planning both in adults<sup>100</sup> and in children<sup>101</sup>. The use of intra-operative DTI has also been explored in treating brain tumours, and a greater surgical precision with less associated morbidity has been observed in those cases<sup>102,103</sup>.

### 4.3.3 DIFFERENTIATING IMAGING CONFOUNDS

Another important use for an imaging tool would be the ability to differentiate between confounds seen in standard imaging techniques post therapy; more specifically, the ability to differentiate between tumour recurrence and radiation necrosis, as well as the ability to differentiate between tumour progression and pseudoprogression.

Radiation necrosis may appear the same as tumour recurrence, both radiologically and clinically. It is a reaction to radiotherapy, occurring anytime from a few months to many years after treatment, and which results in the disruption of the blood brain barrier, oedema and mass effect<sup>59</sup>. Differentiation between tumour recurrence and radiation induced injury using diffusion imaging has been widely explored in the literature. ADC has been shown to contribute to making the right diagnosis, with lower ADC values seen in the recurrent tumour group<sup>104,105</sup>. Other case reports have looked at a few cases using FA and determined that FA may also be useful in differentiating between the two groups<sup>106</sup>. Furthermore, other imaging modalities such as PET, or combining advanced MRI techniques such as perfusion and diffusion imaging could aid in making a reliable diagnosis between radiation necrosis and tumour<sup>107</sup>.

Another confound which may exist is that of pseudoprogression. It is a reaction to chemotherapy and radiotherapy, normally occurring two to three months after treatment, and which results in inflammation, oedema and increased vessel permeability<sup>59</sup>. Similarly to the differentiation between radiation induced necrosis and tumour recurrence, many studies have been carried out on the use of diffusion imaging for differentiation of pseudoprogression from true progression. These studies have determined the ADC to be a valuable biomarker in distinguishing between the two<sup>108–110</sup>.

While numerous studies have been done on both confounders in adults, very limited work has been carried out in paediatric brain tumours. In one case report of pseudoprogression in a 6 year old patient, diffusion imaging provided to be useful in carrying out the correct diagnosis<sup>111</sup>.

#### 4.3.4 TREATMENT RESPONSE

One of the major uses of diffusion imaging in the management of brain tumour treatment has been in the area of treatment response. Currently change in tumour size, generally a few weeks after treatment, is the main method used clinically to determine treatment response. Post-treatment imaging is compared to the pre-treatment image in order to determine whether the tumour decreased in size and thus responded to treatment. This method of assessing treatment response implies that follow-up imaging is carried out too late for clinicians to be able to alter the treatment given in cases with unresponsive tumours. Identifying good biomarkers of early treatment response is important in order to allow for a change in the tumour treatment protocol when necessary and possible, and also in order to validate new therapeutic drugs being studied. A large number of studies have been carried out on changes in diffusion imaging measures after treatment.

One of the areas where the effects of treatment response on diffusion imaging have been explored is that of assessing response to steroid treatment. Steroids are commonly used to treat symptoms of brain tumours and although their mechanism of action is not well understood, it is hypothesized that they act so as to reduce the volume of water inside oedematous regions<sup>112</sup>. It is thus expected that the diffusion coefficient is lower post-steroid treatment. Studies have in fact reported a decrease in the diffusion coefficient both within the tumour<sup>112,113</sup> and peri-tumoural oedema<sup>113,114</sup>. While another study did not find a significant change in the diffusion coefficient when low-dose steroids were used<sup>115</sup>.

Diffusion imaging has also been explored as a tool for identifying response to radiotherapy and chemotherapy. As such the two main uses of diffusion imaging in identifying tumour response to treatment are the use of ADC histograms<sup>116,117</sup> and the functional diffusion map (fDM)<sup>118-121</sup>. In histogram analysis, ADC values are seen to shift upwards at treatment response, such that the mean of the histogram post-treatment is higher than that pre-treatment, and the post-treatment histogram would have a lower kurtosis and thus a wider spread. The analysis however is carried out over the whole tumour area, and thus lacks spatial information in heterogeneous tumours.

The fDM attempts to capture the spatial information by analysing treatment response in individual voxels.

The fDM, also known as the parametric response map, was first described by Moffat et al<sup>118</sup> and is shown in Figure 4.6 and Figure 4.7. The technique involves a voxel-by-voxel comparison of pre-treatment and, either mid- or post-treatment data, for patients with tumours using ADC images. It works on the basic principle that ADC will increase with effective treatment – which would imply a decrease in tumour cellularity, and decrease with unsuccessful treatment – which would imply an increase in tumour cellularity. The fDM was proposed as a biomarker of early treatment response with studies showing good prediction of survival as early as 3 weeks after start of treatment<sup>122</sup>. A histological and receiver operating characteristic analysis has been carried out in order to validate the fDM and determine what thresholds are best to use in building the fDM<sup>121</sup>.

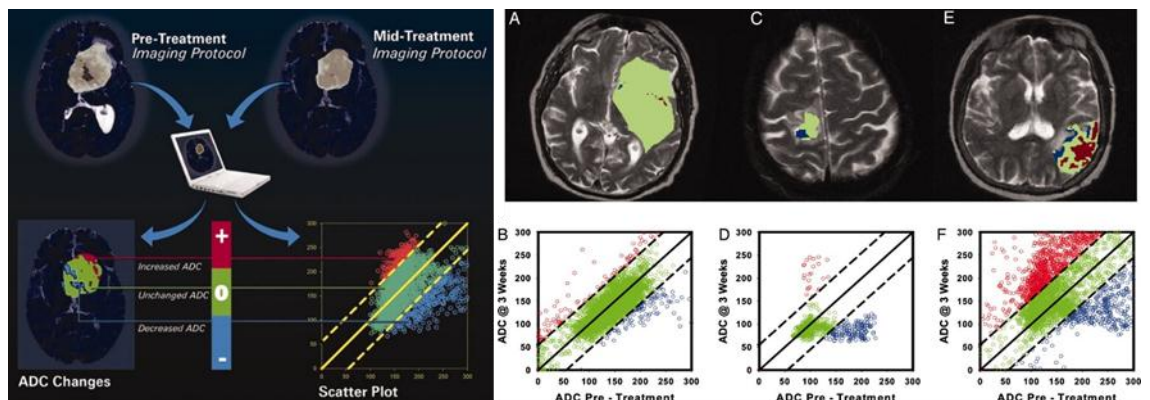


**Figure 4.6: The functional diffusion map.** The fDM was proposed as a biomarker of early treatment response. The difference between pre- and mid-treatment images is computed and an increase in ADC is labelled in red, a decrease in ADC in blue and no change in ADC in green. A scatter plot of overall changes can then be drawn (left pane). The scatter plots B, D and F correspond to the tumours in A, C and E: patient A showed progressive disease, patient C stable disease and patient E treatment response (right pane). In the study no change in ADC was said to imply that the tumour did not respond to therapy and thus represented progressive disease. (Adapted from Moffat et al, 2005.<sup>118</sup>)

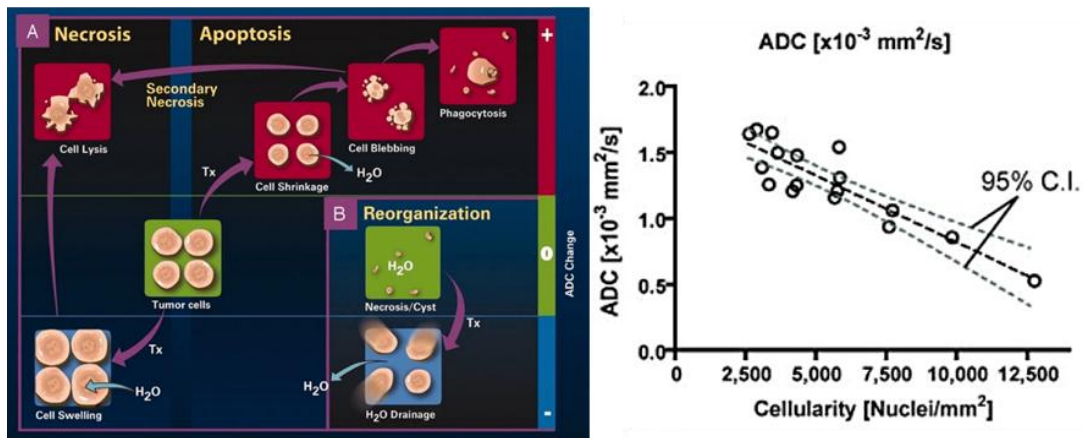


**Figure 4.7: Biology of the fDM.** The biological processes affecting the fDM where first described as shown in the left pane. Cells which respond to treatment can undergo a transient cell swelling, implying a decrease in ADC, before becoming necrotic and increasing in ADC; cells may also die through cell shrinkage and apoptosis (A). Necrotic areas may also reorganise such that cells move into the area and in this case a decrease in ADC is observed (B). Cells which did not respond to therapy were said to remain unchanged in ADC. However, other studies, as shown on the right, described the biology of the fDM to be related to a change in cellularity, postulating that an increase in ADC is related to a decrease in cellularity and a decrease in ADC is related to an increase in cellularity. (Adapted from Moffat et al, 2005<sup>118</sup> (left) and Ellingson et al, 2010<sup>121</sup> (right))

Work on the functional diffusion map has mostly concentrated on adult brain tumours. One study has however analysed the fDM in high grade paediatric brain tumours and found a good correlation between the changes in ADC and response to treatment<sup>123</sup>. A study on the challenges posed to the functional diffusion map in a range of paediatric brain tumours was carried out as part of this thesis<sup>124</sup> and is presented in Chapter 7.

## Chapter 5 REPRODUCIBILITY OF DIFFUSION IMAGING PARAMETERS

This chapter presents research carried out on the reproducibility of diffusion imaging parameters. The content of this chapter has been adapted from a paper prepared to be submitted for publication, the abstract of which has been accepted for a conference presentation<sup>125</sup>.

### 5.1 Background

Diffusion imaging is widely used both in research and in the clinic. In areas where clinical data is sparse, such as paediatric oncology or other rare diseases, it may be necessary to include data from multiple centres in order to conduct a sufficiently powered analysis. While the availability of multi-centre data may be beneficial in terms of increasing the amount of data available for a given study, it introduces the question of whether such data, obtained using standard clinical sequences and on different scanners with different field strengths, is comparable. This question may also arise in carrying out longitudinal studies, where the same patient may be scanned on the same or a different scanner to that used in the previous imaging session. The aim was thus to validate clinical diffusion imaging measurements across multiple centres and on different scanners.

The basis of this study was to determine the reproducibility of diffusion measures, commonly used in multisite clinical research studies, on both a phantom and a group of volunteers, each being scanned at multiple sites and on different scanners. In this study, diffusion weighted imaging (DWI)<sup>7</sup> and diffusion tensor imaging (DTI)<sup>11</sup> parameters were analysed. More specifically the reproducibility of the mono-exponential fit to DWI – the apparent diffusion coefficient (ADC); the bi-exponential fit to DWI as applied through intra-voxel incoherent motion (IVIM)<sup>9</sup>; and the mean diffusivity (MD) and fractional anisotropy (FA) obtained from DTI datasets were investigated.

While previous studies have been carried out examining the reproducibility of these parameters at a single centre<sup>26,68</sup> and at multiple centres<sup>69,72,73</sup>, most studies aimed to match the imaging sequence used across all scanners. Only one of these studies was carried out on a mixture of 1.5T and 3T scanners and this study analysed the reproducibility of ADC only<sup>69</sup>. The aim of this study was to quantify the reproducibility of DWI and DTI parameters acquired with sequences in routine clinical use locally (and therefore not specifically optimised or matched for multi-site comparison). This was conducted on scanners from two manufacturers and two field strengths in order to assess the reproducibility of the quantified diffusion parameters.

## 5.2 Materials and Methods

### 5.2.1 VOLUNTEERS

Nine healthy volunteers (7 male, 2 female; aged 25 to 34 years at first scan; mean 29 years) were enrolled in this multi-centre study. Ethical approval was given by the research ethics committee and informed consent was obtained at all centres. All data was anonymised in accordance with the Data Protection Act, UK.

### 5.2.2 SCANNERS

Eight scanners (three Siemens Avanto 1.5T, one Siemens Symphony 1.5T and four Philips Achieva 3T) across five centres were used in this study. Between four and eight volunteers were scanned on each scanner, with repeat scans performed on a different date to the first scan on one or two volunteers on each scanner. All scans were performed over a period of 18 months and in total 65 imaging sessions took place across the five centres.

### 5.2.3 PHANTOM

An ice water phantom<sup>64</sup> was scanned on all scanners. Different fluids will have a varying ADC value which also varies according to temperature, with ADC in water measured between  $1.756 \times 10^{-3} \text{ mm}^2\text{s}^{-1}$  at  $15^\circ\text{C}$  and  $2.616 \times 10^{-3} \text{ mm}^2\text{s}^{-1}$  at  $30^\circ\text{C}$ <sup>126</sup>. The advantage of using ice-water is that the temperature is fixed, and is not affected by the temperature inside the scanner room. Ice-water is expected to have an ADC of  $1.099 \times$

$10^{-3}\text{mm}^2\text{s}^{-1}$ .<sup>127</sup> The ice-water phantom used consisted of five tubes filled with distilled water and one tube filled with sucrose. The phantom was filled with ice and water in order to bring the temperature of the fluid-filled tubes down to 0°C. Measurements were taken in the water-filled tubes.

#### **5.2.4 IMAGING PROTOCOL**

Tables 5.1 and 5.2 show the clinical protocols used at the different centres and scanners for DWI and DTI. These protocols were applied in the study, with the addition that in all centres b-values of 0, 50, 100, 300, 500, 600 and 1000 were acquired for the DWI protocol. DWI data was acquired on all eight scanners, while DTI data was acquired on seven scanners. In addition, a high resolution T1 weighted image was acquired at each centre.

**Table 5.1: DWI protocol.**

Centre	Great Ormond Street Hospital for Children NHS Trust		St George's Hospital	The Royal Marsden NHS Foundation Trust		Nottingham University Hospital NHS Trust	Birmingham Children's Hospital	
Scanner	A	B	C	D	E	F	G	H
Manufacturer	Siemens	Siemens	Philips	Siemens	Philips	Philips	Siemens	Philips
Model	Avanto	Symphony	Achieva	Avanto	Achieva	Achieva	Avanto	Achieva
field strength (T)	1.5	1.5	3	1.5	3	3	1.5	3
head coil channels	12	8	32	12	8	8	2	32
TR (ms)	2700	3500	3800	3800	3800	3280	4400	3800
TE (ms)	96	109	74	73	73	73	89	74
b values	0, 500, 1000	0, 500, 1000	0, 1000	0, 50, 100, 300, 600, 1000	0, 50, 100, 300, 600, 1000	0, 1000	0, 1000	0, 1000
FOV (mm)	230 x 230	230 x 230	230 x 230	230 x 230	230 x 230	224 x 224	230 x 230	230 x 230
no. of slices	19	19	22	22	22	32	28	22
slice thickness (mm)	5	5	5	5	5	4	5	5
acquired matrix	128 x 128	128 x 128	128 x 128	128 x 128	128 x 128	112 x 112	192 x 192	128 x 128
interpolated matrix	128 x 128	256 x 256	256 x 256	256 x 256	256 x 256	224 x 224	192 x 192	256 x 256
orientation	axial	axial	axial	axial	axial	axial	axial	axial
Bandwidth (Hz/px)	1502	1500	2308	1860	1860	2441	1240	2307
Parallel imaging	2	none	2	2	2	2	2	2
NSA	3	2	3	3	3	2	1	3
voxel size (mm)	1.8 x 1.8 x 5	0.9 x 0.9 x 5	0.9 x 0.9 x 5	0.9 x 0.9 x 5	0.9 x 0.9 x 5	1 x 1 x 4	1.2 x 1.2 x 5	0.9 x 0.9 x 5
SNR*	15	6.6	-	12.9	-	-	4.4	-

\*SNR measured as per equation (5.1). SNR was not measured in Philips scanners as SENSE parallel imaging suppresses background noise and does not give a signal outside of the head.

**Table 5.2: DTI protocol.**

Centre	Great Ormond Street Hospital for Children NHS Trust	St George's Hospital	The Royal Marsden NHS Foundation Trust		Nottingham University Hospital NHS Trust	Birmingham Children's Hospital	
Scanner	A	C	D	E	F	G	H
Manufacturer	Siemens	Philips	Siemens	Philips	Philips	Siemens	Philips
Model	Avanto	Achieva	Avanto	Achieva	Achieva	Avanto	Achieva
field strength(T)	1.5	3	1.5	3	3	1.5	3
head coil channels	12	32	12	8	8	2	32
TR (ms)	7300	6000	7300	7767	6268	6510	6000
TE (ms)	81	70	81	70	53	86	70
b values	0, 1000	0, 1000	0, 1000	0, 1000	0, 1000	0, 1000	0, 1000
FOV (mm)	240 x 240	240 x 240	240 x 240	240 x 240	240 x 240	240 x 231	240 x 240
no. of slices	60	48	60	70	56	51	48
slice thickness (mm)	2.5	2.5	2.5	2	2.5	2.5	2.5
matrix	96 x 96	96 x 96	96 x 96	128 x 128	96 x 96	108 x 104	96x96
Bandwidth (Hz/px)	1447	3324.3	1447	1783	3321	1493	3324
parallel imaging	2	2	2	2	2	2	2
NSA	1	1	1	2	1	2	1
gradient directions	60	32	30	32	15	20	32
b-zeros	3	1	5	1	1	1	1
voxel size (mm)	2.5 x 2.5 x 2.5	2.5 x 2.5 x 2.5	2.5 x 2.5 x 2.5	1.875 x 1.875 x 2	2.5 x 2.5 x 2.5	2.2 x 2.2 x 2.5	2.5 x 2.5 x 2.5

### 5.2.5 DATA ANALYSIS

#### 5.2.5.1 Signal-to-noise Ratio

The signal-to-noise ratio (SNR) was measured according to equation (5.1), suggested in <sup>128</sup> and also used previously in measuring SNR in diffusion imaging<sup>129</sup>. The reported SNR was calculated on the unweighted ( $b_0$ ) DWI image, as the average SNR measured in two volunteers who were scanned across all scanners.

$$SNR = \frac{mean(S)}{stddev(N)} \times 0.6551 \quad (5.1)$$

where  $SNR$  is the signal-to-noise ratio,  $mean(S)$  is the average signal in a region of interest of the image – chosen to include whole brain grey and white matter volumes,  $stddev(N)$  is the standard deviation in a region of interest of the image consisting of noise – chosen to include the first ten rows of the image across all slices, and 0.6551 is a correction factor included to adjust for the Rician distribution of noise in a magnitude image, which is equivalent to a Rayleigh distribution for image regions with no signal<sup>130,131</sup>.

#### 5.2.5.2 Segmentation

In volunteers, DWI and DTI parameters were measured in grey and white matter. For DWI parameters, the masks for grey and white matter were created by segmenting the  $b_0$  image using SPM<sup>23</sup> and a probability threshold of 0.95. For the DTI parameters, the masks were created by segmenting the  $S_0$  image – the estimated  $b_0$  image output by FSL<sup>27</sup>.

DWI and DTI parameters were also measured in eight brain regions which could be particularly affected by neurological diseases and conditions seen in the clinic, with a particular emphasis on regions affected by paediatric brain tumours. The regions studied included the cerebellar white matter, cerebellar grey matter, brain stem, cerebral white matter, basal ganglia, thalamus, choroid plexus, and optic chiasm (shown in Figure 5.1). The masks for these areas were created by segmenting high-resolution T1-weighted images using FreeSurfer<sup>28,132–134</sup>. High-resolution T1-weighted images were not available for all volunteers on scanner D and one volunteer on

scanner G and hence these were excluded from the analysis. Furthermore, the segmentation failed on one volunteer on scanner H. Thus the analysis was conducted on 56 imaging sessions for DWI and on 47 imaging sessions for DTI. The mean value for the DWI parameters in these regions were calculated by registering the  $b_0$  image to the high-resolution T1-weighted image, then subsequently applying the same transformation to ADC, D and f. Similarly, the mean value for the DTI parameters in these regions were calculated by registering the S0 image to the high-resolution T1-weighted image and subsequently applying the same transformation to MD and FA. In order to avoid partial volumes, an image erosion process of one voxel was used on the masks output by FreeSurfer prior to applying these to the registered DWI and DTI parameters. All registration was performed using an affine 12-parameter model with tri-linear interpolation in FLIRT, the linear image registration tool provided by FSL<sup>135</sup>.

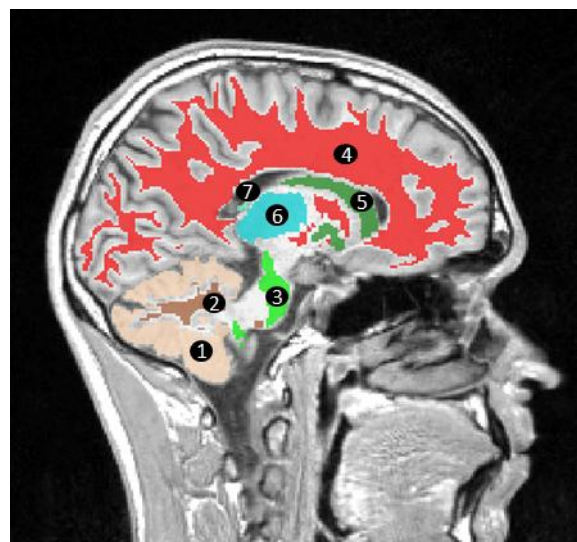


**Figure 5.1: Segmentation of T1-weighted images.** Using FreeSurfer. T1-weighted images were segmented in order to create masks defining: cerebellar cortex (1), cerebellar white matter (2), brain stem (3), cerebral white matter (4), basal ganglia (including the caudate nucleus, the putamen and the globus pallidus) (5), thalamus (6) and choroid plexus (7). A mask for the optic chiasm (not shown) was also defined using FreeSurfer.

#### 5.2.5.3 Apparent diffusion coefficient

The ADC was calculated through custom written MATLAB scripts using equation (5.2) to calculate the linear fit to the clinical b-values shown in Table 5.1.

$$ADC = -\ln\left(\frac{S_b}{S_0}\right)/b \quad (5.2)$$

where  $s_b$  is the signal at the specific  $b$ -value, and  $s_0$  is the signal at  $b_0$ .

In the phantom the ADC was calculated in the ice-water tubes by manually drawing a region of interest (ROI) over the tubes, avoiding boundary regions in order to include only areas of water, and calculating the mean ADC over the area. In volunteers, the segmented images were used as masks to calculate the mean ADC in grey matter, white matter, and in the eight regions mentioned.

#### 5.2.5.4 *Intra-voxel incoherent motion*

DWI data were processed using the IVIM model<sup>9</sup>, which assumes that two diffusing species give rise to the observed signal during in vivo DWI. These are the incoherent flow of blood-water in the randomly orientated micro-vascular network (referred to as fast, micro-circulation driven pseudo-diffusion), and the molecular, thermally driven diffusion of water molecules in the extra-vascular space. Using this model, the observed signal intensity ( $S$ ) at a given level of diffusion weighting ( $b$ ) is given by equation (5.3).

$$\frac{S(b)}{S_0} = (1 - f)e^{-bD} + fe^{-b(D+D^*)} \quad (5.3)$$

where  $s_0$  is signal intensity without diffusion-weighting,  $D$  is the diffusion coefficient of water molecules in the tissue,  $D^*$  is the fast pseudo-diffusion coefficient, and  $f$  is the fraction of the total DWI signal which arises from the latter compartment.

The fitted parameters ( $f$ ,  $D$ , and  $D^*$ ) were obtained in a stepwise-sequential manner, due to limitations in the precision of fitting equation (5.3) directly to DWI data<sup>136</sup>. Firstly, linear regression of  $\ln(S/S_0)$  vs  $b$  was used to obtain  $D$ , using only data acquired with  $b \geq 300 \text{ s/mm}^2$ , at which the fast diffusing component ( $D^*$ ) is negligible due to the dephasing caused by the diffusion gradients. Raw data from all  $b$ -values were then used to fit  $f$  and  $D^*$  (with  $D$  fixed), using an iterative Nelder-Mead nonlinear least squares algorithm. The mean values of  $D$  and  $f$  for both phantom and volunteers were derived through the same masks used for measuring the mean ADC.

### 5.2.5.5 Diffusion tensor imaging

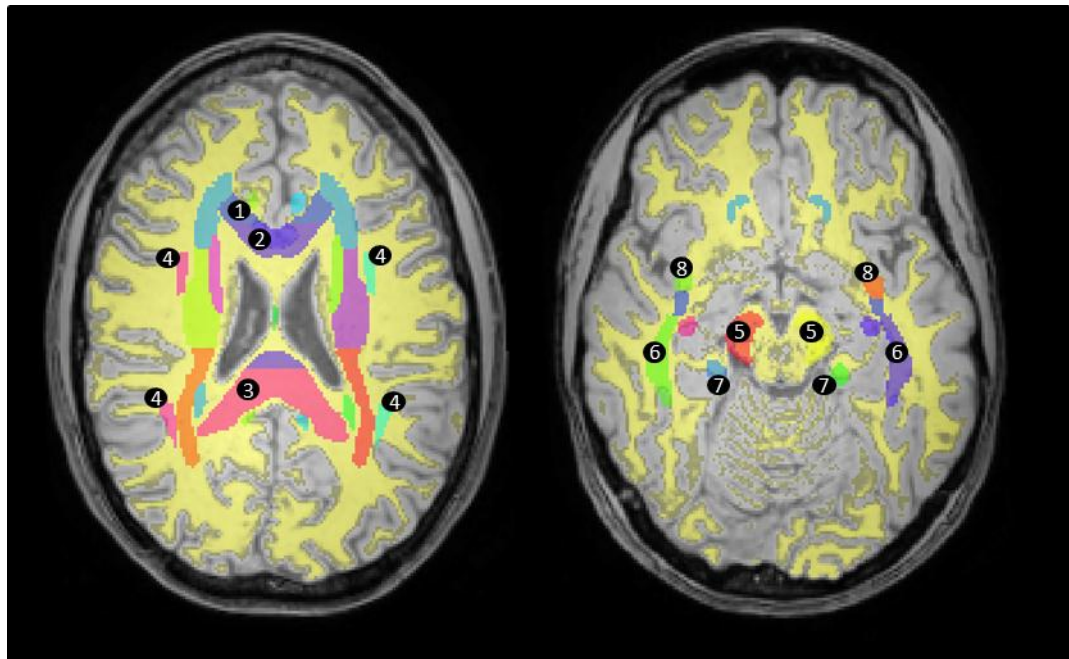


**Figure 5.2: Measuring FA in white matter areas.** The segmented white matter mask (yellow) is shown overlaid on a high-resolution T1 weighted image registered to standard MNI space. The ICBM-DTI-81 atlas (coloured areas) was used in order to measure the FA in areas defined as white matter according to the segmented mask in specific tracts: genu of the corpus callosum (1), body of the corpus callosum (2), splenium of the corpus callosum (3), superior longitudinal fasciculus (4), cerebral peduncle (5), sagittal stratum (6), cingulum (7), uncinate fasciculus (8).

Mean diffusivity (MD) and fractional anisotropy (FA) were calculated through dtoa software<sup>20</sup> which uses FSL<sup>27</sup> to compute the DTI parameters following eddy current correction. In the phantom the MD and FA in the ice-water tubes were calculated by manually drawing an ROI over the tubes, excluding boundary areas, and calculating the mean MD and FA in these areas. In the volunteers, similarly to ADC, segmented images were used to calculate the mean MD and FA in grey matter, white matter, and in the eight brain regions described. In addition, for the FA analysis, the ICBM-DTI-81 atlas<sup>137</sup> available in FSL was used to measure the mean FA in specific white matter ROIs shown in Figure 5.2. This was done by first registering the S<sub>0</sub> image to standard MNI space, then performing the same registration to the derived FA map, and then segmenting the S<sub>0</sub> image to obtain a mask for the white matter. The mean FA in the ROIs was

determined by overlaying the white matter mask and the atlas to the registered FA map, shown in Figure 5.2.

### 5.2.6 STATISTICAL ANALYSIS

Statistical analysis on the phantom data consisted of measuring the coefficient of variation (CV), as defined by equation (5.4), using the group mean and standard deviation of each measured mean ADC value in ice-water, across all scanners.

$$CV = \sigma/\mu \times 100\% \quad (5.4)$$

where  $\sigma$  is the standard deviation and  $\mu$  is the mean

Statistical analysis for the volunteer data was conducted using R software<sup>29</sup> and the lme4 package therein<sup>138</sup>. In order to calculate the reproducibility of the above mentioned parameters, a mixed effect model was used. The volunteer was considered as a random effect with the scanner considered as a fixed effect. The mixed effect model gives a mean and standard deviation for the fixed effects, together with the standard deviation expected for the random effect and an error-term which is considered to be the variation that can be expected in addition to both random and fixed effects. The CV was then calculated from the mean and standard deviation in order to measure the reproducibility of the given measures across different scanners (the inter-scanner CV), across different volunteers (inter-volunteer) and irrespective of volunteer or scanner (the intra-scanner CV). The model was also constructed separately for 1.5T and 3T scanners in order to study whether there is any major difference in reproducibility between the two field strengths.

## 5.3 Results

### 5.3.1 PHANTOM

Results for the ice-water phantom are shown in Table 5.3, together with comparison images shown in Figure 5.3. Values for ADC, D and MD were comparable and very similar. The team imaging with scanner F confirmed that when the phantom was scanned, it was not given enough time to reach thermal equilibrium at 0°C and consequently produced higher values than in the other scanners. Hence, calculations

were also done excluding this scanner, which improved the CV for ADC, D and MD to 0.7, 1.4 and 0.9% respectively. FA and f had a low reproducibility in the phantom. It was noted that f, at a value of 0.0591, was much higher for scanner G, compared to all other scanners. Excluding scanner G and scanner F, the mean estimated value of f in the phantom was 0.0120, with a standard deviation of 0.0033 and a CV of 27.3%.

**Table 5.3: Reproducibility of the ice-water phantom.** The table shows the mean ADC, D, f, MD and FA for the ice-water phantom together with the associated standard deviation. The CV was computed and shown for each of these parameters.

ice-water phantom	DWI		IVIM		DTI	
	ADC mean $\pm$ std $\times 10^{-3} \text{ mm}^2 \text{s}^{-1}$	D mean $\pm$ std $\times 10^{-3} \text{ mm}^2 \text{s}^{-1}$	f mean $\pm$ std	MD mean $\pm$ std $\times 10^{-3} \text{ mm}^2 \text{s}^{-1}$	FA mean $\pm$ std	
Scanner	A 1.1103 0.0214	1.1041 0.0275	0.0114 0.0097	1.1030 0.0177	0.0226 0.0177	
	B 1.1116 0.0218	1.1148 0.0258	0.0115 0.0102	- -	- -	
	C 1.1064 0.1070	1.1010 0.0274	0.0181 0.0137	1.0966 0.0271	0.0392 0.0149	
	D 1.0971 0.0173	1.1060 0.0211	0.0081 0.0087	1.0921 0.0176	0.0240 0.0177	
	E 1.1106 0.0191	1.1218 0.0169	0.0120 0.0141	1.1191 0.0315	0.0473 0.0234	
	F 1.1525 0.0991	1.2059 0.0930	0.0229 0.0189	1.1884 0.0344	0.0488 0.0247	
	G 1.1092 0.0914	1.1428 0.1147	0.0591 0.0451	1.0989 0.0240	0.0370 0.0145	
	H 1.1223 0.0325	1.1346 0.0316	0.0110 0.0096	1.1116 0.0206	0.0405 0.0180	
overall	1.1150 0.0167	1.1289 0.0345	0.0193 0.0168	1.1157 0.0334	0.0371 0.0103	
CV	1.5%	3.1%	87.1%	3.0%	27.8%	

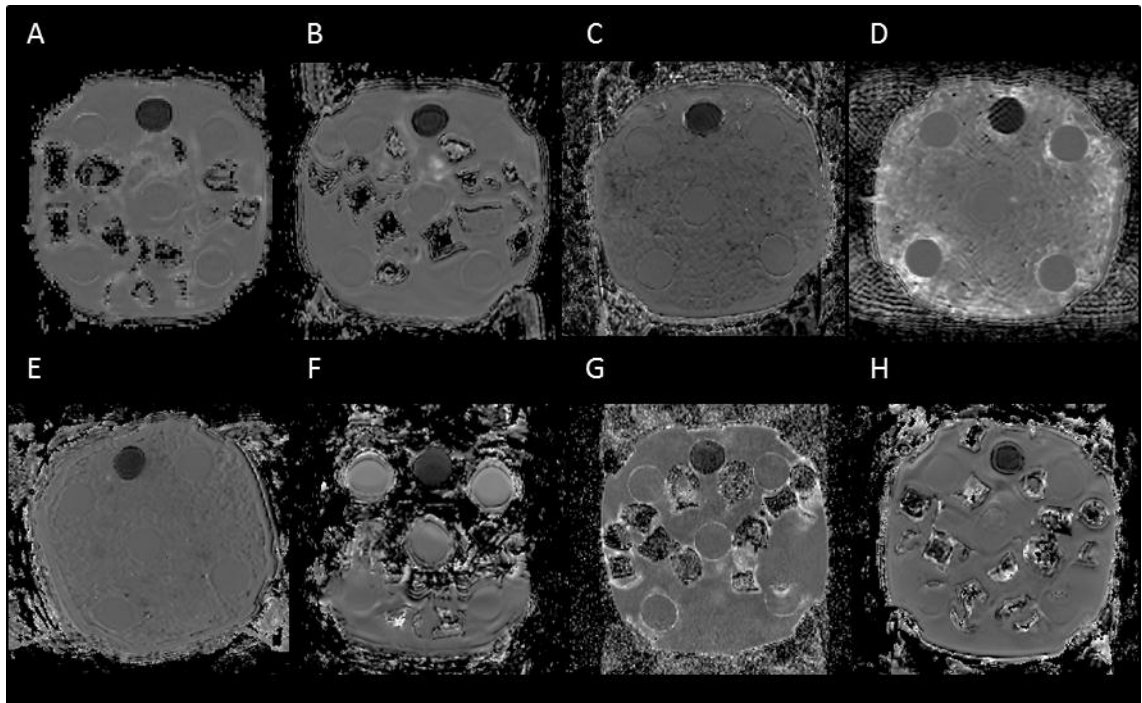


**Figure 5.3: Comparison of the ice-water phantom ADC images across scanners.** Images of the phantom from each of the scanners using the same contrast range are shown. The tube filled with sucrose appears darker while the five tubes filled with distilled water are evenly spaced away from each other and can be seen to be surrounded by iced-water. The protocol for scanning the phantom was not adhered to for scanner F, with the image showing that iced-water was not surrounding all of the tubes at acquisition.

### 5.3.2 VOLUNTEERS

Box plots showing the range of values observed in all volunteers across all scanners are shown for grey matter in Figure 5.4 and for white matter in Figure 5.5. Results for reproducibility of ADC, D, f, MD and FA in grey matter, white matter and the eight brain regions for volunteer scans are shown in Tables 5.4 to 5.8 respectively. The tables show the mean, standard deviation and CV results from the mixed-effect model describing the variation expected if the same volunteer is scanned on a different scanner (inter-scanner reproducibility), if a different volunteer is scanned on the same scanner (inter-volunteer), and if the same volunteer is scanned on the same scanner (intra-scanner reproducibility).

Considering overall grey matter and white matter, ADC, D, MD and FA showed an intra-scanner and inter-scanner CV ranging between 1% (ADC in white matter) and 7.4% (FA in grey matter), with a mean CV of 2.6%. The reproducibility of f was lower than for the other parameters with an average intra-scanner CV of 8.4% and inter-scanner CV of 24.8%. Similarly to the results in the phantom, it was noted that the value of f in scanner G was much higher than in the other scanners, as also seen in the boxplots in Figure 5.4 and Figure 5.5; excluding this scanner reduced the inter-scanner reproducibility to 6.9%.

The mean ADC, D and MD were 0.84, 0.75 and  $0.85 \times 10^{-3} \text{ mm}^2\text{s}^{-1}$  in grey matter and 0.7, 0.65 and  $0.7 \times 10^{-3} \text{ mm}^2\text{s}^{-1}$  in white matter, respectively. The mean value of f was 0.1 in grey matter and 0.08 in white matter. Excluding scanner G, the mean value of f was 0.093 in grey matter and 0.072 in white matter. The mean FA was 0.17 in grey matter and 0.42 in white matter.

The reproducibility of ADC, D, MD and FA was lower in the specific brain regions analysed as compared to overall grey and white matter, and the highest CV was found in the choroid plexus and the optic chiasm. The reproducibility of FA in specific white matter areas is shown in Table 5.9. The mean intra- and inter-scanner CV was 4.2% and 4.4% respectively, with a mean FA ranging from 0.43 to 0.65 depending on the areas analysed.

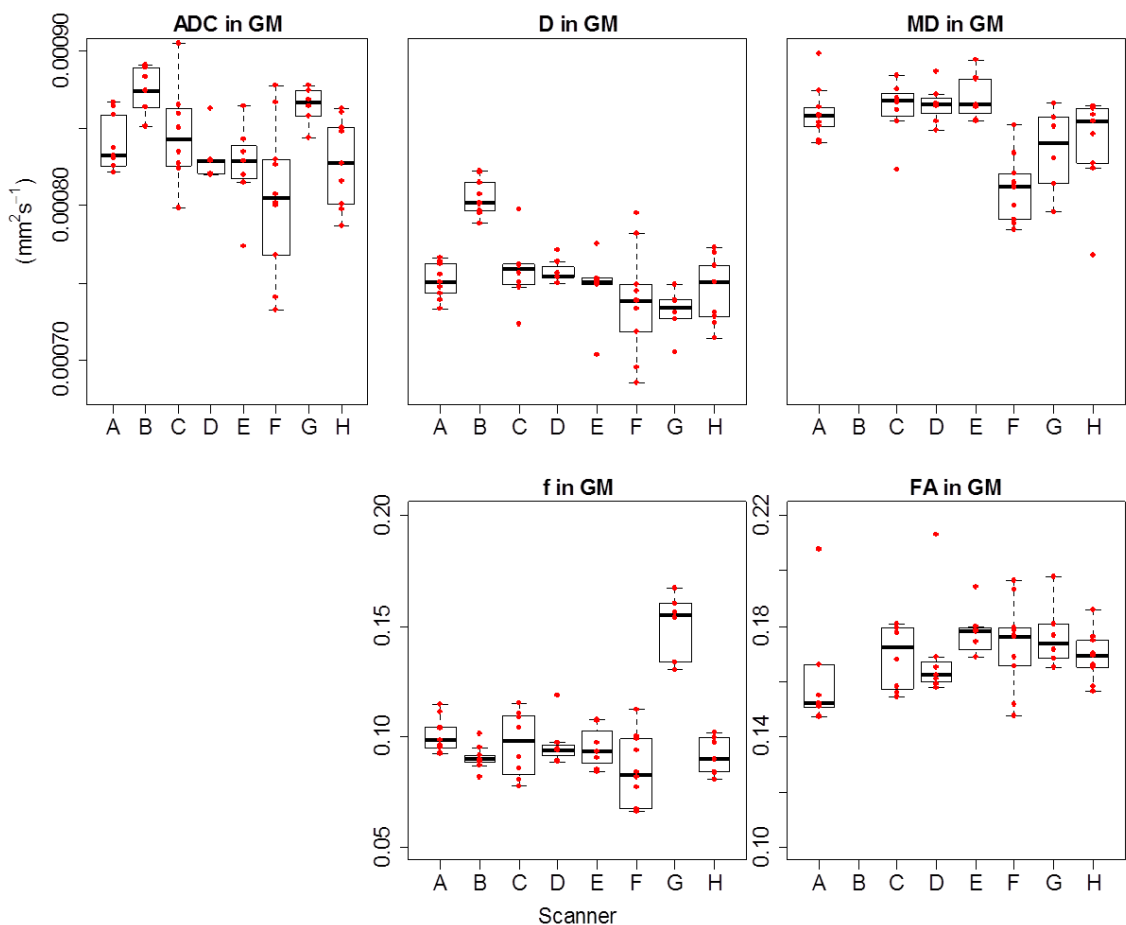


**Figure 5.4: Box plots for DWI and DTI parameters across all scanners in grey matter (GM).** ADC, D and MD are shown with the same range on the y-axis for direct comparison. A-H represent each scanner involved in the study, and the red data points represent individual subjects. ADC and MD had very similar values, while D had comparable but lower values. The boxplots confirm the higher values of f in scanner G.

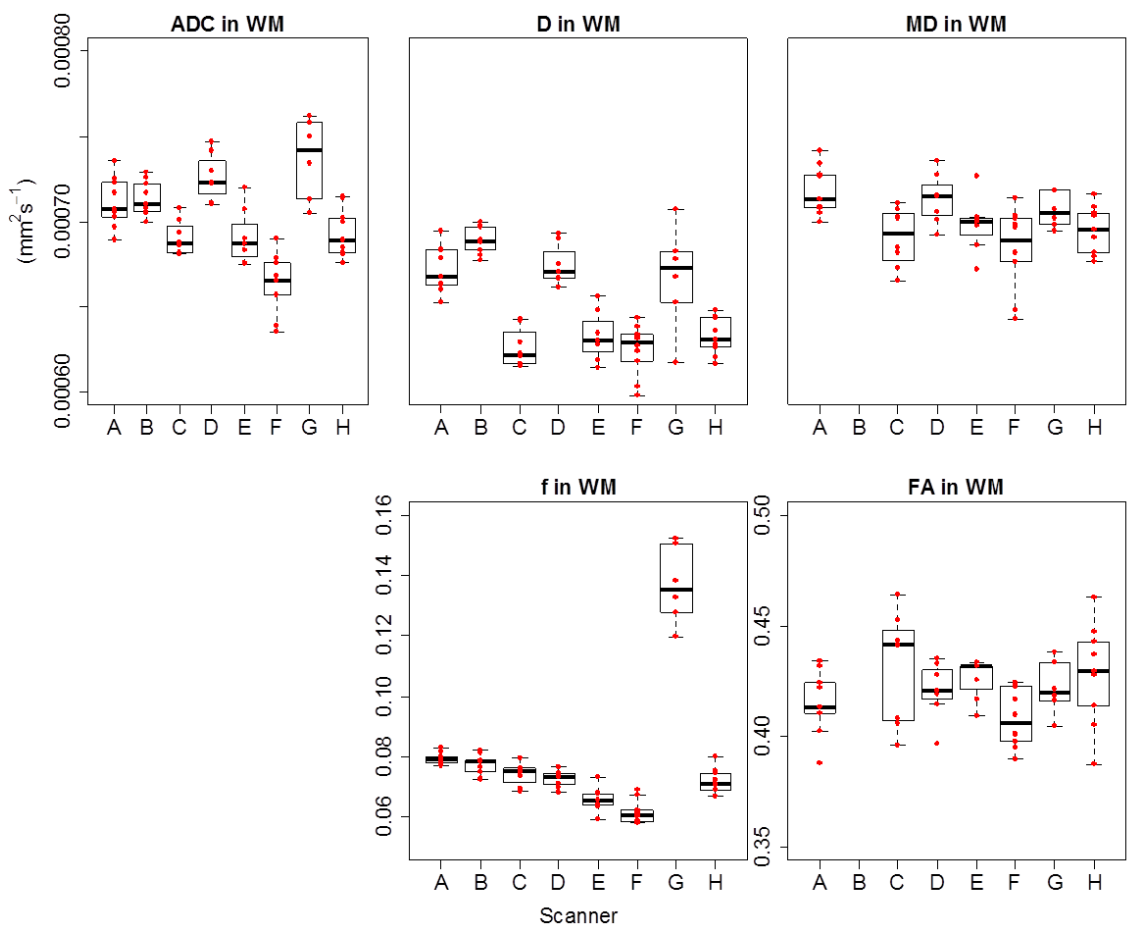


**Figure 5.5: Box plots for DWI and DTI parameters across all scanners in white matter (WM).** ADC, D and MD are shown with the same range on the y-axis for direct comparison. A-H represent each scanner involved in the study, and the red data points represent individual subjects. ADC and MD had very similar values, while D had comparable but lower values. The boxplots confirm the higher values of f in scanner G.

**Table 5.4: Reproducibility in volunteers for ADC.** The table shows the mean and standard deviation values for the measured ADC together with the associated CV in grey matter (GM) and white matter (WM) in all scans, and in eight separate regions in fifty-six of the scans. The first column gives the mean – across all scanners and volunteers as measured by the model. The second column shows the inter-scanner reproducibility – the variation expected if the same volunteer is scanned on a different scanner. The third column shows the inter-volunteer reproducibility – the variation expected if a different volunteer is scanned on the same scanner. The fourth column shows the intra-scanner reproducibility – the variation expected if the same volunteer is scanned on the same scanner. Values which are not estimated (NE) imply that the level of variation was not sufficiently large to warrant inclusion of the random effect in the analysis, as explained in the software manual in <sup>139</sup>.

Volunteers		Mean	Inter-scanner	Inter-volunteer	Intra-scanner
			(intra-volunteer)	(intra-scanner)	(intra-volunteer)
Overall	GM $\times 10^{-3} \text{ mm}^2 \text{s}^{-1}$	0.8327	$\pm 0.0203$	$\pm 0.0246$	$\pm 0.0242$
	CV		<b>2.4%</b>	<b>3.0%</b>	<b>2.9%</b>
	WM $\times 10^{-3} \text{ mm}^2 \text{s}^{-1}$	0.7010	$\pm 0.0210$	$\pm 0.0156$	$\pm 0.0072$
	CV		<b>3.0%</b>	<b>2.2%</b>	<b>1.0%</b>
Cerebellum	Cortex (GM) $\times 10^{-3} \text{ mm}^2 \text{s}^{-1}$	0.8322	$\pm 0.0914$	$\pm 0.0207$	$\pm 0.0290$
	CV		<b>11.0%</b>	<b>2.5%</b>	<b>3.5%</b>
	WM $\times 10^{-3} \text{ mm}^2 \text{s}^{-1}$	0.7244	$\pm 0.099$	$\pm 0.0137$	$\pm 0.0429$
	CV		<b>13.7%</b>	<b>1.9%</b>	<b>5.9%</b>
Brain Stem	All $\times 10^{-3} \text{ mm}^2 \text{s}^{-1}$	0.8710	$\pm 0.1240$	NE	$\pm 0.0679$
	CV		<b>14.2%</b>	NE	<b>7.8%</b>
	WM $\times 10^{-3} \text{ mm}^2 \text{s}^{-1}$	0.7346	$\pm 0.0590$	$\pm 0.0113$	$\pm 0.0190$
	CV		<b>8.0%</b>	<b>1.5%</b>	<b>2.6%</b>
Cerebrum	Basal Ganglia $\times 10^{-3} \text{ mm}^2 \text{s}^{-1}$	0.7574	$\pm 0.0590$	$\pm 0.0162$	$\pm 0.0293$
	CV		<b>10.6%</b>	<b>2.1%</b>	<b>3.9%</b>
	Thalamus $\times 10^{-3} \text{ mm}^2 \text{s}^{-1}$	0.7894	$\pm 0.0809$	$\pm 0.0200$	$\pm 0.0236$
	CV		<b>10.2%</b>	<b>2.5%</b>	<b>3.0%</b>
	Choroid Plexus $\times 10^{-3} \text{ mm}^2 \text{s}^{-1}$	1.9049	$\pm 0.5502$	$\pm 0.0920$	$\pm 0.2103$
	CV		<b>28.9%</b>	<b>4.8%</b>	<b>11.0%</b>
	Optic Chiasm $\times 10^{-3} \text{ mm}^2 \text{s}^{-1}$	1.4399	$\pm 0.3212$	$\pm 0.1618$	$\pm 0.3930$
	CV		<b>22.3%</b>	<b>11.2%</b>	<b>27.3%</b>

**Table 5.5: Reproducibility in volunteers for D.** The table shows the mean and standard deviation values for the measured D together with the associated CV in grey matter (GM) and white matter (WM) in all scans, and in eight separate regions in fifty-six of the scans. All terminology is the same as for Table 5.4.

		Volunteers		Inter-scanner Mean	Inter-volunteer (intra-volunteer)	Intra-scanner (intra-scanner)
DWI - VIM - D	Overall	GM	$\times 10^{-3} \text{ mm}^2 \text{s}^{-1}$	0.7495	$\pm 0.0207$	$\pm 0.0186$
		CV			<b>2.8%</b>	<b>2.5%</b>
	Cerebellum	WM	$\times 10^{-3} \text{ mm}^2 \text{s}^{-1}$	0.6506	$\pm 0.0249$	$\pm 0.0115$
		CV			<b>3.8%</b>	<b>1.8%</b>
	Brain Stem	Cortex (GM)	$\times 10^{-3} \text{ mm}^2 \text{s}^{-1}$	0.7283	$\pm 0.0577$	$\pm 0.0139$
		CV			<b>7.9%</b>	<b>1.9%</b>
	Cerebrum	WM	$\times 10^{-3} \text{ mm}^2 \text{s}^{-1}$	0.6491	$\pm 0.0501$	$\pm 0.0083$
		CV			<b>7.7%</b>	<b>1.3%</b>
DWI - VIM - D	All	All	$\times 10^{-3} \text{ mm}^2 \text{s}^{-1}$	0.6819	$\pm 0.0665$	NE
		CV			<b>9.8%</b>	<b>NE</b>
	Cerebellum	WM	$\times 10^{-3} \text{ mm}^2 \text{s}^{-1}$	0.7035	$\pm 0.0294$	$\pm 0.0098$
		CV			<b>4.2%</b>	<b>1.4%</b>
	Cerebrum	Basal Ganglia	$\times 10^{-3} \text{ mm}^2 \text{s}^{-1}$	0.7184	$\pm 0.0308$	$\pm 0.0145$
		CV			<b>4.3%</b>	<b>2.0%</b>
	Cerebrum	Thalamus	$\times 10^{-3} \text{ mm}^2 \text{s}^{-1}$	0.7367	$\pm 0.0040$	$\pm 0.0178$
		CV			<b>5.4%</b>	<b>2.4%</b>
DWI - VIM - D	Cerebrum	Choroid Plexus	$\times 10^{-3} \text{ mm}^2 \text{s}^{-1}$	1.8489	$\pm 0.2281$	$\pm 0.1443$
		CV			<b>12.3%</b>	<b>7.8%</b>
	Cerebrum	Optic Chiasm	$\times 10^{-3} \text{ mm}^2 \text{s}^{-1}$	0.9730	$\pm 0.0755$	$\pm 0.0962$
		CV			<b>7.8%</b>	<b>9.9%</b>
	Cerebrum					<b>28.9%</b>

**Table 5.6: Reproducibility in volunteers for f.** The table shows the mean and standard deviation values for the measured f together with the associated CV in grey matter (GM) and white matter (WM) in all scans, and in eight separate regions in fifty-six of the scans. All terminology is the same as for Table 5.4.

Volunteers		Mean	Inter-scanner (intra-volunteer)	Inter-volunteer (intra-scanner)	Intra-scanner (intra-volunteer)
Overall	GM $\times 10^{-3} \text{ mm}^2 \text{s}^{-1}$	0.1005	$\pm 0.0204$	$\pm 0.0026$	$\pm 0.0111$
	CV		<b>20.3%</b>	<b>2.6%</b>	<b>11.1%</b>
	WM $\times 10^{-3} \text{ mm}^2 \text{s}^{-1}$	0.0799	$\pm 0.0234$	$\pm 0.0020$	$\pm 0.0047$
	CV		<b>29.2%</b>	<b>2.6%</b>	<b>5.8%</b>
Cerebellum	Cortex (GM) $\times 10^{-3} \text{ mm}^2 \text{s}^{-1}$	0.1441	$\pm 0.0244$	$\pm 0.0080$	$\pm 0.0121$
	CV		<b>16.9%</b>	<b>5.6%</b>	<b>8.4%</b>
	WM $\times 10^{-3} \text{ mm}^2 \text{s}^{-1}$	0.0966	$\pm 0.0136$	$\pm 0.0046$	$\pm 0.0112$
	CV		<b>14.1%</b>	<b>4.8%</b>	<b>11.6%</b>
Brain Stem	All $\times 10^{-3} \text{ mm}^2 \text{s}^{-1}$	0.1771	$\pm 0.0249$	$\pm 0.0159$	$\pm 0.0218$
	CV		<b>14.1%</b>	<b>9.0%</b>	<b>12.3%</b>
	WM $\times 10^{-3} \text{ mm}^2 \text{s}^{-1}$	0.0832	$\pm 0.0175$	$\pm 0.0035$	$\pm 0.0060$
	CV		<b>21.1%</b>	<b>4.2%</b>	<b>7.2%</b>
Cerebrum	Basal Ganglia $\times 10^{-3} \text{ mm}^2 \text{s}^{-1}$	0.0765	$\pm 0.0197$	$\pm 0.0056$	$\pm 0.0094$
	CV		<b>25.7%</b>	<b>7.3%</b>	<b>12.3%</b>
	Thalamus $\times 10^{-3} \text{ mm}^2 \text{s}^{-1}$	0.1079	$\pm 0.0316$	$\pm 0.0041$	$\pm 0.0115$
	CV		<b>29.3%</b>	<b>3.8%</b>	<b>10.7%</b>
DWI - IVIM - f	Choroid Plexus $\times 10^{-3} \text{ mm}^2 \text{s}^{-1}$	0.2949	$\pm 0.0349$	$\pm 0.0370$	$\pm 0.0546$
	CV		<b>11.8%</b>	<b>12.6%</b>	<b>18.5%</b>
	Optic Chiasm $\times 10^{-3} \text{ mm}^2 \text{s}^{-1}$	0.4163	$\pm 0.1124$	$\pm 0.0660$	$\pm 0.1316$
	CV		<b>27.0%</b>	<b>15.8%</b>	<b>31.6%</b>

**Table 5.7: Reproducibility in volunteers for MD.** The table shows the mean and standard deviation values for the measured MD together with the associated CV in grey matter (GM) and white matter (WM) in all scans, and in eight separate regions in forty-seven of the scans. All terminology is the same as for Table 5.4.

		Volunteers	Inter-scanner		Inter-volunteer	
			Mean	(intra-volunteer)	(intra-scanner)	(intra-volunteer)
Overall	GM	$\times 10^{-3} \text{ mm}^2 \text{s}^{-1}$	0.8490	$\pm 0.0212$	$\pm 0.0080$	$\pm 0.0202$
		CV		<b>2.5%</b>	<b>0.9%</b>	<b>2.4%</b>
	WM	$\times 10^{-3} \text{ mm}^2 \text{s}^{-1}$	0.6971	$\pm 0.0111$	$\pm 0.0180$	$\pm 0.0094$
		CV		<b>1.6%</b>	<b>2.6%</b>	<b>1.3%</b>
Cerebellum	Cortex (GM)	$\times 10^{-3} \text{ mm}^2 \text{s}^{-1}$	0.8506	$\pm 0.0824$	$\pm 0.0212$	$\pm 0.0446$
		CV		<b>9.7%</b>	<b>2.5%</b>	<b>5.2%</b>
	WM	$\times 10^{-3} \text{ mm}^2 \text{s}^{-1}$	0.7209	$\pm 0.0523$	$\pm 0.0100$	$\pm 0.0393$
		CV		<b>7.3%</b>	<b>1.4%</b>	<b>5.5%</b>
DTI - MD	Brain Stem	$\times 10^{-3} \text{ mm}^2 \text{s}^{-1}$	0.9316	$\pm 0.0773$	$\pm 0.0293$	$\pm 0.0791$
		CV		<b>8.3%</b>	<b>3.1%</b>	<b>8.5%</b>
	WM	$\times 10^{-3} \text{ mm}^2 \text{s}^{-1}$	0.7851	$\pm 0.0328$	$\pm 0.0142$	$\pm 0.0236$
		CV		<b>4.2%</b>	<b>1.8%</b>	<b>3.0%</b>
Cerebrum	Basal Ganglia	$\times 10^{-3} \text{ mm}^2 \text{s}^{-1}$	0.8012	$\pm 0.0199$	$\pm 0.0150$	$\pm 0.0292$
		CV		<b>2.5%</b>	<b>1.9%</b>	<b>3.6%</b>
	Thalamus	$\times 10^{-3} \text{ mm}^2 \text{s}^{-1}$	0.8846	$\pm 0.0618$	$\pm 0.0394$	$\pm 0.0871$
		CV		<b>7.0%</b>	<b>4.5%</b>	<b>9.9%</b>
	Choroid Plexus	$\times 10^{-3} \text{ mm}^2 \text{s}^{-1}$	2.2421	$\pm 0.3140$	$\pm 0.1241$	$\pm 0.2634$
		CV		<b>14.0%</b>	<b>5.5%</b>	<b>11.7%</b>
	Optic Chiasm	$\times 10^{-3} \text{ mm}^2 \text{s}^{-1}$	1.5959	$\pm 0.2154$	$\pm 0.2592$	$\pm 0.3011$
		CV		<b>13.5%</b>	<b>16.2%</b>	<b>18.9%</b>

**Table 5.8: Reproducibility in volunteers for FA.** The table shows the mean and standard deviation values for the measured FA together with the associated CV in grey matter (GM) and white matter (WM) in all scans, and in eight separate regions in forty-seven of the scans. All terminology is the same as for Table 5.4.

		Volunteers	Inter-scanner		Inter-volunteer	Intra-scanner
			Mean	(intra-volunteer)	(intra-scanner)	(intra-volunteer)
Overall	GM	$\times 10^{-3} \text{ mm}^2 \text{s}^{-1}$	0.1726	$\pm 0.0047$	$\pm 0.0097$	$\pm 0.0128$
		CV		<b>2.7%</b>	<b>5.6%</b>	<b>7.4%</b>
	WM	$\times 10^{-3} \text{ mm}^2 \text{s}^{-1}$	0.4187	$\pm .0083$	$\pm 0.0157$	$\pm 0.0088$
		CV		<b>2.0%</b>	<b>3.8%</b>	<b>2.1%</b>
Cerebellum	Cortex (GM)	$\times 10^{-3} \text{ mm}^2 \text{s}^{-1}$	0.1991	$\pm 0.0142$	$\pm 0.0077$	$\pm 0.0201$
		CV		<b>7.1%</b>	<b>3.9%</b>	<b>10.1%</b>
	WM	$\times 10^{-3} \text{ mm}^2 \text{s}^{-1}$	0.3872	$\pm 0.0253$	$\pm 0.0204$	$\pm 0.0269$
		CV		<b>6.5%</b>	<b>5.3%</b>	<b>6.9%</b>
DTI - FA	Brain Stem	$\times 10^{-3} \text{ mm}^2 \text{s}^{-1}$	0.4139	$\pm 0.0224$	$\pm 0.0157$	$\pm 0.0243$
		CV		<b>5.4%</b>	<b>3.8%</b>	<b>5.9%</b>
	WM	$\times 10^{-3} \text{ mm}^2 \text{s}^{-1}$	0.3275	$\pm 0.0529$	$\pm 0.0102$	$\pm 0.0254$
		CV		<b>16.1%</b>	<b>3.1%</b>	<b>7.8%</b>
Cerebrum	Basal Ganglia	$\times 10^{-3} \text{ mm}^2 \text{s}^{-1}$	0.2351	$\pm 0.0373$	$\pm 0.0159$	$\pm 0.0247$
		CV		<b>15.8%</b>	<b>6.8%</b>	<b>10.5%</b>
	Thalamus	$\times 10^{-3} \text{ mm}^2 \text{s}^{-1}$	0.2879	$\pm 0.0090$	$\pm 0.0151$	$\pm 0.0220$
		CV		<b>3.1%</b>	<b>5.2%</b>	<b>7.6%</b>
	Choroid Plexus	$\times 10^{-3} \text{ mm}^2 \text{s}^{-1}$	0.1592	$\pm 0.0321$	NE	$\pm 0.042$
		CV		<b>20.1%</b>	<b>NE</b>	<b>26.4%</b>
	Optic Chiasm	$\times 10^{-3} \text{ mm}^2 \text{s}^{-1}$	0.1781	$\pm 0.0377$	NE	$\pm 0.0857$
		CV		<b>21.2%</b>	<b>NE</b>	<b>48.1%</b>

**Table 5.9: Reproducibility of FA.** The table shows the mean and standard deviation for FA as measured in each of the specified white matter areas. All terminology is the same as for Table 5.4.

	Volunteers	Mean	Inter-scanner (intra-volunteer)	Inter-volunteer (intra-scanner)	Intra-scanner (intra-volunteer)
DTI - FA	Genu of corpus callosum	0.6257	$\pm 0.0195$	$\pm 0.0226$	$\pm 0.0154$
	CV		<b>3.1%</b>	<b>3.6%</b>	<b>2.5%</b>
	Body of corpus callosum	0.5838	$\pm 0.0199$	$\pm 0.0260$	$\pm 0.0143$
	CV		<b>3.4%</b>	<b>4.4%</b>	<b>2.5%</b>
	Splenium of corpus callosum	0.6523	$\pm 0.0168$	$\pm 0.0493$	$\pm 0.0165$
	CV		<b>2.6%</b>	<b>7.6%</b>	<b>2.5%</b>
	Cerebral peduncle - right	0.5966	$\pm 0.0314$	$\pm 0.0493$	$\pm 0.0235$
	CV		<b>5.3%</b>	<b>8.3%</b>	<b>3.9%</b>
	Cerebral peduncle - left	0.6059	$\pm 0.0378$	$\pm 0.0407$	$\pm 0.0255$
	CV		<b>6.2%</b>	<b>6.7%</b>	<b>4.2%</b>
	Sagittal stratum - right	0.5091	$\pm 0.0241$	$\pm 0.0359$	$\pm 0.0168$
	CV		<b>4.7%</b>	<b>7.0%</b>	<b>3.3%</b>
	Sagittal stratum - left	0.4975	$\pm 0.0158$	$\pm 0.0379$	$\pm 0.0150$
	CV		<b>3.2%</b>	<b>7.6%</b>	<b>3.0%</b>
	Cingulum (hippocampus) - right	0.4289	$\pm 0.0266$	$\pm 0.0292$	$\pm 0.0397$
	CV		<b>6.2%</b>	<b>6.8%</b>	<b>9.2%</b>
	Cingulum (hippocampus) - left	0.4514	$\pm 0.0200$	$\pm 0.0439$	$\pm 0.0399$
	CV		<b>4.4%</b>	<b>9.7%</b>	<b>8.8%</b>
	Superior longitudinal fasciculus - right	0.4462	$\pm 0.0224$	$\pm 0.0319$	$\pm 0.0132$
	CV		<b>5.0%</b>	<b>7.1%</b>	<b>3.0%</b>
	Superior longitudinal fasciculus - left	0.4400	$\pm 0.0185$	$\pm 0.0158$	$\pm 0.0136$
	CV		<b>4.2%</b>	<b>3.6%</b>	<b>3.1%</b>

### 5.3.3 FIELD STRENGTH COMPARISON

When fitting the mixed-effect model to the 1.5T and 3T scanners separately, no consistent pattern for differences between the two field strengths was observed. Results for the CV from the two scanner field strengths are shown separately and combined in Table 5.10.

**Table 5.10: Comparison of CV in 1.5, 3T and all scanners.** The table shows the inter-scanner and the intra- scanner CV when 1.5 and 3T scanners are analysed separately for GM and WM regions, together with the reported CV when combining all scanners together. A larger difference in inter- scanner CV can be seen for f when combining data from all scanners together. No large differences in CV can be seen otherwise.

Field Strength		Inter-scanner			Intra-scanner		
		1.5T	3T	All	1.5	3	All
<b>ADC</b>	GM	1.5	1.4	2.4	2.6	3.5	2.9
	WM	1.5	1.6	3.0	1.3	0.7	1.0
<b>D</b>	GM	3.9	0.8	2.8	1.4	2.5	2.1
	WM	1.3	0.5	3.8	0.8	1.0	1.7
<b>f</b>	GM	5.5	5.6	20.3	7.5	13.9	11.1
	WM	4.1	8.0	29.2	2.3	5.4	5.8
<b>MD</b>	GM	1.9	3.0	2.5	1.9	2.5	2.4
	WM	1.2	0.5	1.6	0.9	1.4	1.3
<b>FA</b>	GM	2.9	2.5	2.7	7.2	1.6	7.4
	WM	0.9	2.6	2.0	1.6	2.0	2.1

## 5.4 Discussion

Multi-centre studies are becoming increasingly important with the discovery of new genetic biomarkers that characterise more specific and rare disease types. In such cases, patients with specific rare diseases can be grouped and studied together across centres, leading to larger sample sizes and more powerful data analyses. Furthermore, meaningful use of imaging biomarkers for treatment stratification and prognostication is dependent on robust interpretation of data from multiple centres. In order to

compare diffusion imaging across centres the reproducibility of both DWI and DTI parameters were studied.

#### 5.4.1 PHANTOM

The diffusion coefficient of water, at 0°C, in the ice-phantom is expected to be  $1.099 \times 10^{-3} \text{ mm}^2 \text{s}^{-1}$ .<sup>127</sup> In the phantom there was no perfusion and hence the perfusion fraction, f, is expected to be close to zero, and the result of noise or model fitting errors. The IVIM model is also therefore expected to have a slow diffusion coefficient, D, similar to the ADC. MD is expected to have a value comparable to the ADC (ADC was measured using DWI as an average of three directions; MD was measured from the diffusion tensor with data acquired over 15 to 60 directions). FA is expected to be close to zero due to free diffusion in the water-filled tubes and therefore its calculated value is dominated by the effects of noise and a high CV is consequently expected.

In the phantom, ADC, D and MD gave very similar results close to the expected value of  $1.099 \times 10^{-3} \text{ mm}^2 \text{s}^{-1}$  in all scanners except for scanner F, where the ice-phantom was not given sufficient time to reach thermal equilibrium. Excluding the result from this scanner gave a very good reproducibility, with a CV of <1.5% for the three parameters. The low reproducibility of FA was expected. Magnitude images have a rectified noise floor<sup>140</sup>, which leads to non-zero calculation of FA even in an isotropic medium, and hence is system dependent. Similarly, the low reproducibility of f was expected as it is a representation of both noise and over-fitting a bi-exponential to data which is in fact mono-exponential. The mean value of f was 0.02 and that of FA was 0.04. While the use of an anisotropic phantom would have been more relevant for an assessment of anisotropy, such a phantom was not available for this study. However, progress has been made in developing anisotropic phantoms such as that described in<sup>66</sup> which could be used in future multi-centre analyses of FA.

#### 5.4.2 VOLUNTEERS

##### 5.4.2.1 ADC, D and MD

In volunteers, ADC and MD are again expected to yield similar results, with D having a similar but lower value due to the IVIM calculation incorporating a perfusion

component. Furthermore, the diffusion coefficient of grey matter is expected to be higher than that of white matter<sup>141</sup>. Results confirmed this with ADC and MD giving similar results for a value of  $0.84 \times 10^{-3} \text{mm}^2\text{s}^{-1}$  and  $0.85 \times 10^{-3} \text{mm}^2\text{s}^{-1}$  in grey matter respectively, and  $0.70 \times 10^{-3} \text{mm}^2\text{s}^{-1}$  for white matter in both cases. D showed lower mean values of  $0.75 \times 10^{-3} \text{mm}^2\text{s}^{-1}$  and  $0.65 \times 10^{-3} \text{mm}^2\text{s}^{-1}$  in grey and white matter respectively. ADC, D and MD all had a good reproducibility in both white matter and grey matter with a mean CV of 2.3%.

#### *5.4.2.2 The perfusion fraction, f*

In the case of f, it is expected that the grey matter signal will have a higher volume fraction related to perfusion than white matter due to an increased vascular density. Results showed the mean values to be 0.10 and 0.08 in grey and white matter respectively, which are concordant with values found in previous literature where f in grey and white matter were found to be 0.11 and 0.076 respectively<sup>142</sup>. However, due to factors such as partial volume fractions and differences in relaxation times between grey matter, white matter and blood<sup>26,143</sup>, these values are not a direct measure of cerebral blood volume fractions (approximately 5.2% and 2.7% in grey and white matter respectively<sup>144</sup>). The significantly higher value of f in both grey and white matter compared to the ice-water phantom demonstrates that perfusion effects have a significant effect on the bi-exponential component in raw DWI data acquired *in vivo*. While the reproducibility of f was found to be low overall, excluding scanner G improved the reproducibility to a CV of 5.3% in grey matter and 8.5% in white matter. Scanner G had consistently higher f for both the phantom and volunteers. It is likely that the higher estimation of f in scanner G could be driven by the higher acquisition resolution in this scanner, as compared to the other scanners, implying a lower signal to noise ratio and, as shown in previous work, an increase in f.<sup>142</sup> In measuring SNR, scanner G, with a resolution of 192 x 192, was in fact found to have the lowest SNR at 4.4 as compared to the SNR of 15 and 12.9 in the other two Siemens Avanto scanners, both with a resolution of 128 x 128. It is thus recommended that the acquisition resolution and SNR are checked before comparing the f value for different scans.

#### 5.4.2.3 *Fractional anisotropy, FA*

FA is highest in white matter, where the presence of structured fibres contributes to the anisotropy of the diffusion of water molecules. Measured FA was higher in white matter, as expected, with a mean value of 0.42 as compared to that found in grey matter of 0.17. This further supports the use of an FA threshold of 0.2 when using tractography, which aims at following pathways within white matter<sup>145</sup>. FA had a good reproducibility, with a CV of 2% when measured over all the white matter regions and a lower mean CV of 4.3% for specific white matter tracts.

#### 5.4.2.4 *Overall reproducibility*

Overall, the inter-scanner reproducibility of ADC, D, MD and FA in grey and white matter was less than 4% in all scanners. As expected, in most cases the intra-scanner reproducibility was better than the inter-scanner reproducibility. Furthermore, analysing the two scanner field strengths separately yielded similar results between 1.5T and 3T scanners, with the overall inter-scanner CV being comparable for all parameters except for f. This implies that the error associated with using data from the different scanners analysed, both 1.5T and 3T, would have a similar impact as using data from the same scanner, and hence supports the use of ADC, D, MD and FA data from across the different scanners.

Similar results to ours were observed in <sup>68</sup> where the intra-scanner CV for MD and FA was reported to be less than 6%; in <sup>72</sup> where the inter-scanner CV was reported to be less than 3.2% in both MD and FA; and in <sup>73</sup> where the intra-scanner CV was reported to be less than 3% and the inter-scanner CV to be less than 4.1% for FA. The inter-scanner reproducibility of ADC in <sup>69</sup> was calculated from the minimum and maximum mean differences and ADC was shown to vary between 3.8 to 8.8% across both grey and white matter. That study showed a poorer reproducibility than the one calculated in this study, and could be attributed to the method used – where in <sup>69</sup> grey matter was considered by drawing an ROI around the thalamus, and white matter was considered by drawing an ROI around the bilateral frontal white matter. When analysing the thalamus separately, this study showed an inter-scanner CV of 10.2%, a result more comparable to that found in <sup>69</sup>.

#### 5.4.2.5 Analysing specific brain regions

When measuring the reproducibility of diffusion imaging parameters in specific brain regions, the reproducibility was lower than in overall grey and white matter areas. This may be due to the lower number of voxels being analysed and errors associated with the introduction of a registration step. The CV was particularly low in the choroid plexus and the optic chiasm, which may be a reflection of the small areas being studied; these areas are also surrounded by CSF, making them particularly susceptible to partial volume effect. They were included as they are known sites for paediatric brain tumours, although tumours are much larger than the structures from which they arise and may well provide more reproducible data. Partial volume is highlighted by the high value of  $f$  in these regions, as a mixed population of diffusing species increases the biexponential behaviour of the DWI signal. Excluding these regions, the maximum inter-scanner CV was 14.2%, 9.8%, 9.7% and 16.1% for ADC, D, MD and FA with a mean CV of 11.3%, 6.5%, 6.5% and 9% respectively for each of the said parameters. In addition, the lower reproducibility of FA when studied in specific regions of the brain may be due to the inherent errors which exist in using a standard brain mask and registration. Nonetheless, the CV in each of the areas studied was less than 10% with a mean CV of 4.3% for both intra- and inter-scanner differences. The lower reproducibility when analysing specific regions highlights the care which needs to be taken when involving more image processing steps such as registration, and when segmenting smaller regions.

#### 5.4.3 ADVANTAGES

While the current study showed comparable reproducibility to previous studies, it has used standard clinical sequences that had not previously been specifically matched for multi-centre studies. This allows the inclusion of previously acquired historical data, i.e. retrospective multi-centre studies. It also does not require any centre to alter their sequence parameters, which would result in specialised protocols that are different to those in routine clinical use in that centre. This is a desirable factor allowing potentially more centres to contribute data for multi-centre analyses. Furthermore, the study encompassed a range of scanners; four 1.5T and four 3T scanners. The CV can thus be

used as a way of determining the minimum diffusion parameter changes required in order to be able to correlate changes in imaging with other clinically relevant measures, such as treatment response or prognosis of specific tumour subtypes. While a change in such neurological conditions as stroke and tumours may be large enough to be analysed using different clinical sequences, other neurological disorders may show more subtle variations that may require more stringent conditions in terms of scanner and acquisition protocol variability. Thus the importance of having matching imaging parameters is also pathology dependent.

#### **5.4.4 STUDY LIMITATIONS**

The main limitation in this reproducibility study lies in the method for segmenting white matter, grey matter, and each of the different regions, which may be prone to partial volume effects, and in registration errors. In order to try and limit this as much as possible only those voxels with a probability higher than 0.95 were accepted for use as grey and white matter and segmented areas were eroded by one voxel. Also of note, previous studies have shown the maximum b-value to have an impact on the measured ADC<sup>146</sup>, however all sequences employed in this study had b-values between 0 and 1000 and hence the impact of using a different upper range of b-values was not studied here. Finally, due to practical and ethical considerations the current reproducibility study was carried out in healthy volunteers; a study in patients would ideally be conducted in order to measure the effect of the specific pathology on the imaging reproducibility.

#### **5.4.5 CONCLUSION**

Diffusion MRI measures, in particular ADC, D, MD and FA have good reproducibility across both 1.5T and 3T scanners. Quantitative research studies can benefit from incorporating multi-centre data using standard clinical sequences and protocols without any significant loss of reproducibility compared to that which would be achieved from a single scanner at a single site.

## Chapter 6 DIFFUSION IMAGING AS A PROGNOSTIC BIOMARKER

Having studied the reproducibility of diffusion imaging parameters, we can proceed to use data from across different scanners. This chapter presents research work carried out as part of this thesis on diffusion imaging as a prognostic biomarker, and uses clinical data taken from two scanners. It is an expanded and adapted version of a paper published during the course of the research and is thus a more detailed version of the paper “Survival analysis for apparent diffusion coefficient measures in children with embryonal brain tumours” published in the journal “Neuro-Oncology” in 2012<sup>99</sup>.

### 6.1 Background

As mentioned in Chapter 3, embryonal brain tumours constitute a large and important subgroup of paediatric central nervous system (CNS) tumours. They are a group of malignant tumours characterised by small round cells and high cellularity and are classified into three main groups: medulloblastoma, supratentorial primitive neuroectodermal tumours (sPNET) (also known as CNS-PNET), and atypical teratoid/rhabdoid tumours (ATRT).<sup>147–150</sup> Given their common cellular features, they share similar characteristics when analysed using diffusion-weighted imaging (DWI), a sub-modality of magnetic resonance imaging (MRI).

DWI, and more specifically, the apparent diffusion coefficient (ADC), is increasingly used in the diagnosis and treatment of various tumour types, as discussed in Chapter 4. ADC, a measure of the diffusion of water, has been found to be a good biomarker for inferring tumour cellularity.<sup>74,75,121,151</sup> Regions of increased cellularity provide barriers for diffusion, restricting water motion and thereby exhibiting a lower ADC. The ADC is also affected by intracellular space: a high nucleus to cytoplasm ratio limits the diffusion of water intracellularly and is therefore thought to contribute to a reduction in ADC.<sup>78,152</sup> In areas where diffusion is not restricted, such as in cerebrospinal fluid

(CSF), brain oedema and necrotic regions of the tumour, the ADC will have a higher value.

Non-invasive imaging biomarkers that aid in cancer treatment planning are of significant importance. Cancer imaging biomarkers based on DWI have been previously discussed from a clinical, neuroradiological and oncological perspective in order to review the current pathophysiological understanding of DWI.<sup>25</sup> Furthermore, MRI biomarkers examining the gradient change over the tumour borders have also been studied.<sup>76,97,98</sup> One such biomarker is the apparent transient coefficient (ATC) which measures the gradient change in ADC at tumour borders.<sup>76,98</sup> Previous work examined the ATC from white matter into surrounding peri-tumoural oedema (ATCO), and from the peri-tumoural oedema into the tumour core (ATCT) and compared these to survival in adults with glioblastoma multiforme.<sup>98</sup> A correlation was found between ATCT and survival in that patient group.

The purpose of this research was to identify and analyse potential biomarkers that would predict survival outcome in children with embryonal brain tumours and aid in treatment planning and decision making. The work is based on the hypothesis that ATCT correlates with survival outcome in this important and highly malignant group of paediatric brain tumours. The tumours appear very dark on ADC images due to water restriction by both intra- and extracellular components.<sup>78,152</sup> The study hypothesizes that a higher tumour cell density could be related to a lower survival and a range of ADC measures were examined for correlation with survival: minimum ADC, mean ADC, ATCT and ATCO. A lower survival rate is thus expected in patients with a lower minimum and mean ADC and a more negative value of ATCT. As ATCO is hypothesized to be related to the presence of tumour cells in the surrounding oedema, it is expected that a lower value of ATCO would imply more tumour cells are present in the oedema and thus a lower survival.

## 6.2 Method

### 6.2.1 PATIENTS

61 patients with histologically proven embryonal brain tumours and who had DWI as part of their clinical imaging between 2004 and 2011 were enrolled in a retrospective study to correlate ADC measures with survival. Three children with pineoblastomas (PNET of the pineal gland) were excluded from the study as the lack of surrounding brain parenchyma and oedema precluded measurement of ATCT. Thus a total of 58 patients (31 male, 27 female, aged 3 weeks to 14.6 years, mean 5.7 years) were analysed: 44 with infratentorial and 14 with supratentorial tumours; 40 were medulloblastoma, 9 were ATRT (5 supratentorial and 4 infratentorial) and 9 were sPNET tumours. Ethical approval was given by the local research ethics committee. Informed consent was not required as the data was obtained for clinical purposes. All data was anonymised in accordance with the data protection act.

Forty patients > 3 years old underwent surgery (31 had gross total surgical resection and 9 had partial surgical resection) and this was followed by radiotherapy and chemotherapy in 39 children. Of the remaining 18 patients < 3 years at diagnosis, 14 underwent surgery (6 had gross total surgical resection and 8 had partial surgical resection) followed by both radiotherapy and chemotherapy in 5 children and chemotherapy alone in 9 children. Palliative care was given to 1 patient > 3 years and 4 patients < 3 years.

### 6.2.2 IMAGING

Imaging data from 43 of the 58 patients was acquired on a 1.5T Siemens Magnetom Symphony MRI scanner, with a maximum magnetic field gradient strength of  $30\text{mTm}^{-1}$ . The data from the remaining 15 patients was acquired on a 1.5T Siemens Avanto scanner, with a maximum magnetic field gradient strength of  $40\text{mTm}^{-1}$ . DWI data was obtained using a diffusion-sensitized single-shot echo planar imaging sequence ( $b = 0, 500, 1000 \text{ s mm}^{-2}$ ). Diffusion gradients were applied in 3 orthogonal directions, with an image matrix of 128 by 128 and field of view of 230 by 230 mm. On the Avanto scanner, 19 slices were acquired with a 5mm thickness, 1.5mm gap and a total

sequence time of 64 seconds, with TR = 2700ms and TE = 96ms. The Symphony protocol acquired 20 slices with a 5mm thickness, 2.5mm gap and a total sequence time of 56 seconds, with TR = 3600ms and TE = 107ms.

### 6.2.3 MEASUREMENTS

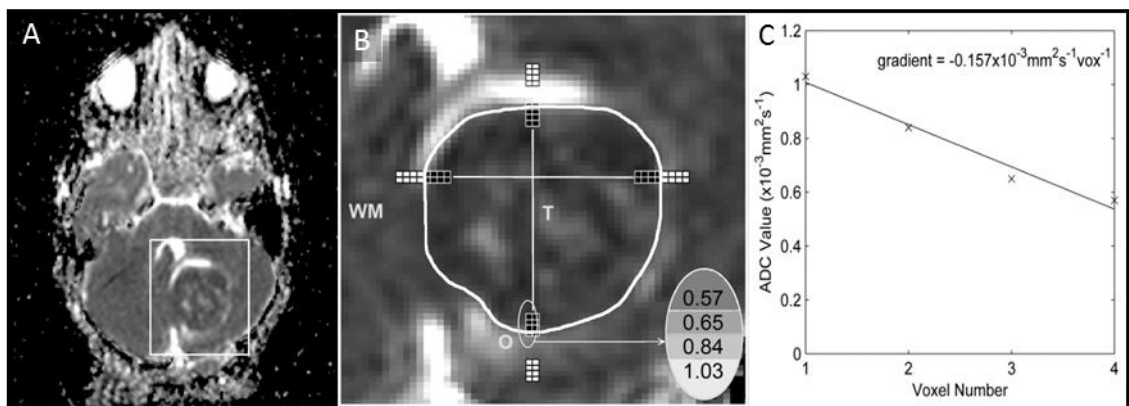


**Figure 6.1: Measuring the ATCT.** The white box in (A) indicates the area on the ADC map that is analysed. The oedema-tumour boundary is identified as marked by the white contour in (B), which also shows the white matter (WM), peri-tumoural oedema (O), and tumour core (T). The ATCT is measured at 4 different locations using a 2-voxel width as shown by the voxels highlighted in black. Therefore, ATCT is measured in a total of 8 locations. The calculation for the gradient change in ADC is shown in (C) and is performed by applying a linear fit to the circled ADC values for the vertical column of 4 pixels on the left, at the posterior side of the tumour. The gradient change in ADC is measured in all 8 locations, and the mean of these is the ATCT. In the image, voxels highlighted in white represent those voxels considered for measuring the ATCO.

Diagnostic clinical MRI scans obtained before gross total resection and prior to any chemo- and radiotherapy treatment were used for data analysis. Minimum and mean ADC were considered in the analysis and were calculated by applying a manually segmented mask, drawn on the ADC images using high-resolution T1-weighted images where necessary. The masks were drawn over the whole tumour, excluding peri-tumoural oedema but including necrotic regions of the tumour, to include the extent of necrosis in the analysis. The size of necrotic areas will influence the mean ADC as necrotic regions are expected to increase the mean ADC due to the higher ADC values in these areas.<sup>153,154</sup> Calculations for the minimum and mean ADC were carried out using MATLAB (MathWorks, Natick, MA, USA).

The apparent transient coefficient (ATC) – the gradient change in ADC over a series of voxels at the tumour border, was measured in two regions; white matter into surrounding peri-tumoural oedema (ATCO), and peri-tumoural oedema into the tumour core (ATCT). Gradients were calculated from ADC images visualised using FSLView (FMRIB Image Analysis Group, Oxford, UK) on the slice that contained the largest tumour area. The white matter-oedema boundary and the oedema-tumour boundary were identified on the selected image. Four consecutive voxels were selected: for ATCO the first voxel selected in white matter and the next three voxels in oedema; for ATCT the first voxel selected in oedema and the next three voxels in the tumour core (Figure 6.1). A linear fit for these four points was applied in order to find the gradient change in ADC. Where possible, the gradient change in ADC was calculated at four different locations of the tumour, located by drawing a crosshair through the centre of the tumour. These were averaged to determine the ATCO and ATCT used in the survival analysis. A width of two voxels was used, such that the ATCO and ATCT were averaged over eight locations. It was expected that ATCO would be a positive gradient and ATCT would be a negative gradient, as ADC values in areas of oedema are higher than both white matter and tumour areas. The ATCT was not measured in necrotic regions of the tumour.

#### 6.2.4 SURVIVAL ANALYSIS

##### 6.2.4.1 *Method description*

Survival analysis in this study consisted of a study on overall survival, and thus time to death. The major issue in conducting a survival analysis is that the event, in this case death, may not have happened by the time of last follow-up. Thus, the true survival is not known and the patient in question may have died one day later or may still be alive ten years later. In order to tackle this problem, the Kaplan-Meier survival method<sup>155</sup> was used to analyse the data and the process used to take this into consideration is known as censoring. Data points for patients who have not had the event happen at last follow-up are censored, which implies that the observation of the particular patient was cut off before the event happened.

Once the data has been obtained, survival probabilities can be constructed by considering time in small intervals<sup>156</sup>. In this way, all data can be used up until the day it is censored. The probability of surviving on day zero is equal to one and remains so up until the day at least one patient dies. The probability of surviving n days,  $S(t_n)$ , is a conditional probability and is equal to the probability of surviving (n-1) days,  $S(t_{n-1})$ , multiplied by the probability of surviving the n<sup>th</sup> day,  $S(n)$ , as shown in equation (6.1).

$$\begin{aligned} S(t_n) &= S(t_{n-1})S(n) \\ &= S(t_{n-1})\left(1 - \frac{d_n}{N_n}\right) \end{aligned} \quad (6.1)$$

where  $S(t_n)$  is the survival probability for n days;  $S(t_{n-1})$  is the survival probability for n-1 days; and  $S(n)$  is the probability of surviving on day n, which is equal to 1 – the probability of dying on day n, with  $d_n$  being the number of deaths on day n, and  $N_n$  being the number of patients known to be alive just before the deaths occurred on day n – thus excluding censored data points occurring prior to day n.

A survival curve can then be constructed from  $S(t)$ , and this curve is known as the Kaplan-Meier survival curve<sup>157</sup>. The curve only changes at times when an event occurs and patients with censored data are included up until the last day the patient was known to be alive. Once the curve is constructed, the median survival can be extracted and is equal to the number of days 50% of the patients are expected to survive. Other measures such as the 25<sup>th</sup> percentile can also be extracted and this has been calculated in this analysis to give the number of days 75% of the patients are expected to survive.

After constructing the survival curves, it may be important to conduct further statistical analysis to infer whether there is a significant difference in survival between groups. The most commonly used method and that employed in this analysis is the logrank test<sup>158</sup>. The method compares the observed number of events to the expected number of events in the scenario that there is no difference between groups and uses a  $\chi^2$  distribution to obtain a p-value.

The Kaplan-Meier survival curves and the logrank test are both univariate analyses, and thus do not take into consideration other factors which may have influenced the

results. In this study, a multivariate survival analysis was also conducted, using the Cox proportional hazard model<sup>159</sup>. This model considers the hazard ratio, the ratio between groups for the probability that a patient under observation dies in a period centred on a given time. A hazard ratio above 1 implies that the covariate is related to a decreased survival<sup>160</sup>.

#### 6.2.4.2 *Method employed*

A linear fit between survival and ATCO, ATCT, mean ADC and minimum ADC was applied to analyse whether there was any significant linear correlation. R and p values were calculated for this linear correlation.

Kaplan-Meier survival curves<sup>157</sup> were plotted for age at diagnosis (less than or greater than 3 years), extent of surgical resection (total or partial/none), tumour type (ATRT, medulloblastoma or sPNET), and whether the patient had metastasis at presentation.

Parameters showing a significant difference from the Kaplan-Meier analysis and the linear fit were included in a multivariate survival analysis<sup>160</sup>, using a Cox proportional hazard regression model. The covariates considered were: the ATCT, whether patients were aged < 3 years at diagnosis, and the extent of surgery. In order to retain significant statistical power, a maximum of three covariates were included in the multivariate survival analysis, in compliance with suggestions outlined in<sup>161</sup>.

The ATCT was further analysed by subdividing it into four groups of increasing ATCT values in such a way that an equal number of patients were included in each group, and in accordance with the approach described in<sup>162</sup>. Kaplan-Meier survival curves were constructed in order to visualise the difference in survival for the four ATCT groups. Statistical analysis was carried out using R software<sup>29</sup> and the survival analysis package therein<sup>163</sup>.

#### 6.2.5 REPRODUCIBILITY STUDY

An intra- and interobserver reproducibility study was conducted on the ATCT in a random selection of ten patients. Measurements were taken following familiarisation with the method, and intra-observer data was calculated from two measurements.

Inter-observer analysis was then carried out between a set of measurements made separately by two people. The coefficient of variation was determined in these ten patients for intra-observer and inter-observer agreement by using Bland-Altman analysis as proposed in <sup>164,165</sup>. Calculations were made using equations (6.2) and (6.3), such that the coefficient of repeatability (CR) is defined as 1.96 times the standard deviation, and the coefficient of variance (COV) is given by CR divided by the mean of the observations and expressed as a percentage. The CR indicates the limits within which 95% of observations are expected to lie.

$$CR = 1.96 \sqrt{\frac{\sum(x_1 - x_2)^2}{n - 1}} \quad (6.2)$$

where  $CR$  is the coefficient of repeatability,  $x_1$  and  $x_2$  are first and second set of measurements taken respectively, and  $n$  is the number of observations.

$$COV = \frac{CR}{mean(x_1, x_2)} \times 100\% \quad (6.3)$$

where  $COV$  is the coefficient of variance,  $CR$  is the coefficient of repeatability, and  $x_1$  and  $x_2$  are first and second set of measurements taken respectively.

### 6.3 Results

#### 6.3.1 CORRELATING ADC MEASURES WITH SURVIVAL

A plot of survival against ATCT (the gradient change in ADC from oedema into the tumour) showed that those patients who died (21/58) had more negative ATCT values than those who survived (Figure 6.2A). The linear correlation between survival and ATCT was tested and showed a statistically significant correlation ( $R = 0.49$ ,  $p < 0.001$ ). It is clear from the plot that there is a wide spread in survival, particularly as ATCT approaches zero; however, the data indicates a decreased chance of survival for highly negative values of ATCT.

A linear correlation between survival and ATCO, mean ADC and minimum ADC was not found to be statistically significant ( $p = 0.17$ ,  $0.37$  and  $0.70$  respectively) (Figure 6.2B, C, D).

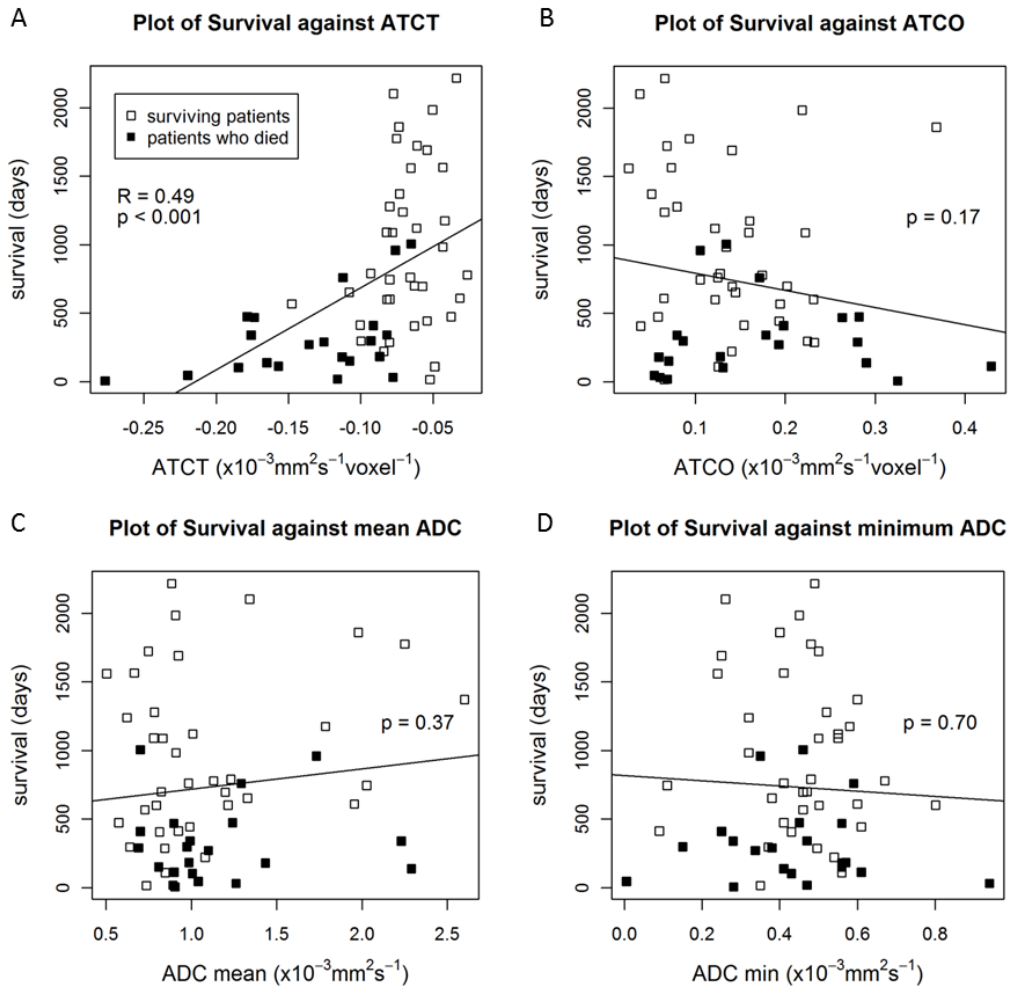


**Figure 6.2: Plot of survival against ATCT (A), ATCO (B), mean ADC (C) and minimum ADC (D) in 58 patients.** Patients who died are marked by a black box and can be seen to have a more negative ATCT value in (A). A statistically significant linear fit to the data was observed for ATCT ( $R = 0.49$ ,  $p < 0.001$ ). No significant correlation between survival and ATCO, mean ADC and minimum ADC was observed ( $p = 0.17$ ,  $0.37$  and  $0.70$  respectively).

### 6.3.2 KAPLAN-MEIER CURVES

Kaplan-Meier curves showed a statistically significant survival benefit in those children  $> 3$  years at diagnosis compared to those  $< 3$  years at diagnosis ( $p < 0.001$ ) (Figure 6.3A) and in those children who had total surgical resection ( $p = 0.04$ ) (Figure 6.3B). There was a trend for a difference in survival between ATRT, sPNET and medulloblastoma (Figure 6.3C), with the poorest survival in ATRT, followed by sPNET and then medulloblastoma, but this did not reach statistical significance ( $p = 0.09$ ).

Patients with metastasis at presentation appeared to have a poorer survival outcome, however this was not found to be statistically significant ( $p = 0.59$ ) (Figure 6.3D).

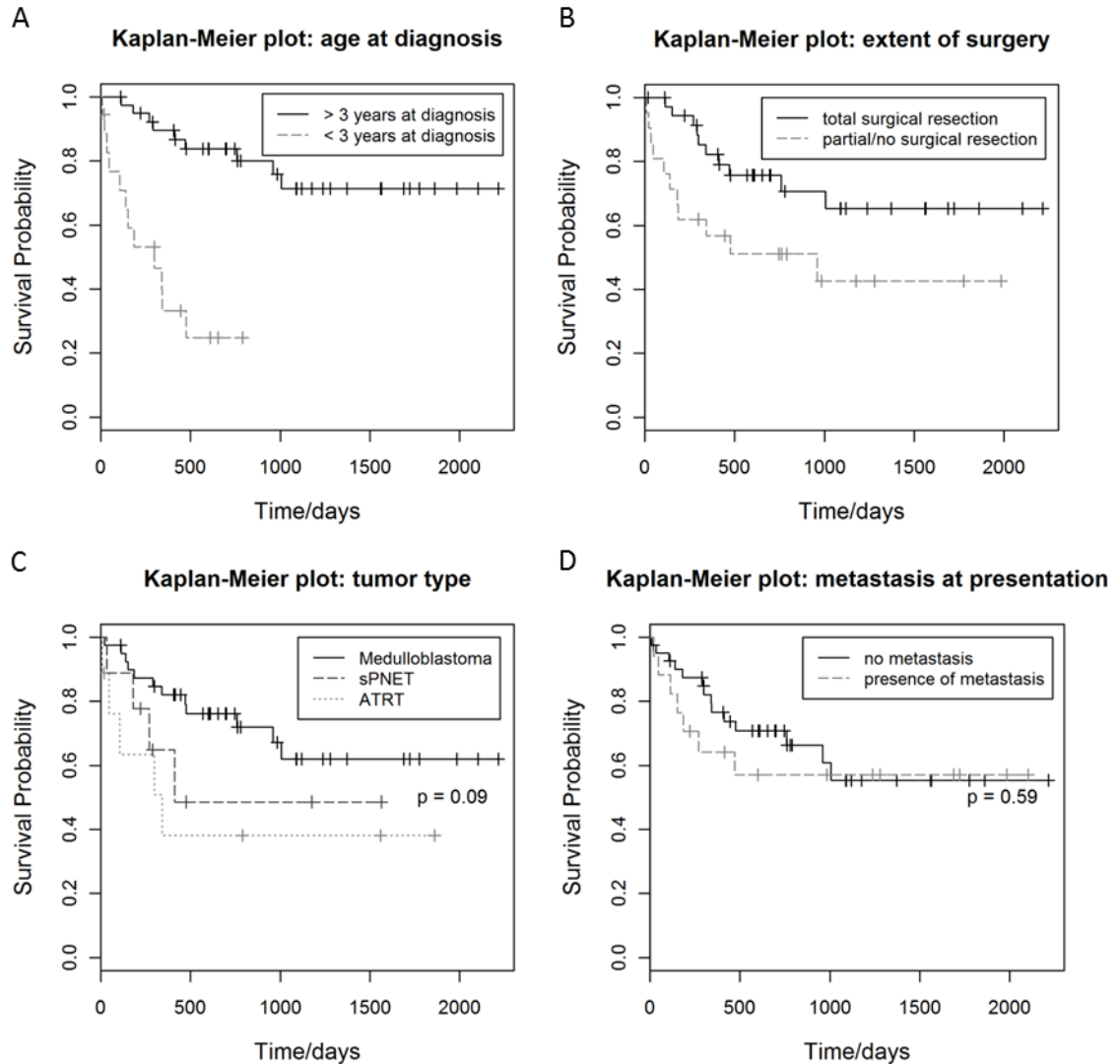


**Figure 6.3: Kaplan-Meier survival curves for age at diagnosis (A), extent of surgery (B), tumour type (C), and metastasis at presentation (D).** Children < 3 years are known to have a poorer prognosis as confirmed by the survival curves, and a statistically significant  $p$ -value of less than 0.001. Children having had total surgical resection have a statistically significant higher chance of survival ( $p = 0.04$ ). Tumour type and metastasis at presentation were not found to be statistically significant ( $p = 0.09$ ,  $p = 0.59$  respectively).

### 6.3.3 MULTIVARIATE SURVIVAL ANALYSIS

The Cox proportional hazard regression model indicated that the only statistically significant covariate was ATCT ( $p << 0.001$ ). Age < 3 years at diagnosis and extent of

surgical resection were not found to be statistically significant covariates for the analysis ( $p = 0.17$  and  $0.62$  respectively).

#### 6.3.4 ATCT KAPLAN-MEIER CURVES

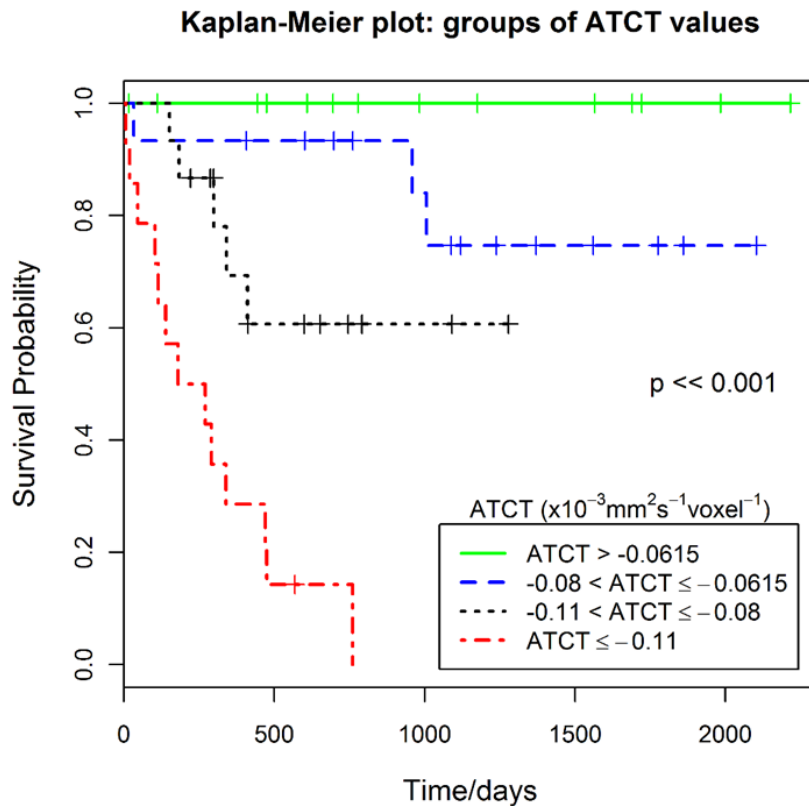


**Figure 6.4:** Kaplan-Meier survival curves for increasingly negative values of ATCT. The survival curves show a decreasing survival probability ( $p << 0.001$ ).

ATCT was the only covariate yielding high statistical significance, and survival analysis using Kaplan-Meier curves was conducted by dividing the patients into four groups of equal size and increasing values of ATCT. The result showed that more negative values of ATCT were related to a lower chance of survival ( $p << 0.001$ ). Kaplan-Meier curves show how survival differs in children with embryonal brain tumours as the value in ATCT changes (Figure 6.4). Table 6.1 shows details of the survival outcome for the four different ATCT groups together with the median survival and the 25<sup>th</sup> centile. Lower values of median survival and 25<sup>th</sup> centile indicate a lower chance of survival and were identified in the groups with more negative ATCT values. Median survival and the 25<sup>th</sup>

centile could not be measured in the less negative ATCT groups as the survival probability was higher than 50% and 75% respectively, for the duration of the study.

**Table 6.1: Survival details for increasingly negative values of ATCT.** The table shows an increased number of deaths for more negative values of ATCT. The median survival gives the probable number of days 50% of the patients would survive in each group. The 25th centile gives the probable number of days 75% of the patients would survive in each group. Median survival and the 25th centile could not be measured in the less negative ATCT groups as the survival probability was higher than 50% and 75% respectively, for the duration of the study. Likelihood of survival is higher in the patients having less negative ATCT values.

ATCT range ( $\times 10^{-3} \text{mm}^2 \text{s}^{-1} \text{vox}^{-1}$ )	- $(0 - 0.0615)$	- $(0.0615 - 0.08)$	- $(0.08 - 0.11)$	- $(0.11 - 0.3)$	Overall
	Least negative		Most negative		
no. of deaths/no. of patients	0/14	3/15	5/15	13/14	21/58
median survival (days)	N/A	N/A	N/A	226	N/A
25 <sup>th</sup> centile (days)	N/A	1006	342	104	299
< 3 years (deaths/total)	0/3	1/1	4/7	7/7	12/18
partial/no resection (deaths/total)	0/4	2/4	2/6	7/7	11/21

### 6.3.5 REPRODUCIBILITY STUDY

Bland-Altman analysis gives an indication of the variability between two measurements by plotting the difference between two repeated measurements against the mean of those two measurements. The CR for the intra- and interobserver analysis was found to be 0.0289 and  $0.0238 \times 10^{-3} \text{mm}^2 \text{s}^{-1} \text{vox}^{-1}$  respectively, whilst the COV was found to be 30.1 and 28.4% respectively. In terms of the grouping in ATCT used in building the ATCT Kaplan-Meier survival curves, 7/10 patients and 8/10 patients remained in the same group for the intra- and the interobserver analysis respectively. Of those patients changing group, 4 were to an adjacent group and 1 was a change of two groups, while both patients who died stayed within the two most negative groups and both surviving patients moved to the least negative group. Overall, all patients who died fell in the two most negative groups and the ones who

survived fell within the two least negative groups for both the intra- and the inter-observer analysis.

## 6.4 Discussion

The main finding of this study is that a statistically significant difference was observed for survival data in children with embryonal brain tumours with respect to the change in ADC from peri-tumoural oedema into the tumour volume. Results show that more negative ATCT values are significantly associated with a poorer survival rate in children with embryonal brain tumours irrespective of tumour type, extent of resection, age under 3 years at diagnosis and metastasis at presentation. We hypothesized that an increased gradient change in ADC at tumour boundaries is related to a more malignant histological tumour type, hence explaining the lower survival outcome identified in this study.

### 6.4.1 ATCT

ADC has been shown to correlate with tumour cellularity in various tumour types. One study has shown a significant correlation between ADC values and tumour cellularity in medulloblastoma.<sup>77</sup> ATCT, and thus the change in ADC over the oedema-tumour boundary, could be an indication of how rapidly the tumour cellularity is increasing (Figure 6.5A, D) and that a more rapid increase in tumour cellularity from the oedema-tumour boundary into the tumour is an indication of a poorer prognosis and reduced survival. More negative ATCT values could also be due to higher ADC values in the oedema itself, indicating that cellularity might not be the only cause for poorer prognosis (Figure 6.5B, C). Previous studies focussed on tumour border MRI features and histology have shown that a sharper border on T<sub>1</sub>- and T<sub>2</sub>- weighted imaging could be indicative of an intact 1p/19q genotype which is related to reduced survival in oligodendroglial tumours.<sup>166,167</sup> The results reported here support the hypothesis that tumour border biomarkers are useful indicators of survival in childhood embryonal brain tumours.

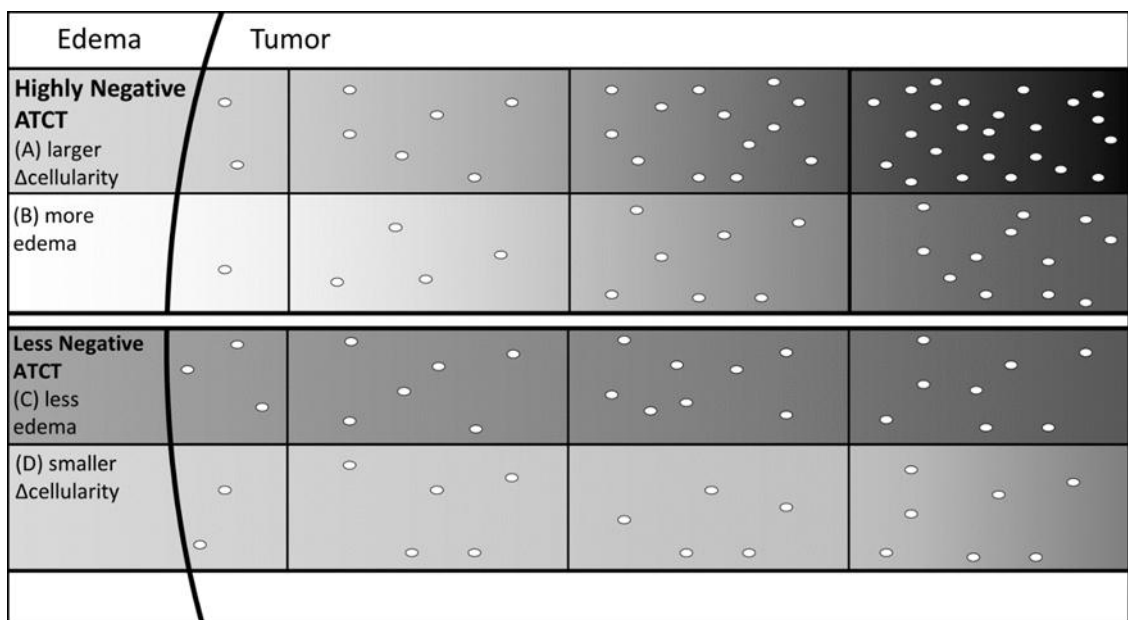


**Figure 6.5: Visualising the ATCT.** The image visualises the hypothetical difference between a highly negative value of ATCT (A, B) and a less negative value of ATCT (C, D). A highly negative value of ATCT means that there is an increased change in ADC from the first voxel on the oedema-tumour boundary towards the tumour core. This could be related to either a larger change in cellularity from the first voxel towards the tumour core (A) or due to increased oedema in the first voxel (B). The increasingly darker shades of grey represent the decreasing values of ADC as tumour cellularity inside the corresponding voxel increases. Conversely, the less negative value of ATCT could be due to less oedema being present (C) or due to a smaller change in cellularity from the first voxel towards the tumour core (D).

#### 6.4.2 ATCO, MEAN AND MINIMUM ADC

The change in ADC from white matter into oedema (the ATCO) was not found to correlate with survival. This result is consistent with previous findings showing that ATCO was not a good biomarker for survival outcome in adults with the highly malignant tumour glioblastoma multiforme.<sup>98</sup> Furthermore, in this cohort, mean ADC and minimum ADC values did not correlate with survival.

#### 6.4.3 TUMOUR TYPE

Previous studies have shown that patients with sPNET have a poorer prognosis than patients with medulloblastoma<sup>168</sup>, and patients with ATRT have a poorer prognosis than patients with either medullublastoma or sPNET<sup>169</sup>. In this analysis these differences did not reach statistical significance, however, the observed trends in the

data (Figure 6.3C) are in line with current literature, showing patients with ATRT to have the poorest prognosis and patients with medulloblastoma to have the best prognosis. The lack of statistical significance is likely to be due to the small number of sPNET and ATRT patients in this cohort, reflecting the rarity of these tumour types. However, when comparing pairs of tumour types, medulloblastoma was found to have statistically significant better survival than ATRT ( $p = 0.04$ ) in agreement with previous literature<sup>169</sup>, whilst the trend for sPNETs to fare worse than medulloblastoma did not reach statistical significance ( $p = 0.22$ ).

#### **6.4.4 METASTASIS AT PRESENTATION**

Metastatic medulloblastoma<sup>170</sup> and metastatic ATRT<sup>171</sup> are well recognised to have reduced survival rates compared to their non-metastatic counterparts. Conflicting results have been obtained in patients with sPNET, with some studies finding no correlation between survival and metastasis at presentation.<sup>53</sup> The results from this study did not show a statistically significant difference in survival for patients with metastasis at presentation across the three tumour types. However, a trend for a poorer prognosis for those patients with metastasis can be seen in Figure 6.3D. Again, the lack of statistical significance is likely to be due to the smaller sample size in this cohort when compared to the previous studies mentioned, which showed a difference in survival between patients with and without metastasis at presentation (119 patients in the study on medulloblastoma<sup>170</sup> and 48 patients in the study on ATRT<sup>171</sup>).

#### **6.4.5 ATCT ACROSS EMBRYONAL BRAIN TUMOURS**

The sample of tumours in this cohort included medulloblastoma, sPNET and ATRT. It has been shown that parameters derived from ADC histogram measures can discriminate between ATRT and both sPNET and medulloblastoma.<sup>86</sup> It is important to establish that the ATCT can be applied generally across different types of embryonal tumours, broadening its clinical utility. However, the correlation between ATCT and survival in the medulloblastoma group alone was examined and, similarly to the findings in the entire cohort, ATCT was found to strongly correlated with survival in this group ( $p < 0.001$ ). The relatively small sample sizes in the sPNET and ATRT groups

precluded a meaningful correlation of ATCT and survival in those groups if studied separately.

When looking at the survival analysis for the three embryonal tumour types, findings, taken together, demonstrated that the ATCT is a more sensitive biomarker of survival than age less than 3 years at diagnosis, extent of surgery, tumour type and metastasis at presentation. The tumour types included in this sample reflect the typical presentation of embryonal tumours such that the ATCT can be generalised across these tumour types.

#### **6.4.6 STATISTICAL ANALYSIS**

In the method a description of how a maximum of three covariates could be included in the multivariate analysis in order to retain sufficient statistical power is given. All variables were initially tested in a univariate analysis. Three covariates were found to be significant in the univariate analysis and all of these were included in the multivariate analysis. Hence, there was no reason for including more covariates even if the method and numbers allowed us to do so.

Furthermore, in conducting Kaplan-Meier survival analysis and in order to visualise the findings, ATCT was categorised into four groups. Having ATCT divided into four equal groups provided for an analysis with 3 different cut-off points and as can be seen in the Kaplan-Meier curves, there does not appear to be a single cut-off point which determines favourable or unfavourable survival outcome. Results show that the more negative the cut-off point used, the worse the survival probability.

#### **6.4.7 STUDY LIMITATIONS**

This study is limited by various factors. ATCT is a subjective measurement as oedema and tumour boundaries are identified by visual inspection, and a maximum of four locations on the tumour borders were used in the calculation of the ATCT. This limitation is reflected in the reproducibility of the method. Semi-automated methods for voxel selection for the ATCT may improve the robustness of the method and could be a fruitful avenue for future work. Given the data was collected over a period of 7 years, some patients would have received different treatment regimes, with palliative

care being offered in five cases. These different treatment procedures might have also had an impact on the survival outcome in this cohort.

Although the intra- and interobserver COV for the ATCT was found to be 30.1% and 28.4% respectively, the changes had a negligible impact on the overall results. The tendency for patients who died to fall under the two most negative groups and for the surviving patients to fall under the two least negative groups was maintained in all 10 cases analysed for both the intra- and the interobserver analysis.

Medulloblastomas are classified into four different histological subgroups (medulloblastoma with extensive nodularity, desmoplastic/nodular, anaplastic and large cell medulloblastoma)<sup>149</sup> and recent advances in molecular genetics have indicated that medulloblastomas can be further classified into four different molecular subgroups (Wnt, Shh, group 3 and group 4)<sup>172</sup>. However, these histological and molecular classifications had only been collected very recently and were not available for the majority of the cohort. Nonetheless, future studies could examine the ATCT in these distinct histological and molecular tumour types to evaluate the value of the ATCT as a biomarker in comparison to the predictive value of these classifications on survival.

As discussed in<sup>173</sup>, the patient cohort in this group was a heterogeneous one. As a limitation, heterogeneity is expected to mask the effects of interest and hence, for example, the lower survival in medulloblastoma patients having metastases at presentation could have been masked by including other tumour types such as the supratentorial primitive neuroectodermal tumours, where conflicting evidence exists as to whether there is a relationship between metastasis at presentation and survival. In a similar way, it would be expected that the relationship between survival and ATCT would be masked by cohort heterogeneity, if it is dependent on tumour type. Therefore, the fact that ATCT was significant across embryonal tumour types makes a strong case for it to be considered as a measure of prognosis in addition to currently used variables. Although different tumour subtypes have different prognoses, ATCT can still be a useful indicator of longer survival across all of them. Since there was no

evidence in the data to suggest that patients with one or another tumour type did not fit the general pattern, the results may be said to broadly apply in all cases. By contrast, restricting the analysis to a very homogeneous sample would severely restrict the generalizability of the conclusions that can be drawn. Therefore, cohort heterogeneity reinforces the strength of ATCT as a biomarker of survival across a range of embryonal tumour types. Nonetheless, further analysis on larger patient groups of a more homogeneous nature would aid in identifying those groups in which it would be most beneficial to incorporate ATCT as part of clinical trials and as a biomarker of survival.

## 6.5 Conclusion

In conclusion, identifying non-invasive biomarkers of survival outcome is of utmost importance in managing and planning the treatment of children with brain tumours. Results showed that ATCT measured at diagnosis is a sensitive biomarker that correlates with survival in childhood embryonal brain tumours. While prognostic biomarkers are useful in the initial steps of treatment planning, treatment management needs to be consolidated through the use of biomarkers of treatment response.

## Chapter 7 DIFFUSION IMAGING FOR TREATMENT RESPONSE

Biomarkers of treatment response are an essential tool for managing the treatment plan of patients. This chapter presents research work carried out as part of this thesis on diffusion imaging for treatment response. It is an adapted version of a paper published during the course of the research and titled “Challenges for the functional diffusion map in pediatric brain tumors” in the journal “Neuro-Oncology” in 2014<sup>124</sup>.

### 7.1 Background

As has already been mentioned in Chapter 3, brain tumours are the most common solid tumour in children and differ in biology and development from adult brain tumours. However, few biological markers have been studied in paediatric brain tumours compared to those carried out in adults due to the relative rarity of childhood tumours. As a consequence limited literature is available and this includes low patient numbers, who receive diverse treatment regimens.<sup>174,175</sup> Chapter 4 has introduced diffusion weighted imaging (DWI) as a tool for tumour diagnosis<sup>86</sup> whilst Chapter 6 has shown its use as a biomarker of prognosis<sup>99</sup> in childhood brain tumours. This chapter looks at DWI as a biomarker of treatment response.

The concept of measuring the diffusion of water molecules in tissue, and quantifying this in terms of the apparent diffusion coefficient (ADC) has already been introduced. Through this, DWI is able to image cellularity as a consequence of water diffusion restriction in more densely packed tumours.<sup>74</sup> The functional diffusion map (fDM), which is also known as the parametric response map, compares ADC changes over time and has been introduced in Chapter 4. In the fDM, a voxel-wise comparison of pre- and post-treatment ADC maps is carried out in the tumour areas, and the difference in ADC labelled in blue, green or red depending on whether a decrease, no change or an increase in ADC, respectively, was observed. In published studies, an increase in ADC is said to reflect a decrease in tumour cellularity and a good treatment

response. On the other hand, a decrease in ADC is said to reflect an increase in tumour cellularity and a poor treatment response.

Currently tumour size is the conventional measure of tumour response to treatment. The fDM has been proposed as a tool to monitor early treatment response and efficacy, in an attempt to identify patients that will benefit from further adjuvant therapy prior to a change in tumour size.<sup>118,119,121</sup> This study examines three factors identified as possible confounders for the fDM in childhood brain tumours; and hypothesizes that necrosis, tumour grade and change in tumour size need to be taken into consideration when interpreting fDM analysis in childhood brain tumours.

Firstly, tumour necrosis can be seen following both tumour growth, as the tumour outgrows its blood supply, as well as a result of successful treatment. Limited literature is found that links areas of necrosis to survival. One study in osteosarcoma patients, showed no correlation between 90% necrosis and survival, and suggested that more data was necessary to determine a possible correlation between 70% necrosis and survival.<sup>176</sup> In an earlier study carried out in children with brain stem gliomas treated with radiotherapy, no association was found between the absence or presence of necrosis post-radiation and outcome.<sup>177</sup> Furthermore, the presence or absence of necrosis as a prognostic factor is dependent on the disease type in which it occurs. It is currently being debated whether the inflammation in necrotic areas carries a good prognosis or not<sup>178</sup> as it is possible that a certain degree of necrosis may induce angiogenesis through the immune inflammatory cells which necrotic cell death promotes<sup>40</sup>. This study thus aimed to analyse whether the fDM in necrotic areas discriminated between the treatment outcomes.

Secondly, tumour cellularity varies by tumour type and grade and the fDM technique was applied to tumours of varying grades to establish its utility throughout a range of childhood tumours.

Thirdly, some tumours change considerably in size after treatment. Since this may cause problems of registration, the aim was to identify whether the fDM can be successfully applied in these cases.

## 7.2 Method

Thirty-four childhood brain tumour patients (19 male, 15 female; aged 4 months to 16.5 years; mean 7.8 years) who had DWI as part of their clinical imaging between 2005 and 2012, were enrolled in a retrospective study. Ethical approval was given by the local ethics committee. Informed consent was not required for imaging data as this was obtained for clinical purposes. Informed consent was obtained in those cases where the histology of patients was used. All data was made anonymous in accordance with the Data Protection Act.

Patients were selected so that fDM characteristics could be evaluated across a range of tumour types and grade. The cases that were chosen were those that had clinical DWI data available at two time-points, with a significant tumour volume at presentation and no surgery taking place in between the two time-points (which would obviate a meaningful assessment of the fDM). Of the thirty-four patients, 18 were diagnosed with diffuse intrinsic pontine glioma (DIPG), 6 with optic pathway glioma (OPG), 4 with tuberous sclerosis and sub-ependymal giant cell astrocytoma (SEGA), 3 with glioblastoma multiforme (GBM) and 3 with gliomatosis cerebri (GC). Histological diagnosis was confirmed in 4 SEGA patients, 3 GBM patients, 2 GC patients and 1 OPG patient. In the remainder, the diagnosis was made on neuroradiological grounds with imaging discussed in a multi-disciplinary team setting and accepted as a basis for treatment. The diagnostic histology was reviewed in two patients (one GBM and one OPG). This was then compared to that from a patient showing normal appearing white matter.

### 7.2.1 IMAGE ACQUISITION

Imaging data was acquired on a 1.5T Siemens Magnetom Symphony MRI scanner, with a maximum magnetic field gradient strength of  $30\text{mTm}^{-1}$  and on a 1.5T Siemens Avanto scanner, with a maximum magnetic field gradient strength of  $40\text{mTm}^{-1}$ . DWI data was obtained using a diffusion-sensitized single-shot echo planar imaging sequence ( $b = 0, 500, 1000 \text{ s mm}^{-2}$ ). The clinical ADC, using all three b-values was used in this analysis. Diffusion gradients were applied in 3 orthogonal directions, with an

image matrix of 128 by 128 and field of view of 230 by 230mm. On the Avanto scanner, 19 slices were acquired with a 5mm thickness, 1.5mm gap and a total sequence time of 64 seconds, with TR = 2700ms and TE = 96ms. The Symphony protocol acquired 20 slices with a 5mm thickness, 2.5mm gap and a total sequence time of 56 seconds, with TR = 3600ms and TE = 107ms.

### 7.2.2 fDM ANALYSIS

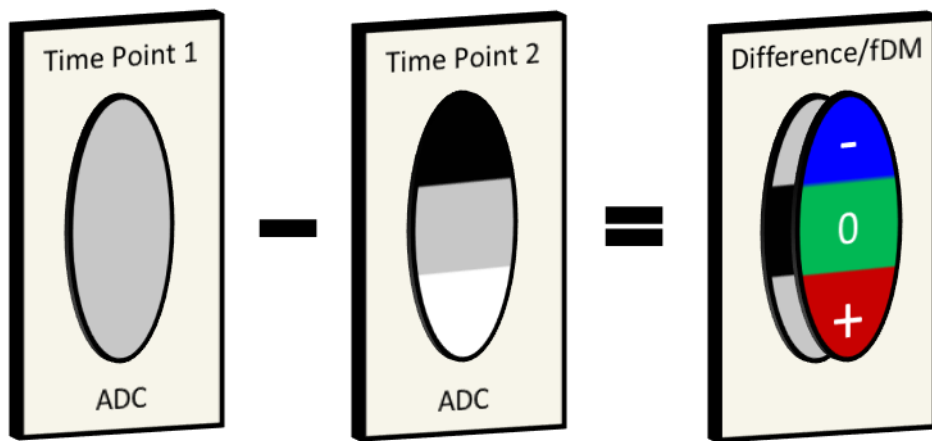


**Figure 7.1: Construction of the fDM.** The fDM is built by using tumour images at two time points. After registration of the two images, a difference image is calculated. A decrease in ADC is labelled in blue, an increase in ADC labelled in red and no change in ADC labelled in green.

Figure 7.1 shows how the fDM is constructed. Prior to building the fDM, ADC maps at the time-points analysed were co-registered to the patient's T2- weighted image at diagnosis or post-surgery to exclude major changes in the tumour due to surgery. Where pre-treatment images were not available, as some patients would have arrived at our institution with these images already taken, two post-treatment images were used. MATLAB (MathWorks) and SPM8<sup>23</sup> were used for co-registration, applying the standard normalised mutual information and a trilinear interpolation algorithm. A visual inspection was carried out on all co-registered images to ensure successful registration.

The fDM, implemented in MATLAB, was applied in tumour areas by specifying a region of interest (ROI) using FSLView (FMRIB). ROIs were defined across all tumour image slices by considering both ADC and T2-weighted images; including tumour regions and

areas of necrosis, but excluding peri-tumoural oedema where possible. The tumour boundary was identified using both ADC and T2 weighted images. Areas of bright ADC outside the defined tumour boundary were considered to be peri-tumoural oedema and thus were excluded. Infiltrative oedema was included in the analysis as it cannot be easily differentiated from tumour using ADC and T2 weighted imaging.

A voxel-wise comparison was carried out, over the whole tumour, on the two time-points being investigated. Specific thresholds were used to determine whether there was an increase, decrease or no change in ADC when comparing ADC images. This study employed the suggested threshold of  $0.40 \times 10^{-3} \text{ mm}^2\text{s}^{-1}$ , the threshold indicating the highest sensitivity and specificity in the receiver operating characteristic (ROC) analysis<sup>121</sup>. This means that a voxel with ADC increasing by more than this value is classified as increasing in ADC and displayed in red in the fDM. A voxel with ADC decreasing by more than this threshold is classified as decreasing in ADC and displayed in blue. Any voxels with an ADC change between these thresholds are classified as not changing in ADC, and are displayed in green. fDM findings are compared to clinical imaging reports in order to identify whether the fDM correctly identifies tumour response from tumour progression as reported by the clinical Radiologist.

### 7.2.3 AREAS OF NECROSIS

In the course of showing the biological processes involved in the fDM, Moffat et al. have briefly mentioned that necrotic or cystic regions can undergo a displacement of water which results in a reduction in ADC as tumour cells move into the area.<sup>118</sup> Moreover, in theory, areas of necrosis can increase or decrease in size irrespective of treatment outcome. Figure 7.2 shows a flow map for the different possible outcomes of treatment response in terms of necrotic areas within the tumour.

The fDM was studied in areas of necrosis in patients with DIPG and with GC as these were the patients which showed most necrosis as compared to the other groups studied. Areas of necrosis were identified in each image as those voxels with an ADC value higher than  $1.8 \times 10^{-3} \text{ mm}^2\text{s}^{-1}$  – a value observed to make up most of the necrotic regions on the ADC image whilst excluding both normal and tumour tissue, as well as

being the value for the mean ADC in areas of necrosis measured in other tumour types<sup>154,179</sup>. The ROI was selected such that only tumour areas visible on both pre- and post-treatment images were included in the analysis. A comparison was made between fDM tumour treatment response classification when including and excluding necrosis to test the hypothesis that necrotic areas act as a confounder in the fDM.

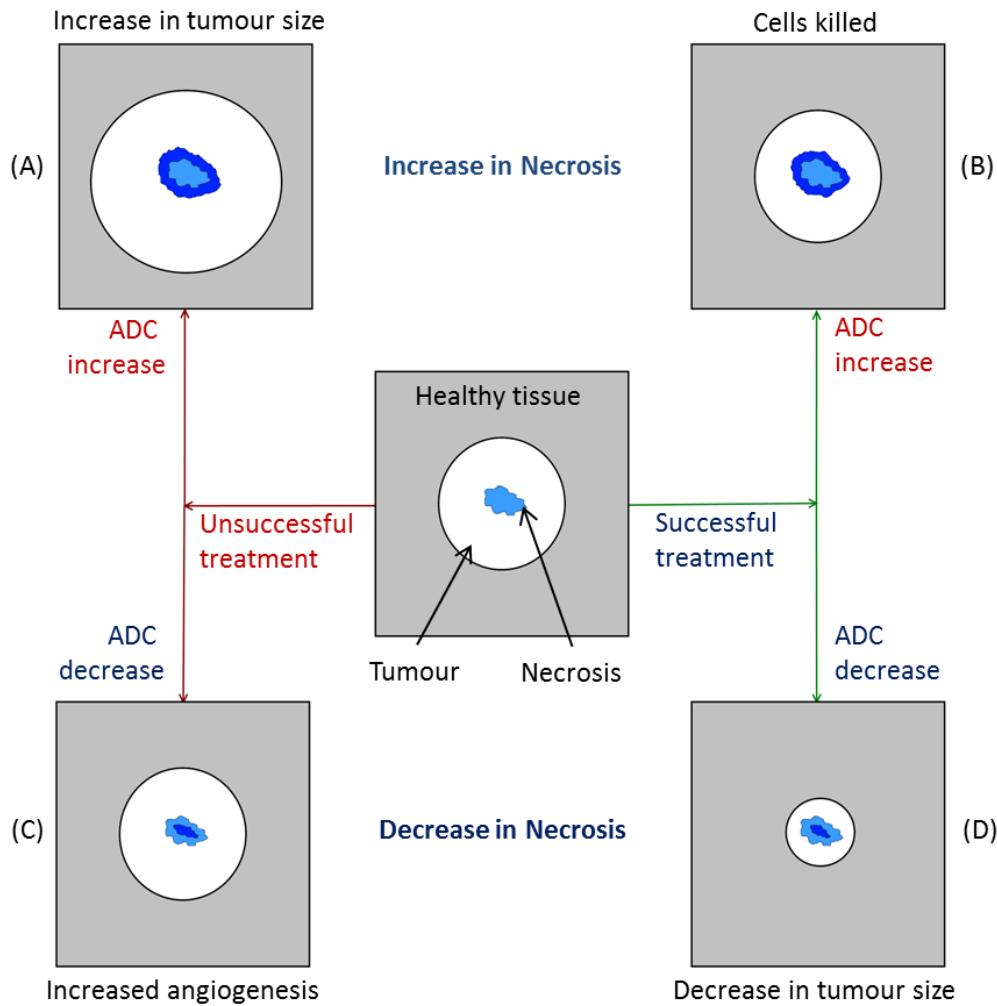


**Figure 7.2: Theoretical change in areas of necrosis by treatment.** Necrotic areas of a tumour can increase in size as a result of (A) tumour growth (causing increased hypoxic regions and hence necrosis) and (B) successful treatment (as cells are killed, tumour regions are replaced by areas of necrosis). Conversely, a reduction in size of necrotic regions can be due to (C) tumour growth through angiogenesis (making the tumour more vascular and hence more cellular in areas which would have otherwise been necrotic), and (D) tumour size reduction due to successful treatment (as the tumour shrinks in size, areas of necrosis may be replaced by glial cells).

### 7.2.4 TUMOUR GRADE

Most fDM studies have been carried out on adults in high grade tumours.<sup>122,180,181</sup> Given that high and low grade tumours differ in ADC<sup>86</sup>, the corresponding fDM may also differ in terms of treatment response classification. Figure 7.3 shows the theoretical changes that can occur to the ADC and the fDM when high and low grade tumours respond to treatment or show signs of progressive disease. The fDM in high-grade (GBM – WHO grade IV), mid-grade (DIPG – WHO grade II and III) and low-grade (OPG – WHO grade I) tumours were analysed and findings compared with the outcome described in clinical reports obtained at the time of the follow-up (second) imaging session.

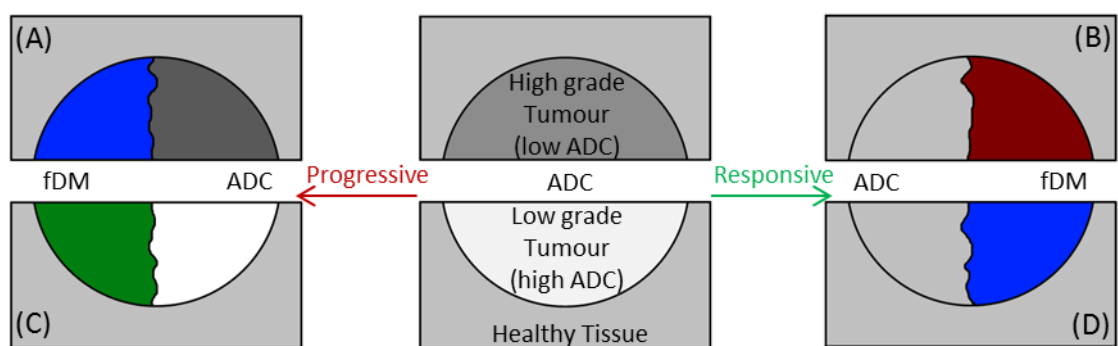


**Figure 7.3: Theoretical changes in the fDM in tumours of varying grade.** (red represents an increase, blue a decrease and green no change in ADC). The upper half of the image shows the theoretical change in ADC in high grade tumours which appear dark with low ADC values. (A) Progressive high grade tumours will increase in cellularity and result in a lower, and darker, ADC value (blue in fDM). (B) Conversely, a high grade tumour responding well to therapy will decrease in cellularity and increase in ADC to values more similar to that of healthy tissue (red in fDM). The lower half of the image shows the theoretical change in ADC in low grade tumours which appear bright with high ADC values. (C) In progressive disease it is expected the tumour will either grow or become necrotic hence, excluding areas of necrosis, it is not expected to change in ADC (green in fDM) – which is also indicative of stable disease. (D) Low grade tumours which respond to therapy are likely to be replaced by lower ADC healthy tissue and hence responsive low grade tumours would decrease in ADC (blue in fDM).

### 7.2.5 CHANGE IN TUMOUR SIZE

SEGA patients were found to respond well to rapamycin<sup>182</sup> and the effect of a reduction in tumour size was addressed by analysing the fDM in this patient group as there was a positive response to treatment, with the tumour decreasing in size considerably in three of four patients. The images were analysed using first a pre-treatment mask and then the overlap between the pre-treatment tumour areas and post-treatment tumour area. fDM findings were then compared to clinical imaging reports at the time of the follow-up (second) image.

### 7.2.6 STATISTICAL ANALYSIS

In order to analyse the fDM in areas of necrosis and in tumours of varying grade, contingency tables were constructed (Tables 7.1 and 7.2). Fisher's exact test<sup>183</sup> was applied to these tables using MATLAB and a pre-defined function<sup>184</sup>. Contingency tables show how categorical variables are related to each other by representing the frequency distribution of the variables analysed. Fisher's exact test allows for the analysis of such tables, particularly when the sample size is small.

## 7.3 Results

Of the patients included in this study, none of the DIPG and OPG patients had partial or total resection of tumour. 2 GBM patients, 1 GC patient and all 4 SEGA patients had partial or total resection of tumour. The fDM was built in 11 patients pre- and post-treatment, in 20 patients using two post-treatment images, and in 3 patients using two pre-treatment images were a watch and wait or a palliative care protocol was employed. The time interval between the two images ranged from 2 weeks to 13 months.

### 7.3.1 AREAS OF NECROSIS

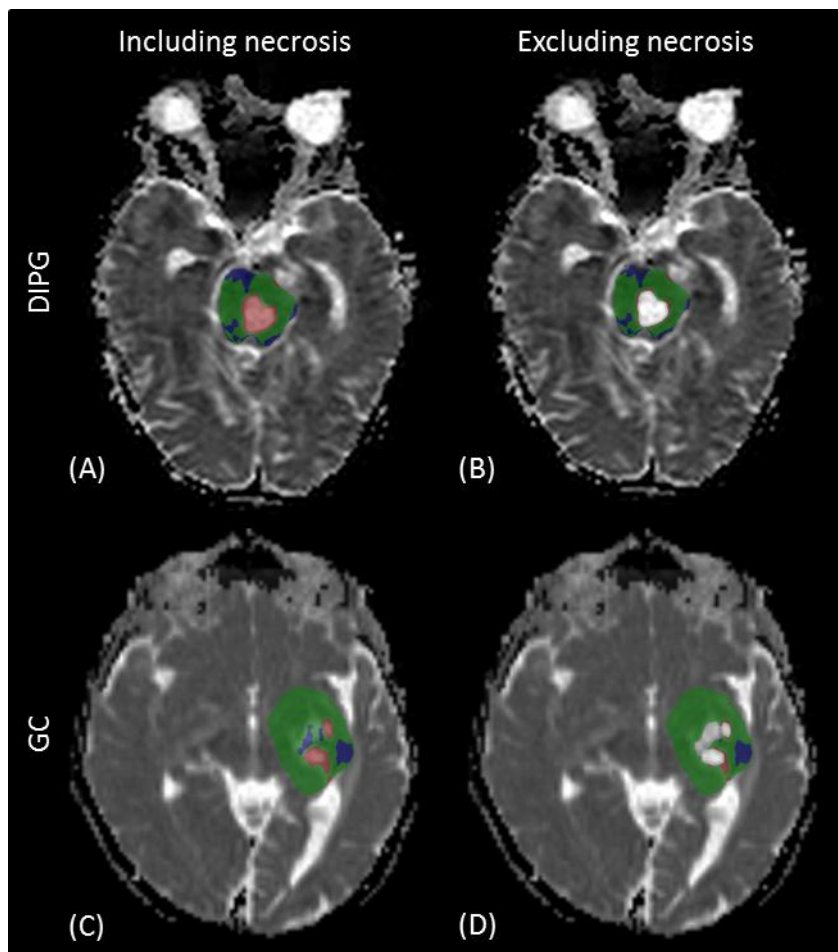


**Figure 7.4: The fDM in areas of necrosis.** The DIPG patient was treated with radiotherapy and chemotherapy and the fDM was constructed from one-post treatment image and a 3 months follow-up image. (A, B) The fDM in DIPG shows areas of increased ADC (red) (A) which are eliminated when excluding areas of necrosis (B). The GC patient was treated via surgery followed by chemotherapy and the fDM was constructed from one image taken 3 months after start of chemotherapy and a 1 year follow-up image. (C, D) The fDM in GC showed areas of increased ADC in necrotic regions (C) which were again eliminated when necrotic regions were excluded (D). Removal of the necrotic regions is concordant with no tumour response in two patients with no change in tumour size.

**Table 7.1: The fDM in necrotic areas compared to clinical response and change in size in necrotic areas.**

The fDM in necrotic areas	ADC			P value
	Increase	No Change	Decrease	
Size of Necrotic Area	Increase	6		
	No Change		3	
	Decrease			4      P < 0.001
Clinical Response	Response	3	1	1
	Stable	2		
	Progression	1	2	3      P = 0.31

In the DIPG patient group, the tumour area consisted of, on average, 11.2% necrosis while the GC patient group had on average 31.6% necrosis; measured by calculating the percentage of voxels with an ADC higher than  $1.8 \times 10^{-3} \text{ mm}^2 \text{s}^{-1}$  in the tumour ROI. 10/18 patients with DIPG and all 3 patients with GC showed areas of necrosis > 5%. In all of these cases, an increase or decrease in ADC in areas of necrosis was related to an increase or decrease in size of necrotic regions respectively and was not related to the treatment response identified in clinical image reports. Table 7.1 shows a summary of the fDM in necrotic areas and how these related to the size of necrotic areas and clinical response. Fisher's exact test on this data confirmed the fDM in areas of necrosis to be related to the change in size of necrotic areas ( $p < 0.001$ ) and was not related to clinical response ( $p = 0.31$ ). When classifying tumour response using the fDM, excluding areas of necrosis made a difference in four out of 21 patients studied. Figure 7.1 shows two examples of the fDM showing an increase in ADC in areas of necrosis while clinical image reports identified stable disease in both cases.

### 7.3.2 TUMOUR GRADE

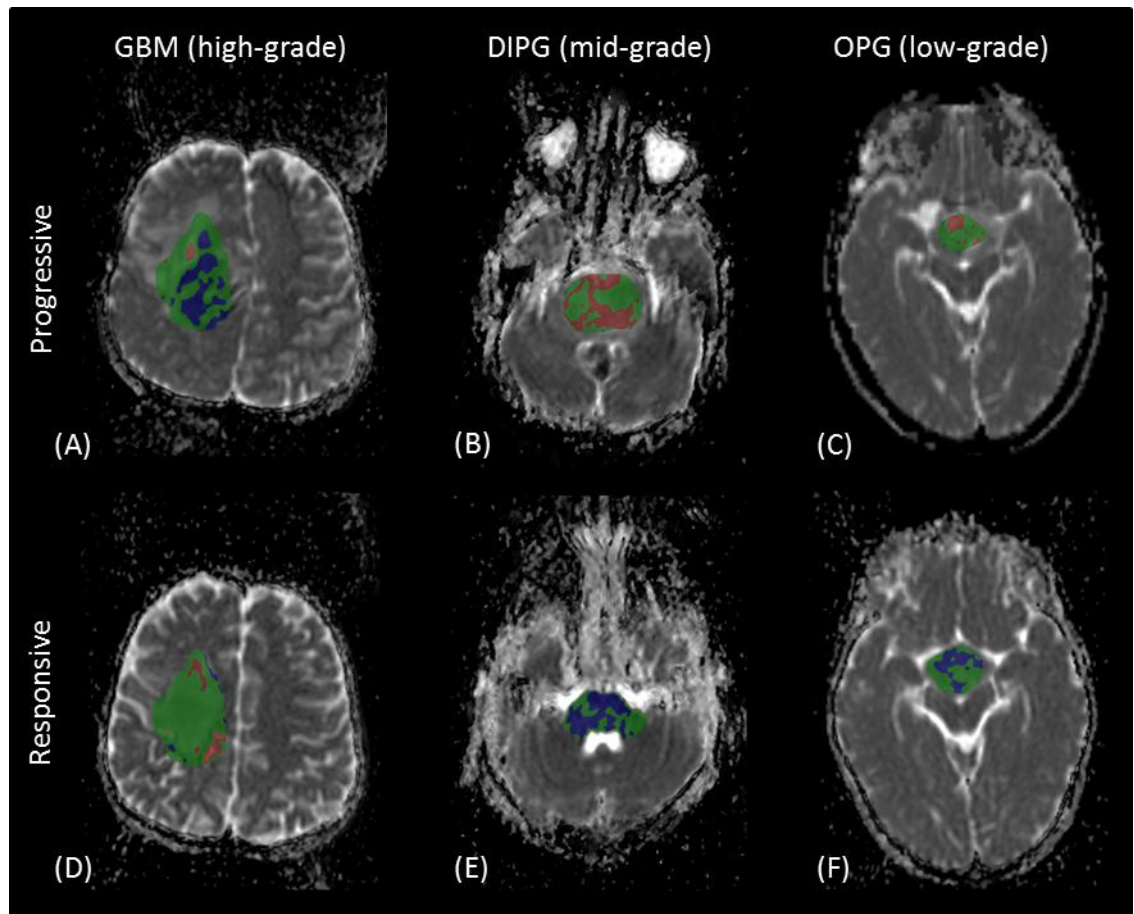


**Figure 7.5: The fDM in tumours of varying grade.** A comparison of the fDM in GBM (A, D), DIPG (B,E), and OPG (C, F), in areas of progression (top row) and treatment response (bottom row) is shown. (A) In high grade tumours a decrease in ADC (blue) was indicative of an increase in cellularity and progression. (E,F) In mid- and low grade tumours a decrease in ADC was indicative of positive treatment response as high ADC tumour was replaced by healthy tissue. (D) Similarly an increase in ADC (red) was indicative of positive treatment response in high grade tumours, and in the above cases, (B,C) progression in mid- and low grade tumours (B, C). Tumour progression and treatment response was defined by a radiologist at the time of second imaging.

The fDM in GBM (high-grade) showed areas of decreased ADC at progression, and areas of increased ADC with positive treatment response. Conversely, in DIPG (mid-grade) and OPG (low-grade), the fDM showed areas of increased ADC at progression and areas of decreased ADC at tumour treatment response (Figure 7.5). In the lower grade tumours it was noted that an increase in ADC was mostly associated with an increase in necrotic/cystic components of the tumour.

**Table 7.2: fDM changes by tumour grade and clinical response.**

The fDM by tumour grade		Tumour Grade			P value
fDM increase in ADC	Clinical Response	High-	Mid-	Low-	
		Response	1		
		Stable			
fDM no change in ADC	Clinical Response	Progression	5	1	P < 0.001
		Response	2		
		Stable	3	6	
fDM decrease in ADC	Clinical Response	Progression	1	3	P = 0.04
		Response	5	4	
		Stable			
		Progression	2		P < 0.001

Table 7.2 shows a summary of the changes in the fDM according to tumour grade and response. Fisher's exact test showed that there was a significant difference between tumour grade and clinical response for the increase and decrease in ADC ( $p<0.001$ ). The comparison between grade and clinical response when the tumour fDM did not change was only marginally significant ( $p=0.04$ ).

Of the 3 GBM patients, one showed small areas of increased ADC at response and large areas of decreased ADC at progression. A second patient showed small areas of decreased ADC at progression. In the third patient negligible changes in ADC were observed at progression.

Of the 18 DIPG patients, 8 progressed at second imaging with 5 showing an increase in ADC and 3 showing minor to no changes in ADC; 7 responded to treatment with 5 showing a decrease in ADC and 2 showing minor to no changes in ADC; 3 showed stable disease with minor changes in ADC.

Of the 6 OPG patients, 4 showed areas of decreased ADC at treatment response and minor to no change at stable disease, with one of these patients progressing at a later time point and showing increased ADC; 2 patients showed minor to no changes in ADC with stable disease.

### 7.3.3 CHANGE IN TUMOUR SIZE

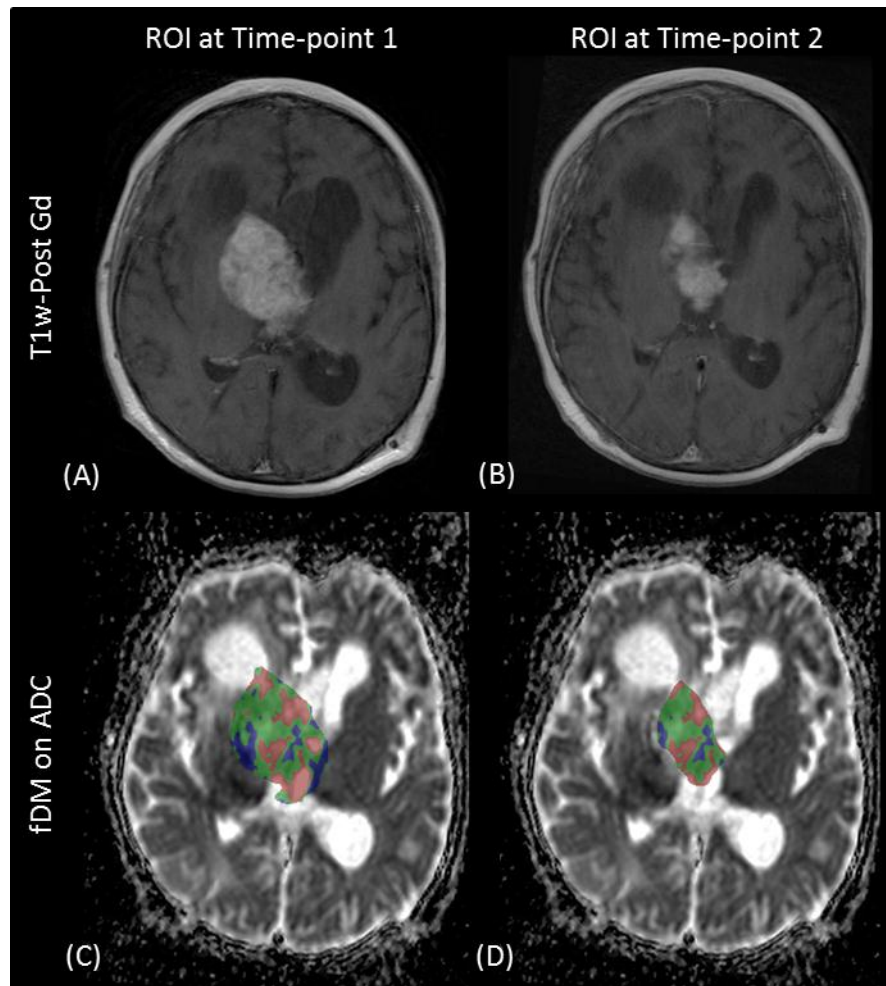


**Figure 7.6: Change in tumour size.** A comparison of the fDM when using (A,C) a pre-treatment mask and (B, D) only the overlap between pre- and post-treatment images is shown in a SEGA patient. The top row shows T1-weighted post-contrast imaging. The bottom row shows the fDM in one patient, showing (C) a mixture of areas of increased ADC (red) and decreased ADC (blue) when considering the pre-treatment mask, and (D) mostly areas of increased ADC when considering the tumour overlap area.

Of the 4 SEGA patients analysed, there was a large decrease in tumour size in 3 patients. When using pre-treatment masks, the fDM showed a large area of decreased ADC in the three SEGA patients responding to treatment. These areas were excluded from the fDM when looking at only the overlap (Figure 7.6). Outside of the tumour overlap areas, a decrease in ADC was observed when tumour areas were replaced by healthy tissue, and an increase in ADC was observed when tumour areas were replaced by areas of cerebrospinal fluid (CSF). In selecting only tumour overlap areas, a

more accurate assessment of the fDM findings was therefore given, although results did not indicate the fDM to give any more information than standard clinical imaging reports.

#### 7.3.4 HISTOLOGY

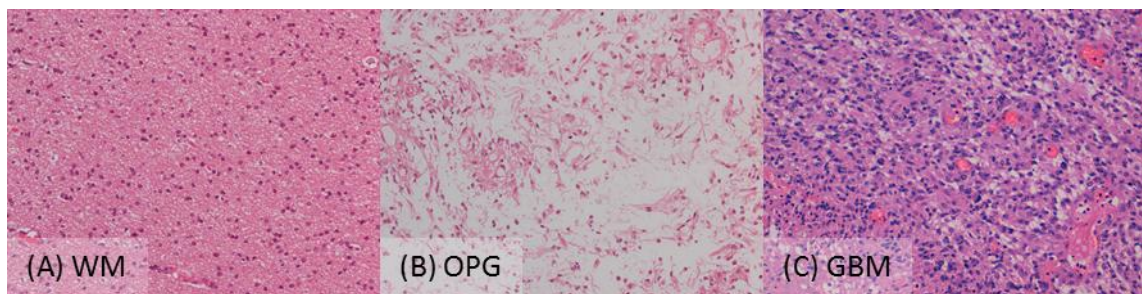


**Figure 7.7: Histological comparison of low and high-grade tumours.** A comparison of a low-grade OPG (B), with a histological diagnosis of pilocytic astrocytoma (WHO grade 1), and a high-grade GBM (C) are shown together with a comparative image from normal appearing white matter (WM) (A). The low-grade tumour showed some areas with high cellularity (as compared to WM) as well as myxoid areas shown in B. The microcystic changes observed in the low-grade tumour, could explain the increased ADC observed in these tumours when compared to normal appearing white matter. The high-grade tumour (C) showed the highest cellularity, which restricts diffusion and explains why these tumours appear dark in ADC images. (All images are haematoxylin-eosin stained and at the same magnification.)

A comparison of high-grade (GBM), low-grade (OPG) and normal appearing white matter is shown in Figure 7.7. The low-grade tumour had some areas of increased cellularity compared to normal appearing white matter and some myxoid areas with a loose microcystic stroma. This may help explain the increased ADC observed in low-grade tumours. The high-grade tumour showed the highest cellularity and due to this restricted diffusion, these tumours appear dark in an ADC image.

## 7.4 Discussion

Determining treatment response early on in the treatment cycle is of vital importance as this allows the choice of personalised medicine with the ability to alter doses or change therapy in those cases where the current treatment is seen to be ineffective. The fDM was previously shown to be an effective biomarker for detecting treatment

response earlier than current standard techniques which consist of radiological assessment, in most cases at the end of therapy.<sup>122</sup> However, in this analysis, a number of limitations have been identified and studied, and these indicated the need to exercise caution when interpreting fDM results.

#### **7.4.1 AREAS OF NECROSIS**

Necrotic areas of a tumour can increase in size both as a result of successful treatment (as cells are killed, tumour regions are replaced by areas of necrosis), as well as a result of tumour growth (causing increased hypoxic regions and hence necrosis). The results of this study indicate that the fDM does not give an accurate interpretation of treatment response in areas of necrosis. An increase/decrease in ADC in these areas was mostly related to an increase/decrease in necrotic areas rather than positive treatment response or progression. Eliminating areas of necrosis made a difference in treatment response classification in 20% of the patients studied, and given such areas may act as a potential confounder in the fDM, the study suggests excluding these areas from the fDM in order to accurately assess tumour response.

#### **7.4.2 TUMOUR GRADE**

Our results have identified tumour grade as a potential confounder in the fDM and the importance of taking this into consideration in analysing the fDM has been shown. Previous publications have shown an increase in ADC in the fDM to be indicative of positive treatment response<sup>118</sup>, and a decrease in ADC to be indicative of tumour progression<sup>181</sup>. This concept is underpinned by research which showed the ADC to be inversely correlated with cellularity.<sup>74</sup> This was based on the assumption that the ADC is lower in tumour tissue than in surrounding healthy tissue, due to the increased cellularity of tumours. While this is valid in high grade tumours, in lower grade tumours, tumour tissue can include microcystic areas or areas of infiltrative oedema, driving the ADC up, even though the cellularity of the tumour itself may be higher than that of surrounding tissue.<sup>86</sup> Unless there is tumour progression from low- to high-grade, a decrease in ADC in low grade tumours is therefore likely to be a sign of treatment response, as the higher ADC tumour tissue is being replaced by healthy tissue, rather than the tumour progressing by becoming more cellular. Furthermore,

an increase in ADC in low grade tumours is more likely to be associated with an increase in necrotic regions and, as shown in this study, tumour response cannot be inferred from these areas.

#### **7.4.3 CHANGE IN TUMOUR SIZE**

Previous research has shown how image registration, particularly due to an increase in tumour size, may be a major limitation to the technique employed in the fDM, and methods of non-linear registration may be beneficial.<sup>185</sup> In the cases investigated in this study, there was a considerable decrease in tumour size. In tumour regions replaced by healthy tissue, a decrease in ADC was observed in the areas where there was a reduction in size back to healthy tissue, and an increase in ADC where tumour areas were replaced by CSF. In the leftover tumour volume, areas of decreased ADC were limited and hence no inference could be made as regards to treatment success or progression. Given the limited number of patients in this group no definite conclusion can be drawn as to whether reduction in size is a confounder in the fDM when using linear registration – however a reduction in size is already an indicator of treatment success and the fDM did not appear to give any further information in the patients analysed. That said changes in tumour size need to be treated with caution, and careful visual inspection of registered images needs to be carried out in order to avoid problems of registration due to a change in tumour size.

#### **7.4.4 STUDY LIMITATIONS**

The main limitation of this study is that it was carried out on a group of childhood brain tumours, having small numbers of similar tumours. However, different tumour types were specifically selected so that the fDM could be evaluated in paediatric tumours of differing grade. Case ascertainment was limited by the rarity of childhood brain tumours and the fact that patients often arrive at our institution with pre-treatment imaging that did not include comparable DWI to allow an fDM to be generated. In some cases surgery took place immediately, and hence the fDM could only be applied to two post-treatment images. However, fDM results were compared to clinical imaging reports at the time of follow-up (second) imaging rather than the final clinical outcome in order to minimise this limitation. Further analyses are

warranted on other tumour types and in larger numbers in order to evaluate more fully the effects of the confounders described here on the fDM.

While the majority of patients were imaged on one scanner, the fDM in some patients was constructed from one image from each of the two scanners, and thus the reproducibility of ADC parameters needs to be considered and may affect the results. However, as discussed in Chapter 5, the inter-scanner variability of ADC was observed to be  $\pm 0.02 \times 10^{-3} \text{mm}^2\text{s}^{-1}$  in grey and white matter and  $\pm 0.12 \times 10^{-3} \text{mm}^2\text{s}^{-1}$  in the brain stem. These thresholds are much smaller than the fDM threshold used in this study to determine an increase or decrease in ADC ( $0.40 \times 10^{-3} \text{mm}^2\text{s}^{-1}$ ) and hence it is expected that using data from the two different scanners would have a negligible impact on the results.

## 7.5 Conclusion

In conclusion, results from this chapter have shown that, while the fDM may be a useful tool for determining tumour treatment response, careful interpretation needs to be carried out, considering the underlying biology of both tumour and healthy tissue. Areas of necrosis, tumour grade and change in tumour size are all factors that need to be taken into account when carrying out fDM analyses.

## Chapter 8 DISCUSSION

This chapter intends to bring together the main points from the research work carried out as part of this thesis by describing the advances made and outlining how these advances may be used in future studies to expand our current knowledge of diffusion imaging in paediatric brain tumours and beyond.

### 8.1 Advances made

Three studies were performed as part of this thesis. The first, explored in Chapter 5, was a comprehensive analysis of the reproducibility of diffusion imaging parameters – ADC, D, f, MD and FA. In this study, nine volunteers and one phantom were scanned on four 1.5T scanners and four 3T scanners using sequences employed for routine clinical use locally. A mixed-effect model was constructed and ADC, D, MD and FA were found to have a good reproducibility and vary by less than 4% across all scanners. On the other hand, f was found to have a poor reproducibility and to be affected by scan acquisition resolution. The study showed that diffusion imaging parameters are robust across 1.5T and 3T scanners and are suitable for use in multi-centre clinical studies and trials.

The second study, presented in Chapter 6, analysed the use of the gradient change in ADC across the tumour border, from oedema into the tumour core (ATCT), as a measure of survival in children with embryonal brain tumours. Identifying biomarkers of survival is important in managing and planning the treatment of childhood brain tumours. The survival analysis, on fifty-eight patients, confirmed being under the age of 3 years at diagnosis and partial surgical resection contribute to lower survival. Furthermore, it identified ATCT as a good biomarker of survival, with a more negative value correlating with reduced survival. This correlation was found to be irrespective of tumour type, extent of surgical resection, age less than 3 years at diagnosis and metastases at presentation.

The third study, described in Chapter 7, involved an analysis of the functional diffusion map in paediatric brain tumours. The fDM has been recommended as a tool for determining early treatment response. In the study three factors which may affect the fDM were examined: areas of necrosis, tumour grade, and change in tumour size. Thirty-four paediatric patients with a range of brain tumours were enrolled in the study and a qualitative analysis was carried out to determine how fDM findings may be affected by each of the confounds. This was done by comparing the fDM to clinical image reports. Results showed that the fDM in areas of necrosis did not discriminate between treatment response and progression. Furthermore, tumour grade appears to alter the behaviour of the fDM: while a decrease in ADC in a high grade tumour is a sign of tumour progression, a decrease in ADC in a low grade tumour may be a sign of response to treatment. Finally, results suggested that only the tumour overlap area should be considered when analysing tumours which change in size considerably. The study concluded that, while the fDM may be useful in determining treatment response, careful interpretation needs to take into account areas of necrosis, tumour grade and change in tumour size.

## 8.2 Future studies

The results from the reproducibility study pave the way for a host of analyses which could be performed by combining multi-centre data. As paediatric brain tumours are rare, combining multi-centre data may be necessary for significant and meaningful analyses. Furthermore, multi-centre analyses are essential in order to show how biomarkers of survival or treatment response can be used clinically across centres.

Following on from the reproducibility study, the analysis on ATCT as a biomarker of survival in embryonal brain tumours could be expanded to encompass data from multiple-centres in order to determine whether the correlation found applies across centres, and to further determine the usefulness of the biomarker. The analysis could also be taken forward by conducting a histological comparison in order to understand better what the biomarker is representing in biological terms.

Finally the study on the fDM recommends caution in generalising the tool for determining treatment response across all tumours and that the underlying biology needs to be taken into account. A more specific fDM analysis on individual tumour types could be carried out by incorporating multi-centre data in order to analyse the utility of the technique in individual tumour types.

### 8.3 Conclusion

Diffusion MRI is a valuable tool in the management of childhood brain tumours. It has been explored in this thesis as a biomarker of survival and as a tool for determining early treatment response in paediatric brain tumours. A multi-centre study on diffusion imaging parameters showed a good reproducibility, and this result paves the way for further research and validation of biomarkers in the field.

## APPENDIX A: LIST OF PUBLICATIONS AND CONFERENCE PRESENTATIONS ATTRIBUTED TO THIS THESIS

### Journal Papers

Grech-Sollars M, Saunders DE, Phipps KP, Kaur R, Paine SML, Jacques TS, Clayden JD, Clark CA. Challenges for the functional diffusion map in paediatric brain tumours. *Neuro Oncol.* 2014; 16(3):449–456.

Grech-Sollars M, Saunders DE, Phipps KP, Clayden JD, Clark CA. Survival Analysis for Apparent Diffusion Coefficient Measures in Children with Embryonal Brain Tumours. *Neuro Oncol.* 2012; 14(10):1285-1293.

### Conferences and meetings oral presentations

Grech-Sollars M, Hales PW, Miyazaki K, Raschke F, Rodriguez D, Wilson M, Gill SK, Banks T, Saunders DE, Clayden JD, Gwilliam MN, Barrick TR, Morgan PS, Davies NP, Rossiter J, Auer DP, Grundy R, Leach MO, Howe FA, Peet AC, Clark CA. Multi-centre reproducibility of diffusion MRI parameters for standard clinical sequences in the brain. *Proceedings of the Joint Annual Meeting of the International Society for Magnetic Resonance in Medicine and the European Society for Magnetic Resonance in Medicine and Biology*, Milan, Italy. 2014; 1684.

Grech-Sollars M, Saunders DE, Phipps KP, Clayden JD, Clark CA. Challenges for the functional diffusion map in paediatric brain tumours. *CCLG Functional Imaging Group Scientific Meeting*, Birmingham, UK. 2013.

Grech-Sollars M, Saunders DE, Phipps KP, Clayden JD, Clark CA. The functional diffusion map (fDM) in diffuse intrinsic pontine gliomas (DIPG). *Proceedings of the Annual Meeting of the ISMRM British Chapter*, Cambridge, UK. 2012; 40.

Grech-Sollars M, Saunders DE, Phipps KP, Clayden JD, Clark CA. Survival Analysis for Apparent Diffusion Coefficient Measures in Children with Embryonal Brain Tumours. *CCLG Functional Imaging Group Scientific Meeting*, Birmingham, UK. 2012.

Grech-Sollars M, Saunders DE, Phipps KP, Clayden JD, Clark CA. Survival Analysis for Apparent Diffusion Coefficient Measures in Children with Embryonal Brain Tumours. (Oral poster presentation) *Proceedings of the Annual Meeting of the British Neuro-Oncology Society*, Cambridge, UK. 2011; 22.

Grech-Sollars M, Saunders DE, Phipps KP, Clayden JD, Clark CA. Survival Analysis for Apparent Diffusion Coefficient Measures in Children with Primitive Neuroectodermal Tumours. *CCLG Cancer Imaging Programme Workshop*, Birmingham, UK. 2010.

#### **Conferences and meetings poster presentations**

Grech-Sollars M, Saunders DE, Phipps KP, Kaur R, Clayden JD, Clark CA. Challenges for the functional diffusion map in paediatric brain tumours. *Proceedings of the 45th Congress of the International Society of Paediatric Oncology*, Hong Kong. 2013.

Grech-Sollars M, Saunders DE, Phipps KP, Kaur R, Clayden JD, Clark CA. Challenges for the functional diffusion map in paediatric brain tumours with different grades. *Proceedings of the International Society for Magnetic Resonance in Medicine 21st Annual Meeting & Exhibition*, Salt Lake City, USA. 2013; 2187.

Grech-Sollars M, Saunders DE, Phipps KP, Kaur R, Clayden JD, Clark CA. Challenges for the functional diffusion map in paediatric brain tumours. *Proceedings of the ISMRM Workshop: Magnetic Resonance of Cancer Gone Multimodal*, Valencia, Spain. 2013; 22.

Grech-Sollars M, Saunders DE, Phipps KP, Clayden JD, Clark CA. The functional diffusion map (fDM) in diffuse intrinsic pontine gliomas (DIPG). *Proceedings of the 10<sup>th</sup> Congress of the European Association of NeuroOncology*, Marseille, France. 2012; 71.

Grech-Sollars M, Saunders DE, Phipps KP, Clayden JD, Clark CA. Areas of necrosis can act as a confounding factor in the functional diffusion map (fDM). *Proceedings of the International Society for Magnetic Resonance in Medicine 20th Annual Meeting & Exhibition*, Melbourne, Australia. 2012; 871.

Grech-Sollars M, Saunders DE, Phipps KP, Clayden JD, Clark CA. Survival Analysis for Apparent Diffusion Coefficient Measures in Children with Embryonal Brain Tumours. *Proceedings of the International Society for Magnetic Resonance in Medicine 20th Annual Meeting & Exhibition*, Melbourne, Australia. 2012; 847.

Grech-Sollars M, Saunders DE, Phipps KP, Clayden JD, Clark CA. Areas of necrosis can act as a confounding factor in the functional diffusion map (fDM). *Proceedings of the 3rd Annual Cancer Research UK & EPSRC Cancer Imaging Conference*, London, UK. 2012.

Grech-Sollars M, Saunders DE, Phipps KP, Clayden JD, Clark CA. Survival Analysis for Apparent Diffusion Coefficient Measures in Children with Embryonal BrainTumours. *Proceedings of the Annual Meeting of the ISMRM British Chapter*, Manchester, UK. 2011; 99.

Grech-Sollars M, Saunders DE, Phipps KP, Clayden JD, Clark CA. Survival Analysis for Apparent Diffusion Coefficient Measures in Children with Primitive Neuroectodermal Tumours. *Proceedings for the UCL Neuroscience Symposium*, London, UK. 2011; 175.

Grech-Sollars M, Saunders DE, Phipps KP, Clayden JD, Clark CA. Survival Analysis for Apparent Diffusion Coefficient Measures in Children with Primitive Neuroectodermal Tumours. *Proceedings of the Society for Neuro-Oncology 2011 Pediatric Neuro-Oncology Basic and Translational Research Conference*, New Orleans, USA. 2011; 22.

Grech-Sollars M, Saunders DE, Phipps KP, Clayden JD, Clark CA. Survival Analysis for Apparent Diffusion Coefficient Measures in Children with Primitive Neuroectodermal

Tumours. *Proceedings of the 2nd Annual Cancer Research UK & EPSRC Cancer Imaging Conference*, London, UK. 2011.

## REFERENCES

1. Marin T, Moore J. Understanding near-infrared spectroscopy. *Adv neonatal care.* 2011;11(6):382-388.
2. Rabi I, Zacharias J, Millman S, Kusch P. A new method of measuring nuclear magnetic moment. *Phys Rev.* 1938;53:318.
3. Purcell E, Torrey H, Pound R. Resonance absorption by nuclear magnetic moments in a solid. *Phys Rev.* 1945;69:37-38.
4. Bloch F. Nuclear induction. *Phys Rev.* 1946;70:460-474.
5. McRobbie DW, Moore EA, Graves MJ, Prince MR. *MRI from Picture to Proton.* 2nd ed. Cambridge University Press; 2007.
6. Carr H, Purcell E. Effects of diffusion on free precession in nuclear magnetic resonance experiments. *Phys Rev.* 1954;94(3):630-638.
7. Stejskal EO, Tanner JE. Spin Diffusion Measurements: Spin Echoes in the Presence of a Time-Dependent Field Gradient. *J Chem Phys.* 1965;42(1):288-292.
8. Clark CA, Le Bihan D. Water diffusion compartmentation and anisotropy at high b values in the human brain. *Magn Reson Med.* 2000;44(6):852-859.
9. Le Bihan D, Breton E, Lallemand D, Grenier P, Cabanis E, Laval-Jeantet M. MR imaging of intravoxel incoherent motions: application to diffusion and perfusion in neurologic disorders. *Radiology.* 1986;161(2):401-407.
10. Jones DK, ed. *Diffusion MRI: Theory, Methods, and Applications.* Oxford University Press; 2011.

11. Basser PJ, Mattiello J, LeBihan D. MR diffusion tensor spectroscopy and imaging. *Biophys J.* 1994;66(1):259-267.
12. Mori S, Crain BJ, Chacko VP, van Zijl PC. Three-dimensional tracking of axonal projections in the brain by magnetic resonance imaging. *Ann Neurol.* 1999;45(2):265-269.
13. Jones DK, Simmons A, Williams SC, Horsfield MA. Non-invasive assessment of axonal fiber connectivity in the human brain via diffusion tensor MRI. *Magn Reson Med.* 1999;42(1):37-41.
14. Conturo T, Lori N, Cull T, et al. Tracking neuronal fiber pathways in the living human brain. *Proc Natl Acad Sci USA.* 1999;96(18):10422-10427.
15. Basser PJ, Pajevic S, Pierpaoli C, Duda J, Aldroubi a. In vivo fiber tractography using DT-MRI data. *Magn Reson Med.* 2000;44(4):625-632.
16. Mori S, Tournier J. *Introduction to Diffusion Tensor Imaging And Higher Order Models.* 2nd ed. Academic Press; 2013.
17. Johansen-Berg H, Behrens TE. *Diffusion MRI: From quantitative measurement to in-vivo neuroanatomy.* 1st ed. Academic Press; 2009.
18. Data Format Working Group. Neuroimaging Informatics Technology Initiative. 2005. Available at: <http://nifti.nimh.nih.gov/>. Accessed October 23, 2013.
19. Smith J. *MRI Convert* [computer program]. V2.0. Oregon: Lewis Centre for NeuroImaging; 2013. Available at: <http://lcni.uoregon.edu/~jolinda/MRIConvert>
20. Morgan P. *dtoa* [computer program]. Nottingham; Available at: <http://www.nottingham.ac.uk/~msapm1/software/dtoa.html>
21. Rorden C. *dcm2nii* [computer program]. South Carolina; 2012. Available at: <http://www.mccauslandcenter.sc.edu/mricron/dcm2nii.html>

22. Clayden J, Munoz Maniega S, Storkey AJ, King MD, Bastin ME, Clark CA. TractoR: Magnetic resonance imaging and tractography with R. *J Stat Softw*. 2011;44(8).
23. Wellcome Trust Centre for Neuroimaging. *SPM8* [computer program]. London; 2008. Available at: <http://www.fil.ion.ucl.ac.uk/spm/>
24. MathWorks Inc. *MATLAB* [computer program]. R2013a. 2013.
25. Padhani AR, Liu G, Koh DM, et al. Diffusion-weighted magnetic resonance imaging as a cancer biomarker: consensus and recommendations. *Neoplasia*. 2009;11(2):102–125.
26. Hales PW, Clark CA. Combined arterial spin labeling and diffusion-weighted imaging for noninvasive estimation of capillary volume fraction and permeability-surface product in the human brain. *J Cereb Blood Flow Metab*. 2013;33(1):67–75.
27. Jenkinson M, Beckmann CF, Behrens TEJ, Woolrich MW, Smith SM. FSL. *Neuroimage*. 2012;62(2):782–790.
28. Laboratory for Computational Neuroimaging. *FreeSurfer* [computer program]. V5.3. Massachusetts: Martinos Center for Biomedical Imaging; 2013. Available at: <http://surfer.nmr.mgh.harvard.edu/>
29. Development Core Team. R: *A language and environment for statistical computing* [computer program]. Vienna; 2010.
30. Kanal E, Barkovich a J, Bell C, et al. ACR guidance document on MR safe practices: 2013. *J Magn Reson Imaging*. 2013;37(3):501–530.
31. Ziegelberger G. Amendment to the ICNIRP “statement on medical Magnetic Resonance (MR) procedures: protection of patients.” *Health Phys*. 2009;97(3):259–261.

32. Sudhakar A. History of Cancer, Ancient and Modern Treatment Methods. *J Cancer Sci Ther.* 2009;1(2):1–4.
33. Rao PN, Johnson RT. Mammalian cell fusion: studies on the regulation of DNA synthesis and mitosis. *Nature.* 1970;225(5228):159–164.
34. Weinert TA, Kiser GL, Hartwell LH. Mitotic checkpoint genes in budding yeast and the dependence of mitosis on DNA replication and repair. *Genes Dev.* 1994;8(6):652–665.
35. Bolsover SR, Shephard EA, White HA, Hyams JS. *Cell Biology: A Short Course.* Wiley-Blackwell; 2011.
36. Stevens MCG, Caron HN, Biondi A. *Cancer in Children: Clinical Management.* 6th ed. OUP Oxford; 2012.
37. Clark S. *A Guide to Cancer Genetics: In Clinical Practice.* TFM Publishing Ltd; 2008.
38. Karp G. *Cell Biology.* John Wiley & Sons; 2010.
39. Hanahan D, Weinberg RA. The hallmarks of cancer. *Cell.* 2000;100(1):57–70.
40. Hanahan D, Weinberg RA. Hallmarks of cancer: the next generation. *Cell.* 2011;144(5):646–674.
41. Talmadge JE, Fidler IJ. AACR centennial series: the biology of cancer metastasis: historical perspective. *Cancer Res.* 2010;70(14):5649–5669.
42. Vogelstein B, Kinzler K. The multistep nature of cancer. *Trends Genet.* 1993;9(4):3–6.
43. Bower M, Waxman J. *Oncology (Lecture Notes).* 2nd ed. Wiley-Blackwell; 2010.
44. Crossman A, Neary D. *Neuroanatomy.* 4th ed. Churchill Livingstone; 2010.

45. Cancer Research UK. *Childhood Cancer – Great Britain & UK*. 2010.
46. DeVita VT, Hellman S, Rosenberg SA. *Cancer:principles & practice of oncology*. 7th ed. Philadelphia: Lippincott Williams & Wilkins; 2004:1834.
47. Merchant TE, Pollack IF, Loeffler JS. Brain tumors across the age spectrum: biology, therapy, and late effects. *Semin Radiat Oncol*. 2010;20(1):58-66.
48. Berghoff AS, Preusser M. Biology in prevention and treatment of brain metastases. *Expert Rev Anticancer Ther*. 2013;13(11):1339-1348.
49. McKinney P. Brain tumours: incidence, survival, and aetiology. *J Neurol Neurosurg Psychiatry*. 2004;75(suppl\_2):ii12-ii17.
50. Armstrong GT, Phillips PC, Rorke-Adams LB, Judkins AR, Localio a R, Fisher MJ. Gliomatosis cerebri: 20 years of experience at the Children's Hospital of Philadelphia. *Cancer*. 2006;107(7):1597-1606.
51. Jansen MHA, van Vuurden DG, Vandertop WP, Kaspers GJL. Diffuse intrinsic pontine gliomas: A systematic update on clinical trials and biology. *Cancer Treat Rev*. 2012;38(1):27-35.
52. Taylor MD, Northcott PA, Korshunov A, et al. Molecular subgroups of medulloblastoma: the current consensus. *Acta Neuropathol*. 2011.
53. Johnston DL, Keene DL, Lafay-Cousin L, et al. Supratentorial primitive neuroectodermal tumors: a Canadian pediatric brain tumor consortium report. *J Neurooncol*. 2008;86(1):101-108.
54. Gupta N, Banerjee A, Haas-Kogan D. *Pediatric CNS Tumors*. 2nd ed. Springer; 2009.
55. Al-Hussaini M, Sultan I, Abuirmileh N, Jaradat I, Qaddoumi I. Pineal gland tumors: experience from the SEER database. *J Neurooncol*. 2009;94(3):351-358.

56. Papadopoulos M, Saadoun S, Binder D, Manley G, Krishna S, Verkman A. Molecular mechanisms of brain tumor edema. *Neuroscience*. 2004;129(4):1011-1020.
57. Kimelberg HK. Current concepts of brain edema. *J Neurosurg*. 1995;83:1051-1059.
58. Proskuryakov SY, Gabai VL. Mechanisms of tumor cell necrosis. *Curr Pharm Des*. 2010;16(1):56-68.
59. Caroline I, Rosenthal M. Imaging modalities in high-grade gliomas: pseudoprogression, recurrence, or necrosis? *J Clin Neurosci*. 2012;19(5):633-637.
60. Pinkerton R, Plowman PN, Pieters R. *Paediatric Oncology*. 3rd ed. Arnold Publishers; 2004.
61. Green D, Wallace H. *Late Effects of Childhood Cancer*. Arnold Publishers; 2004.
62. Carroll WL. *Cancer in children and adolescents*. 1st ed. (Carroll WL, Finaly JL, eds.). Sudbury, Massachusetts: Jones and Bartlett Publishers, Inc; 2009.
63. Chenevert TL, Galbán CJ, Ivancevic MK, et al. Diffusion coefficient measurement using a temperature-controlled fluid for quality control in multicenter studies. *J Magn Reson Imaging*. 2011;34(4):983-987.
64. Malyarenko D, Galbán CJ, Londy FJ, et al. Multi-system repeatability and reproducibility of apparent diffusion coefficient measurement using an ice-water phantom. *J Magn Reson Imaging*. 2013;37(5):1238-1246.
65. Teipel SJ, Reuter S, Stieltjes B, et al. Multicenter stability of diffusion tensor imaging measures: A European clinical and physical phantom study. *Psychiatry Res*. 2011.

66. Zhou F-L, Hubbard PL, Eichhorn SJ, Parker GJM. Coaxially electrospun axon-mimicking fibers for diffusion magnetic resonance imaging. *ACS Appl Mater Interfaces*. 2012;4(11):6311-6316.
67. Bonekamp D, Nagae LM, Degaonkar M, et al. Diffusion tensor imaging in children and adolescents: reproducibility, hemispheric, and age-related differences. *Neuroimage*. 2007;34(2):733-742.
68. Veenith T V, Carter E, Grossac J, et al. Inter Subject Variability and Reproducibility of Diffusion Tensor Imaging within and between Different Imaging Sessions. *PLoS One*. 2013;8(6):e65941.
69. Sasaki M, Yamada K, Watanabe Y, et al. Variability in absolute apparent diffusion coefficient values across different platforms may be substantial: a multivendor, multi-institutional comparison study. *Radiology*. 2008;249(2):624-630.
70. Fox RJ, Sakaie K, Lee J-C, et al. A validation study of multicenter diffusion tensor imaging: reliability of fractional anisotropy and diffusivity values. *Am J Neuroradiol*. 2012;33(4):695-700.
71. Lemkaddem a, Daducci a, Vulliemoz S, et al. A multi-center study: intra-scan and inter-scan variability of diffusion spectrum imaging. *Neuroimage*. 2012;62(1):87-94.
72. Magnotta V a, Matsui JT, Liu D, et al. Multicenter reliability of diffusion tensor imaging. *Brain Connect*. 2012;2(6):345-355.
73. Vollmar C, O'Muircheartaigh J, Barker GJ, et al. Identical, but not the same: intra-site and inter-site reproducibility of fractional anisotropy measures on two 3.0T scanners. *Neuroimage*. 2010;51(4):1384-94.
74. Sugahara T, Korogi Y, Kochi M, et al. Usefulness of diffusion-weighted MRI with echo-planar technique in the evaluation of cellularity in gliomas. *J Magn Reson Imaging*. 1999;9(1):53-60.

75. Gauvain KM, McKinstry RC, Mukherjee P, et al. Evaluating pediatric brain tumor cellularity with diffusion-tensor imaging. *Am J Roentgenol.* 2001;177(2):449-454.
76. Jenkinson MD, Smith TS, Brodbelt AR, Joyce KA, Warnke PC, Walker C. Apparent diffusion coefficients in oligodendroglial tumors characterized by genotype. *J Magn Reson Imaging JMRI.* 2007;26(6):1405-1412.
77. Yamashita Y, Kumabe T, Higano S, Watanabe M, Tominaga T. Minimum apparent diffusion coefficient is significantly correlated with cellularity in medulloblastomas. *Neurol Res.* 2009;31(9):940-946.
78. Matsumoto Y, Kuroda M, Matsuya R, et al. In vitro experimental study of the relationship between the apparent diffusion coefficient and changes in cellularity and cell morphology. *Oncol Rep.* 2009;22(3):641-648.
79. Humphries PD, Sebire NJ, Siegel MJ, Olsen ØE. Tumors in pediatric patients at diffusion-weighted MR imaging: apparent diffusion coefficient and tumor cellularity. *Radiology.* 2007;245(3):848-854.
80. Prayson RA. *Neuropathology Review.* 1st ed. Humana Press; 2008.
81. Rosai J. *Surgical Pathology.* 9th ed. Mosby; 2004.
82. Koral K, Mathis D, Gargan L, Weprin B, Bowers DC, Margraf L. Common Pediatric Cerebellar Tumors : Correlation between Cell Coefficient Metrics. *Radiology.* 2013;268(2):532-537.
83. Stadlbauer A, Ganslandt O, Buslei R, et al. Gliomas: histopathologic evaluation of changes in directionality and magnitude of water diffusion at diffusion-tensor MR imaging. *Radiology.* 2006;240(3):803-810.
84. Beppu T, Inoue T, Shibata Y, et al. Fractional anisotropy value by diffusion tensor magnetic resonance imaging as a predictor of cell density and proliferation activity of glioblastomas. *Surg Neurol.* 2005;63(1):56-61.

85. Kinoshita M, Hashimoto N, Goto T, et al. Fractional anisotropy and tumor cell density of the tumor core show positive correlation in diffusion tensor magnetic resonance imaging of malignant brain tumors. *Neuroimage*. 2008;43(1):29-35.
86. Bull JG, Saunders DE, Clark CA. Discrimination of paediatric brain tumours using apparent diffusion coefficient histograms. *Eur Radiol*. 2012;22(2):447-457.
87. Rodriguez Gutierrez D, Awwad A, Meijer L, et al. Metrics and Textural Features of MRI Diffusion to Improve Classification of Pediatric Posterior Fossa Tumors. *Am J Neuroradiol*. 2013;1-7.
88. Rumboldt Z, Camacho DL a, Lake D, Welsh CT, Castillo M. Apparent diffusion coefficients for differentiation of cerebellar tumors in children. *AJNR Am J Neuroradiol*. 2006;27(6):1362-1369.
89. Schneider JF, Confort-Gouny S, Viola a, et al. Multiparametric differentiation of posterior fossa tumors in children using diffusion-weighted imaging and short echo-time <sup>1</sup>H-MR spectroscopy. *J Magn Reson Imaging*. 2007;26(6):1390-1398.
90. Pillai S, Singhal A, Byrne AT, Dunham C, Cochrane DD, Steinbok P. Diffusion-weighted imaging and pathological correlation in pediatric medulloblastomas-“They are not always restricted!”. *Childs Nerv Syst*. 2011;27(9):1407-1411.
91. Poretti A, Meoded A, Cohen KJ, Grotzer MA, Boltshauser E, Huisman TAGM. Apparent Diffusion Coefficient of Pediatric Cerebellar Tumors : A Biomarker of Tumor Grade? 2013;60:2036-2041.
92. Kralik SF, Taha A, Kamer a P, Cardinal JS, Seltman T a, Ho CY. Diffusion Imaging for Tumor Grading of Supratentorial Brain Tumors in the First Year of Life. *Am J Neuroradiol*. 2013;1-9.
93. Yuan W, Holland SK, Jones B V, Crone K, Mangano FT. Characterization of abnormal diffusion properties of supratentorial brain tumors: a preliminary diffusion tensor imaging study. *J Neurosurg Pediatr*. 2008;1(4):263-269.

94. Koral K, Zhang S, Gargan L, et al. Diffusion MRI Improves the Accuracy of Preoperative Diagnosis of Common Pediatric Cerebellar Tumors among Reviewers with Different Experience Levels. *Am J Neuroradiol.* 2013;34(12):2360-2365.
95. Saksena S, Jain R, Narang J, et al. Predicting survival in glioblastomas using diffusion tensor imaging metrics. *J Magn Reson Imaging.* 2010;32(4):788-795.
96. Zulfiqar M, Yousem DM, Lai H. ADC values and prognosis of malignant astrocytomas: does lower ADC predict a worse prognosis independent of grade of tumor?-a meta-analysis. *Am J Roentgenol.* 2013;200(3):624-629.
97. Aghi M, Gaviani P, Henson JW, Batchelor TT, Louis DN, Barker FG. Magnetic Resonance Imaging Characteristics Predict Epidermal Growth Factor Receptor Amplification Status in Glioblastoma. *Clin Cancer Res.* 2005;11(24):8600 -8605.
98. Thompson G, Cain JR, Mills SJ, Jackson A. Apparent Diffusion Coefficient Measures on MR Correlate with Survival in Glioblastoma Multiforme. *Proc Int'l Soc Mag Reson Med.* 2009;17:280.
99. Grech-Sollars M, Saunders DE, Phipps KP, Clayden JD, Clark CA. Survival analysis for apparent diffusion coefficient measures in children with embryonal brain tumours. *Neuro Oncol.* 2012;14(10):1285-1293.
100. Dimou S, Battisti R a, Hermens DF, Lagopoulos J. A systematic review of functional magnetic resonance imaging and diffusion tensor imaging modalities used in presurgical planning of brain tumour resection. *Neurosurg Rev.* 2013;36(2):205-214.
101. Tummala RP, Chu RM, Liu H, Truwit CL, Hall WA. Application of diffusion tensor imaging to magnetic-resonance-guided brain tumor resection. *Pediatr Neurosurg.* 2003;39(1):39-43.

102. D'Andrea G, Angelini A, Romano A, et al. Intraoperative DTI and brain mapping for surgery of neoplasm of the motor cortex and the corticospinal tract: our protocol and series in BrainSUITE. *Neurosurg Rev.* 2012;35(3):401-412.
103. Kuhnt D, Bauer MH a, Becker A, et al. Intraoperative visualization of fiber tracking based reconstruction of language pathways in glioma surgery. *Neurosurgery.* 2012;70(4):911-919.
104. Asao C, Korogi Y, Kitajima M, et al. Diffusion-weighted imaging of radiation-induced brain injury for differentiation from tumor recurrence. *Am J Neuroradiol.* 2005;26(6):1455-1460.
105. Bobek-Billewicz B, Stasik-Pres G, Majchrzak H, Zarudzki L. Differentiation between brain tumor recurrence and radiation injury using perfusion, diffusion-weighted imaging and MR spectroscopy. *Folia Neuropathol.* 2010;48(2):81-92.
106. Kashimura H, Inoue T, Beppu T, Ogasawara K, Ogawa A. Diffusion tensor imaging for differentiation of recurrent brain tumor and radiation necrosis after radiotherapy--three case reports. *Clin Neurol Neurosurg.* 2007;109(1):106-110.
107. Shah R, Vattoth S, Jacob R, et al. Radiation necrosis in the brain: imaging features and differentiation from tumor recurrence. *Radiographics.* 2012;32(5):1343-1359.
108. Lee WJW, Choi SSH, Park CK, et al. Diffusion-weighted MR imaging for the differentiation of true progression from pseudoprogression following concomitant radiotherapy with temozolomide in patients with newly diagnosed high-grade gliomas. *Acad Radiol.* 2012;19(11):1353-1361.
109. Song YS, Choi SH, Park C-K, et al. True progression versus pseudoprogression in the treatment of glioblastomas: a comparison study of normalized cerebral blood volume and apparent diffusion coefficient by histogram analysis. *Korean J Radiol.* 2013;14(4):662-672.

110. Chu HH, Choi SH, Ryoo I, et al. Differentiation of True Progression from Pseudoprogression in Glioblastoma Treated with Radiation Therapy and Concomitant Temozolomide: Comparison Study of Standard and High-b-Value Diffusion-weighted Imaging. *Radiology*. 2013;269(3):831-840.
111. Korchi AM, Garibotto V, Ansari M, Merlini L. Pseudoprogression after proton beam irradiation for a choroid plexus carcinoma in pediatric patient: MRI and PET imaging patterns. *Childs Nerv Syst*. 2013;29(3):509-512.
112. Minamikawa S, Kono K, Nakayama K, et al. Glucocorticoid treatment of brain tumor patients: changes of apparent diffusion coefficient values measured by MR diffusion imaging. *Neuroradiology*. 2004;46(10):805-811.
113. Bastin ME, Carpenter TK, Armitage P a, Sinha S, Wardlaw JM, Whittle IR. Effects of dexamethasone on cerebral perfusion and water diffusion in patients with high-grade glioma. *Am J Neuroradiol*. 2006;27(2):402-408.
114. Sinha S, Bastin ME, Wardlaw JM, Armitage P a, Whittle IR. Effects of dexamethasone on peritumoural oedematous brain: a DT-MRI study. *J Neurol Neurosurg Psychiatry*. 2004;75(11):1632-1635.
115. Steens SC a, Steup-Beekman GM, Bosma GPT, et al. The effect of corticosteroid medication on quantitative MR parameters of the brain. *Am J Neuroradiol*. 2005;26(10):2475-2480.
116. Nowosielski M, Recheis W, Goebel G, et al. ADC histograms predict response to anti-angiogenic therapy in patients with recurrent high-grade glioma. *Neuroradiology*. 2011;53(4):291-302.
117. Farjam R, Tsien CI, Feng FY, et al. Investigation of the diffusion abnormality index as a new imaging biomarker for early assessment of brain tumor response to radiation therapy. *Neuro Oncol*. 2014;16(1):131-139.

118. Moffat BA, Chenevert TL, Lawrence TS, et al. Functional diffusion map: a noninvasive MRI biomarker for early stratification of clinical brain tumor response. *Proc Natl Acad Sci U S A.* 2005;102(15):5524-5529.
119. Hamstra DA, Chenevert TL, Moffat BA, et al. Evaluation of the functional diffusion map as an early biomarker of time-to-progression and overall survival in high-grade glioma. *Proc Natl Acad Sci U S A.* 2005;102(46):16759-16764.
120. Moffat BA, Chenevert TL, Meyer CR, et al. The functional diffusion map: an imaging biomarker for the early prediction of cancer treatment outcome. *Neoplasia.* 2006;8(4):259-267.
121. Ellingson BM, Malkin MG, Rand SD, et al. Validation of functional diffusion maps (fDMs) as a biomarker for human glioma cellularity. *J Magn Reson Imaging.* 2010;31(3):538-548.
122. Hamstra DA, Galbán CJ, Meyer CR, et al. Functional diffusion map as an early imaging biomarker for high-grade glioma: correlation with conventional radiologic response and overall survival. *J Clin Oncol.* 2008;26(20):3387-3394.
123. Rodriguez Gutierrez D, Manita M, Jaspan T, Dineen R a, Grundy RG, Auer DP. Serial MR diffusion to predict treatment response in high-grade pediatric brain tumors: a comparison of regional and voxel-based diffusion change metrics. *Neuro Oncol.* 2013.
124. Grech-Sollars M, Saunders DE, Phipps KP, et al. Challenges for the functional diffusion map in pediatric brain tumors. *Neuro Oncol.* 2014;16(3):449-456.
125. Grech-Sollars M, Hales P, Miyazaki K, et al. Multi-centre reproducibility of diffusion MRI parameters for clinical sequences in the brain. In: *Proceedings of the Joint Annual Meeting International Society for Magnetic Resonance in Medicine – European Society for Magnetic Resonance in Medicine and Biology.*; 2014:1684.

126. Tofts PS, Lloyd D, Clark CA, et al. Test liquids for quantitative MRI measurements of self-diffusion coefficient in vivo. *Magn Reson Med.* 2000;43(3):368-374.
127. Holz M, Heil S, Sacco A. Temperature-dependent self-diffusion coefficients of water and six selected molecular liquids for calibration in accurate <sup>1</sup>H NMR PFG measurements. *Phys Chem Chem Phys.* 2000;2:4740-4742.
128. Dietrich O, Raya JG, Reeder SB, Reiser MF, Schoenberg SO. Measurement of signal-to-noise ratios in MR images: influence of multichannel coils, parallel imaging, and reconstruction filters. *J Magn Reson Imaging.* 2007;26(2):375-385.
129. Polders DL, Leemans A, Hendrikse J, Donahue MJ, Luijten PR, Hoogduin JM. Signal to noise ratio and uncertainty in diffusion tensor imaging at 1.5, 3.0, and 7.0 Tesla. *J Magn Reson Imaging.* 2011;33(6):1456-1463.
130. Edelstein W, Bottomley P, Pfeifer L. A signal-to-noise calibration procedure for NMR imaging systems. *Med Phys.* 1984;11(2):180.
131. Gudbjartsson H, Patz S. The Rician distribution of noisy MRI data. *Magn Reson Med.* 1995;34(6):910-914.
132. Dale AM, Fischl B, Sereno MI. Cortical surface-based analysis. I. Segmentation and surface reconstruction. 1999;194:179-194.
133. Fischl B, Sereno MI, Dale AM. Cortical surface-based analysis. II: Inflation, flattening, and a surface-based coordinate system. 1999;207:195-207.
134. Fischl B, Salat DH, Busa E, et al. Whole brain segmentation: automated labeling of neuroanatomical structures in the human brain. *Neuron.* 2002;33(3):341-355.
135. Jenkinson M, Bannister P, Brady M, Smith S. Improved Optimization for the Robust and Accurate Linear Registration and Motion Correction of Brain Images. *Neuroimage.* 2002;17(2):825-841.

136. Pekar J, Moonen CTW, van Zijl PCM. On the precision of diffusion/perfusion imaging by gradient sensitization. *Magn Reson Med.* 1992;23(1):122-129.
137. Mori S, Oishi K, Jiang H, et al. Stereotaxic white matter atlas based on diffusion tensor imaging in an ICBM template. *Neuroimage.* 2008;40(2):570-582.
138. Bates D, Maechler M, Bolker B, Walker S. *lme4: Linear mixed-effects models using S4 classes* [computer program]. 2013. Available at: <http://cran.r-project.org/web/packages/lme4/index.html>
139. Bates DM. *lme4: Mixed-effects modelling with R.* 2010.
140. Jones DK, Basser PJ. “Squashing peanuts and smashing pumpkins”: how noise distorts diffusion-weighted MR data. *Magn Reson Med.* 2004;52(5):979-993.
141. Maier SE, Sun Y, Mulkern R V. Diffusion imaging of brain tumors. *NMR Biomed.* 2010;23(7):849-864.
142. Wirestam R, Borg M, Brockstedt S, Lindgren a., Holtås S, Ståhlberg F. Perfusion-Related Parameters in Intravoxel Incoherent Motion Mr Imaging Compared with Cbv and Cbf Measured by Dynamic Susceptibility-Contrast Mr Technique. *Acta radiol.* 2001;42(2):123-128.
143. Lemke A, Laun FB, Simon D, Stieltjes B, Schad LR. An in vivo verification of the intravoxel incoherent motion effect in diffusion-weighted imaging of the abdomen. *Magn Reson Med.* 2010;64(6):1580-1585.
144. Leenders KL, Perani D, Lammertsma a a, et al. Cerebral blood flow, blood volume and oxygen utilization. Normal values and effect of age. *Brain.* 1990;113:27-47.
145. Clayden JD, Dayan M, Clark CA. Principal networks. *PLoS One.* 2013;8(4):e60997.

146. Wilson M, Morgan PS, Blumhardt LD. Quantitative diffusion characteristics of the human brain depend on MRI sequence parameters. *Neuroradiology*. 2002;44(7):586-591.
147. Chawla A, Emmanuel J V, Seow WT, Lou J, Teo HE, Lim CCT. Paediatric PNET: pre-surgical MRI features. *Clin Radiol*. 2007;62(1):43-52.
148. Klisch J, Husstedt H, Hennings S, von Velthoven V, Pagenstecher A, Schumacher M. Supratentorial primitive neuroectodermal tumours: diffusion-weighted MRI. *Neuroradiology*. 2000;42(6):393-398.
149. Louis D, Ohgaki H, Wiestler O, et al. The 2007 WHO classification of tumours of the central nervous system. *Acta Neuropathol*. 2007;114(2):97-109.
150. Newton HB, Jolesz FA. *Handbook of neuro-oncology neuroimaging*. Amsterdam: Academic Pr; 2008.
151. Chenevert TL, Stegman LD, Taylor JM, et al. Diffusion magnetic resonance imaging: an early surrogate marker of therapeutic efficacy in brain tumors. *J Natl Cancer Inst*. 2000;92(24):2029-2036.
152. Kotsenas AL, Roth TC, Manness WK, Faerber EN. Abnormal diffusion-weighted MRI in medulloblastoma: does it reflect small cell histology? *Pediatr Radiol*. 1999;29(7):524-526.
153. Razek AAKA, Megahed a S, Denewer A, Motamed A, Tawfik a, Nada N. Role of diffusion-weighted magnetic resonance imaging in differentiation between the viable and necrotic parts of head and neck tumors. *Acta Radiol (Stockholm, Sweden 1987)*. 2008;49(3):364-370.
154. Vossen JA, Buijs M, Geschwind JFH, et al. Diffusion-Weighted and Gd-EOB-DTPA-Contrast-Enhanced Magnetic Resonance Imaging for Characterization of Tumor Necrosis in an Animal Model. *J Comput Assist Tomogr*. 2009;33(4):626.

155. Kaplan E, Meier P. Nonparametric estimation from incomplete observations. *J Am Stat Assoc.* 1958;53(282):457-481.
156. Altman DG. *Practical Statistics for Medical Research*. Chapman and Hall; 1990.
157. Clark TG, Bradburn MJ, Love SB, Altman DG. Survival Analysis Part I: Basic concepts and first analyses. *Br J Cancer*. 2003;89(2):232-238.
158. Peto R, Pike M, Armitage P, et al. Design and analysis of randomized clinical trials requiring prolonged observation of each patient. II. analysis and examples. *Br J Cancer*. 1977;35(1):1-39.
159. Cox D. Regression models and life-tables. *J R Stat Soc.* 1972;34(2):187-220.
160. Bradburn MJ, Clark TG, Love SB, Altman DG. Survival Analysis Part II: Multivariate data analysis - an introduction to concepts and methods. *Br J Cancer*. 2003;89(3):431-436.
161. Bradburn MJ, Clark TG, Love SB, Altman DG. Survival Analysis Part III: Multivariate data analysis - choosing a model and assessing its adequacy and fit. *Br J Cancer*. 2003;89(4):605-611.
162. Clark TG, Bradburn MJ, Love SB, Altman DG. Survival Analysis Part IV: Further concepts and methods in survival analysis. *Br J Cancer*. 2003;89(5):781-786.
163. Therneau TM, Lumley T. *survival: Survival analysis [computer program]*. 2010. Available at: <http://cran.r-project.org/web/packages/survival/index.html>
164. Bland JM, Altman DG. Statistical methods for assessing agreement between two methods of clinical measurement. *Lancet*. 1986;1(8476):307-310.
165. Bland JM, Altman DG. Measuring agreement in method comparison studies. *Stat Methods Med Res.* 1999;8(2):135-160.

166. Jenkinson MD, du Plessis DG, Smith TS, Joyce KA, Warnke PC, Walker C. Histological growth patterns and genotype in oligodendroglial tumours: correlation with MRI features. *Brain*. 2006;129(7):1884-1891.
167. Megyesi JF, Kachur E, Lee DH, et al. Imaging correlates of molecular signatures in oligodendrogliomas. *Clin Cancer Res*. 2004;10(13):4303-4306.
168. Packer RJ, Macdonald T, Vezina G, Keating R, Santi M. Medulloblastoma and primitive neuroectodermal tumors. *Handb Clin Neurol*. 2012;105:529-548.
169. Ho DM, Hsu CY, Wong TT, Ting LT, Chiang H. Atypical teratoid/rhabdoid tumor of the central nervous system: a comparative study with primitive neuroectodermal tumor/medulloblastoma. *Acta Neuropathol*. 2000;99(5):482-488.
170. Ray A, Ho M, Ma J, et al. A clinicobiological model predicting survival in medulloblastoma. *Clin cancer Res*. 2004;10(22):7613-7620.
171. Dufour C, Beaugrand A, Le Deley MC, et al. Clinicopathologic prognostic factors in childhood atypical teratoid and rhabdoid tumor of the central nervous system: A multicenter study. *Cancer*. 2012;118(15):3812-3821.
172. Northcott PA, Korshunov A, Witt H, et al. Medulloblastoma comprises four distinct molecular variants. *J Clin Oncol*. 2011;29(11):1408-1414.
173. Grech-Sollars M, Saunders DE, Phipps KP, Clayden JD, Clark CA. Response to "Reply to 'Survival analysis for apparent diffusion coefficient measures in children with embryonal brain tumors,' by Grech-Sollars et al." *Neuro Oncol*. 2013;15(3):268.
174. Fleming AJ, Chi SN. Brain tumors in children. *Curr Probl Pediatr Adolesc Health Care*. 2012;42(4):80-103.

175. Jones C, Perryman L, Hargrave D. Paediatric and adult malignant glioma: close relatives or distant cousins? *Nat Rev Clin Oncol.* 2012;9(7):400-413.
176. Li X, Ashana AO, Moretti VM, Lackman RD. The relation of tumour necrosis and survival in patients with osteosarcoma. *Int Orthop.* 2011;35(12):1847-1853.
177. Packer RJ, Boyett JM, Zimmerman RA, et al. Outcome of children with brain stem gliomas after treatment with 7800 cGy of hyperfractionated radiotherapy. A Childrens Cancer Group Phase I/II Trial. *Cancer.* 1994;74(6):1827-1834.
178. Amaravadi RK, Thompson CB. The roles of therapy-induced autophagy and necrosis in cancer treatment. *Clin Cancer Res.* 2007;13(24):7271-7279.
179. Sharma U, Sah RG, Parshad R, Sharma R, Seenu V, Jagannathan NR. Role of apparent diffusion coefficient values for the differentiation of viable and necrotic areas of breast cancer and its potential utility to guide voxel positioning for MRS in the absence of dynamic contrast-enhanced MRI data. *Magn Reson Imaging.* 2012;30(5):649-55.
180. Galbán CJ, Chenevert TL, Meyer CR, et al. Prospective analysis of parametric response map-derived MRI biomarkers: identification of early and distinct glioma response patterns not predicted by standard radiographic assessment. *Clin cancer Res.* 2011;17(14):4751-4760.
181. Ellingson BM, Cloughesy TF, Zaw T, et al. Functional diffusion maps (fDMs) evaluated before and after radiochemotherapy predict progression-free and overall survival in newly diagnosed glioblastoma. *Neuro Oncol.* 2012;14(3):333-343.
182. Yasin S, Harkness W, Cross J, Cohen N, Jacques T. Subependymal Giant Cell Astrocytoma (SEGA) cells respond to rapamycin in vitro. In: *Neuropathology and Applied Neurobiology*; 2010:41-42.

183. Ghent AW. A Method for Exact Testing of 2X2 , 2X3 , 3X3 , and Other Contingency Tables , Employing Binomial Coefficients. *Am Midl Nat.* 1972;88(1):15-27.
184. Cardillo G. *MyFisher33: a very compact routine for Fisher's exact test on 3x3 matrix* [computer program]. 2007. Available at: <http://www.mathworks.co.uk/matlabcentral/fileexchange/15482-myfisher33>
185. Ellingson BM, Cloughesy TF, Lai A, Nghiemphu PL, Pope WB. Nonlinear registration of diffusion-weighted images improves clinical sensitivity of functional diffusion maps in recurrent glioblastoma treated with bevacizumab. *Magn Reson Med.* 2012;67(1):237-245.